

University of Southampton Research Repository ePrints Soton

Copyright © and Moral Rights for this thesis are retained by the author and/or other copyright owners. A copy can be downloaded for personal non-commercial research or study, without prior permission or charge. This thesis cannot be reproduced or quoted extensively from without first obtaining permission in writing from the copyright holder/s. The content must not be changed in any way or sold commercially in any format or medium without the formal permission of the copyright holders.

When referring to this work, full bibliographic details including the author, title, awarding institution and date of the thesis must be given e.g.

AUTHOR (year of submission) "Full thesis title", University of Southampton, name of the University School or Department, PhD Thesis, pagination



Faculty of Physical Science and Engineering

MODELLING AND DESIGN OPTIMISATION OF A HOLLOW CATHODE THRUSTER

Daniele Frollani

Thesis submitted for Doctor of Philosophy

Faculty of Physical Sciences and Engineering
December 2014

UNIVERSITY OF SOUTHAMPTON ABSTRACT

Faculty of Physical Sciences and Engineering

Doctor of Philosophy

MODELLING AND DESIGN OPTIMISATION OF A HOLLOW CATHODE THRUSTER

by Daniele Frollani

The present trend in spacecraft is to have two separate thrusters systems performing different tasks, a main electric propulsion system operating on xenon and a chemical system, usually bipropellants or cold gas. The development of a low power electric propulsion system operating on xenon to replace the chemical thrusters on board spacecrafts would be beneficial. It would be bring significant advantages in terms of mass saving from the sharing of the tanks, pipes and flow control unit, also with improvements in the specific impulse.

In recent years experiments have demonstrated the possibility of using hollow cathodes as standalone thrusters, with indirect thrust measurement performed at the University of Southampton. Nevertheless indirect thrust measurements bring large uncertainties on the real value of the thrust. For the first time, direct thrust measurements were carried out with two different thrust balances on two different hollow cathode thrusters, derived from the T5 and T6 hollow cathodes, with unique design modification in the orifice and anode geometry. These measurements provide a unique insight into the real performance range of hollow cathode thrusters. Significant improvements in thrust, specific impulse and thrust efficiency have been achieved thanks to the optimized design of the T6 hollow cathode.

The design of the thruster was modified using a one dimensional theoretical model developed within this research. With the help of the theoretical model the optimisation of the hollow cathode thruster design was carried out and a better understanding of the physical mechanisms which contribute to the generation of the thrust could be achieved, with the conclusion of electrothermal and electromagnetic phenomena being the main contributors. The main conclusions of the research and recommendations for related future works are also presented.

Living is easy with eyes closed misunderstanding all you see...

(Strawberry Field Forever)

ACKNOWLEDGEMENTS

First and foremost I offer my sincerest gratitude to my supervisors, Prof Stephen Gabriel and Dr Michele Coletti, for the opportunity given and for their continuous guidance.

Thanks are due to Mike and lots of other people at QinetiQ for securing the use of the T5 and T6 hollow cathodes and for sharing their technical support and know-how.

Thanks to the office gang, Simone and Michele, and Ismat and Francesco sometimes, for the great working environment and for making this research enjoyable.

Thanks to all my friends here in Southampton, in particular Rossella and all my housemates. Thanks to you all I felt like at home.

Many thanks to the university gang in Rome. Time passes by and everyone is in a different country, but somehow we have always found a way to meet.

Johns (Giovanni), I can always count on you. Thanks.

Carla, you have been my friend for 'almost 14 years since 2001'. Thanks for your continuous support, even when things seemed to go terribly wrong.

Finally, to my family; Valeria, Simone, zia e zio, nonna, nonno (from above), zia Loredana, thanks for your support. Mom, dad, this is dedicated to you.

Contents

Ch	apter	r I	16		
I.1.	Res	search Motivation	16		
I.2.	Obj	jectives and Novelty of the Research	16		
I.3.	Pro	pulsion in Space	17		
I.3	.1.	Basic Equations	17		
I.3	.2.	Classification of Space Propulsion System	19		
I.4.	App	plications: All-Electric Spacecraft	22		
I.4	.1.	Competing EP Technologies	22		
I.4	.2.	HCT Requirements for an All-Electric Spacecraft	28		
I.5.	Stru	ucture of the Thesis	29		
Ch	apter	r II	31		
II.1.	The	e Hollow Cathode Thruster	31		
II.	1.1.	The HCT Regions	33		
II.2.	Exp	perimental Investigations on HCs Operational Modes	35		
II.3.	Mo	delling of HCs/HCTs	37		
II.3	3.1.	Modelling of HCTs with External Applied Magnetic Field	39		
II.3	3.2.	Modelling of Arcjet Constrictors	39		
II.4.	Pre	vious Work on HCs/HCTs Thrust Measurements	40		
II.5.	The	eoretical Thrust Mechanisms	47		
II.	5.1.	Heavy Particles Gasdynamic Contribution	47		
II.	5.2.	Electrons Gasdynamic contribution	47		
II.	5.3.	Electromagnetic Thrust	49		
II.	5.4.	High Energy Ions Production	50		
	Chapter III				
(Chapt	ter III	52		
III.1.	•	nputs and Outputs			

III.3.	The	oretical Model for the Orifice Region	57
III.3.1	1.	Assumptions	57
III.3.2	2.	Source Terms	60
III.3.3	3.	Equations	64
III.3.4	4.	Boundary Conditions	67
III.3.5	5.	Mesh and Solution	68
III.4.	Mo	del for the Anode/Nozzle Region	68
III.5.	Wh	ere the Thrust is Calculated	69
III.6.	Tre	nds of the Plasma Parameters	70
III.7.	Mo	del Sensitivity	74
III.8.	App	olication of an External Magnetic Field in the Model	79
III.8.1	1.	Effect on the Electromagnetic Thrust	79
III.8.2	2.	Effect on the HCT Behaviour	80
III.8.3	3.	Analytical Treatment	81
III.8.4	4.	Ideal Magnetic Field Shape	88
Cha	pter	IV	90
IV.1.	The	T5 HCTs	90
IV.2.	The	optimization of the HCT	92
IV.2.	1.	Flowchart and Boundaries	93
IV.2.2	2.	The Optimised T6 HCT	95
IV.2.	3.	Magnetic Field Calibration	97
IV.3.	Tes	t Equipment and Set-Up at AER	98
IV.3.	1.	Vacuum Rig and diagnostic	98
IV.3.2	2.	Fluidic Line	98
IV.3.	3.	Test equipment	99
IV.3.4	4.	Electric Interfaces	101
IV.3.:	5.	Mechanical Interfaces	102

IV.3.6.	The Thrust Balance at Aerospazio	102
IV.4. Tes	t Equipment and Set-Up at UoS	108
IV.4.1.	Vacuum Rig and diagnostic	108
IV.4.2.	Fluidic Line	109
IV.4.3.	Test equipment	110
IV.5. The	e thrust balance at the UoS	112
IV.5.1.	Thrust Balance Characterization	114
IV.5.2.	Evaluation of thermal effects on the measurements	123
IV.5.3.	The error budget	124
IV.5.4.	Thrust Balance Assessment	125
Chapter V	7	127
V.1. Direct	t Measurements on the HCTs	127
V.2. Cold	gas and Resistojet Thrust Measurements	128
V.3. Disch	arge Characteristics	132
V.3.1. T	The T5 HCT	132
V.3.2. T	The T6 HCT	133
V.4. Disch	arge Thrust Measurements	139
V.4.1. T	75K HCT	139
V.4.2. T	⁷ 6 HCT	141
V.5. Comp	parison with the requirements	150
V.6. Erosio	on	151
Chapter	VI	157
VI.1. The	eoretical Model and Mechanisms of Thrust Production	157
VI.2. The	e Design Optimisation of the T6 HCT and the Direct T	hrust
Measuremen	nts	159
VI.3. Nov	velty and Applicability of the Work	161
VI.4. Rec	commendations for Future Work	163

TABLE OF FIGURES

Figure 1 - Optimization of the specific impulse for an electric thruster	21
Figure 2 - Schematic of a resistojet	23
Figure 3 – Thrust vs Isp for the T50 [29]	24
Figure 4 – Thrust vs Efficiency for the T50 [29]	24
Figure 5 – Calculated (eq (1.9)) to claimed efficiency ratio for a) T50 and b) T15	25
Figure 6 – Calculated (eq (1.12)) to claimed efficiency ratio for T50	25
Figure 7 - Schematic of an arcjet	26
Figure 8 - General HCT configuration	28
Figure 9 - General HCT configuration	32
Figure 10 – Different orifice to cathode diameter ratio HCT configurations [35]	33
Figure 11 – Active region in the cathode	34
Figure 12 - Visual appearance of the HC discharge from a) plume to e) spot m	node
[47]	36
Figure 13 – Schematic of ion production region [37]	37
Figure 14 – Plasma density for two different HC geometries [65]	39
Figure 15 – The constrictor region in an Arcjet [70]	40
Figure 16 – a) Inelastic and b) elastic collisions of particles against the target	41
Figure 17 – The pendulum used in [78]	42
Figure 18 – Measured cathode thrust as a function of target angle [78]	43
Figure 19 - Isp measured on a T6 HCT varying the orifice diameter with xeno	n at
25 A [6]	43
Figure 20 – Plume-to-spot mode transition with argon at 12 A on a T6 HCT [6]	44
Figure 21 - Thrust obtained in operation of the T5 and T6 cathodes in hot and	cold
gas mode [12]	45
Figure 22 - Thrust for the T5FO cathode with argon [12]	45
Figure 23 - Thrust for the T6 HCT with argon and xenon [12]	46
Figure 24 – Comparison between theoretical and measured thrust [12]	46
Figure 25 - Equivalent amps in a HCT	48
Figure 26 - Sketch for the determination of the electromagnetic thrust contribution	n49
Figure 27 – HCT geometry and domain region	53
Figure 28 – Inputs and outputs in the model	54

Figure 29 – Currents in a HCT	56
Figure 30 - Charge exchange mean free path in the orifice	58
Figure 31 - Mach number in the orifice of a a) T5 at 3.2 A with Argon	and b)
NSTAR at 8.1 A with Xenon	60
Figure 32 – Source and sink terms for the mass	61
Figure 33 - Computational region division in the orifice and main collision pro	ocesses
	65
Figure 34 – Geometry of the T5 and NSTAR cathodes	71
Figure $35 - a$) Plasma and b) neutral density profiles in the orifice of the N	ISTAR
cathode at TH8 and TH15 computed with the model	72
Figure $36 - a$) Electron temperature and b) plasma potential profile in the ori	ifice of
the NSTAR cathode at TH8 and TH15 computed with the model	72
Figure $37 - a$) Plasma and b) neutral density profile in the orifice of the T5	HC at
3.2 A and 2.7 sccm	73
Figure 38 - Plasma potential profile in the orifice of the T5 HC at 3.2 A a	ınd 2.7
sccm	73
Figure 39 – Trends of a) Thrust and b) Specific impulse varying D_{st}	74
Figure 40 – Trends of a) Discharge Voltage and b) Discharge Power varying I	$O_{st}75$
Figure 41 – Trends of a) Thrust and b) Specific impulse varying L_{st}	75
Figure 42 – Trends of a) Discharge Voltage and b) Discharge Power varying I	L _{st} 76
Figure 43 – Trends of a) Thrust and b) Specific impulse varying L_{div}	76
Figure 44 – Trends of a) Discharge Voltage and b) Discharge Power varying I	L _{div} 77
Figure 45 – Trends of a) Thrust and b) Specific impulse varying \mathcal{V}_{div}	77
Figure 46 – Trends of a) Discharge Voltage and b) Discharge Power varying a	\mathcal{Y}_{div} .78
Figure 47 – Trends of a) Thrust and b) Specific impulse varying the mass flo	ow rate
Figure 48 – Trends of a) Discharge Voltage and b) Discharge Power varying	
mass flow rate	
Figure 49 – Radial and axial direction in the cathode	
Figure 50 – Magnetic field configuration	
Figure $51 - t_S/R_L$ vs axially magnetic field applied in the insert region	84
Figure 52 - $1/(1+\Omega^2)$ vs axially magnetic field applied in the insert region	85
Figure 53 – Variables vs axially magnetic field applied in the orifice region	87

Figure 54 – Magnetic field configuration	88
Figure 55 – Suggested shape for the magnetic field	89
Figure 56 – The T5K HCT	91
Figure 57 – The T5A HCT	91
Figure 58 – Dimension to be optimised (insulating spacer not shown)	93
Figure 59 – Flowchart	94
Figure 60 – T6 HCT Cutaway	96
Figure 61 – Pieces manufactured for the T6 HCT.	96
Figure 62 – The T6 HCT	97
Figure 63 – Test set-up of the calibration test of the magnetic field	97
Figure 64 – Results of the calibration of the magnetic field	98
Figure 65 – Fluidic lines at AER	99
Figure 66 – The TPS	99
Figure 67 – Electrical test set-up at AER for a) the T5K and b) the T6 HCT	101
Figure 68 – Electrical connections at AER	101
Figure 69 – a) T5K and b) T6 HCTs on the thrust balance at AER	102
Figure 70 – Calibration graphs for cold gas thrust measurements on the T6 H6	CT.105
Figure 71 – Calibration graphs for discharge with magnetic field on the T6	HCT a)
10A 4 sccm and b) 15A 8 sccm	105
Figure 72 – Oscillations in the raw thrust	107
Figure 73 – Sensor trace at AER on the T6 for 8sccm and a) 10A, B=0 and b	
Figure 74 - The vacuum chamber at UoS	
Figure 75 – Fluidic lines at UoS	110
Figure 76 – Electric set-up at UoS for the T6 HCT	111
Figure 77 – Electric set-up at UoS for the T5 HCT	111
Figure 78 - Complete thrust balance assembly schematic	112
Figure 79 - Swinging arm of the thrust balance a) CAD model b) manufacture	ed113
Figure 80 - Electrical connections constrained to the thrust balance	113
Figure 81 - Working distance and sweet-spot of EUCLID	114
Figure 82 - Thrust balance, schematics (not in scale)	115
Figure 83 - Displacement sensor trace for a T6 in discharge mode at 10 A	and 10
sccm	117

Figure 84 - Example of Fourier Transform to evaluate the natural frequency	119
Figure 85 - Thrust balance a) without and b) with weights	121
Figure 86 - Geometrical parameters of the weights	121
Figure 87 - Dynamic Calibration for the calculation of the moment of inertia	for the
T6 and T5A balance assembly	122
Figure 88 - T6 HCT in cold gas mode at UoS and AER	125
Figure 89 - Thrust at AER and UoS at 10A and 15 A a) without B and b) with	ith the
applied B	126
Figure 90 – Arc attachment section on the T6 HCT	128
Figure 91 – Thrust in cold gas and resistojet mode for the T5A	129
Figure 92 – Thrust in cold gas and resistojet mode for the T6	130
Figure 93 –Thrust vs applied power	130
Figure 94 –Isp in cold gas and resistojet mode for the T5A and T6 HCTs	131
Figure 95 – Thrust efficiency in resistojet mode	132
Figure 96 – Discharge characteristics on the T5K and T5 HCT	133
Figure 97 – Discharge characteristics on the T6 HCT	133
Figure 98 – Discharge characteristics on the T6 HCT – 5, 15 and 24 A only	134
Figure 99 – Discharge characteristics vs mdot on the T6 HCT	134
Figure 100 – Discharge characteristics at 15A and 24A on the T6 HCT at UoS	135
Figure 101 – Discharge characteristics vs E on the T6 HCT	135
Figure 102 – Discharge characteristics vs E on the T6 HCT	136
Figure 103 - Effect of the application and removal of the magnetic field of	on the
discharge voltage at 15 A and 4 sccm on the T6	136
Figure 104 – Pictures of T6 HCT in discharge mode	138
Figure 105 – Thrust vs mass flow rate on the T5K HCT	140
Figure $106 - a$) Isp vs. mass flow rate and b) contribution to the thrust on the	e T5K
	140
Figure 107 –Thrust efficiency of the T5 HCT	141
Figure 108 – Overall view of the thrust obtained with no applied magnetic field	1142
Figure 109 – Overall view of the thrust obtained with applied magnetic field	143
Figure 110 –Contribution to the thrust for the T6 HCT with no applied B	144
Figure 111 – Overall view of the Isp obtained	145
Figure 112 – Thrust plotted against the discharge current	146

Figure 113 – Isp plotted against the discharge current	146
Figure 114 – Overall view of the thrust vs. specific energy obtained	147
Figure 115 – Overall view of the Isp vs. specific energy obtained	147
Figure 116 – Example of thrust and specific impulse vs. E for a fixed mass	flow rate
	147
Figure 117 – Increase in thrust and Isp with the applied magnetic field	148
Figure 118 – Thrust efficiency vs mass flow rate on the T6 HCT	149
Figure 119 – Thrust efficiency vs discharge current on the T6 HCT	149
Figure 120 - Thrust efficiency vs specific energy on the T6 HCT at UoS	150
Figure 121 - Orifice new shape measured with the microscope	152
Figure 122 - Orifice visual inspection	152
Figure 123 - The orifice a) as given by QQ and b) after the test at Aerospazio	o153
Figure 124 – New orifice geometry	153
Figure 125 – The orifice tip	154
Figure 126 – T6 HCT orifice visual inspection with the microscope	154
Figure 127 – The anode/nozzle	155
Figure 128 – The spacer	156
Figure 129 – T5 with a different nozzle spacer	164
Figure 130 – a) Visual inspection of the spacer b) Heater voltage during the	cathode
warm up	165

TABLE OF TABLES

Table 1- Velocity increments needed for different missions [23]	18
Table 2- Xenon resistojet	23
Table 3- Xenon Arcjets	27
Table 4- Requirement for the electric propulsion system [32, 33]	29
Table 5 – Geometry variables which can be defined in the model	55
Table 6 – NSTAR geometry and throttle level [35, 97]	71
Table 7 – Baseline dimensions of the HCT to show the trends	74
Table 8 - Variables in the insert region with and without correction	86
Table 9 - Variables in the orifice region with and without correction	87
Table 10 – Range of parameters for the T5 and T6	93
Table 11 – Best performance predicted by the model	95
Table 12 – Optimized T6 HCT geometry	95
Table 13 - Test equipment with the T5K HCT at AER	100
Table 14 - Test equipment with the T6 HCT at AER	100
Table 15- Cable used	102
Table 16 - Sample weight used for calibration	104
Table 17 – Calibration gain for the T5K HCT tests at AER	105
Table 18 – Calibration gain for the T6 HCT tests at AER	106
Table 19 – Calibration gain for the T5K HCT tests at AER	108
Table 20 - Geometrical values of the weights	121
Table 21 - Configuration of weights used	122
Table 22 – Moment of inertia and uncertainty	123
Table 23 - Error budget for the T6 HCT in discharge mode	124
Table 24 - Error budget for the T5A HCT in discharge mode	125
Table 25 - Thrust measurements set-points	128
Table 26 - Thrust measurements set-points for the T5K	139
Table 27 - Thrust measurements set-points for the T6 HCT	141
Table 28. Comparison of experimental data with requirements	151

NOMENCLATURE

В	Magnetic field or Bessel function	V	Voltage
CG	Calibration gain	W	Source term for the mass equation
CP	Chemical propulsion	X	Source term for the momentum equation
cp	Specific heat capacity at constant pressure	Y	Source term for the energy equation
D	Diameter or diffusion coefficient	β	Heavy particles to wall
E	Electric field or specific energy	γ	temperature ratio Heat capacity ratio
EP	Electric propulsion	$\varepsilon 0$	Vacuum permittivity
EWSK	East west station keeping	η	Efficiency
f	Frequency	λ	Free path length
$\stackrel{J}{F}$	Thrust	μ	Mobility
FEEP	Field emission electric propulsion	v	Collision frequency
g0	Standard gravity	ρ	Density
GIE	Gridded ion engine	σ	Cross section
h	Enthalpy	φ	Potential
H	Heat loss	ω	Angular velocity
НС	Hollow cathode	g	Angle
HCT	Hollow cathode thruster	Ω	Hall parameter
HEI	High energy ion	Subsci	-
HET	Hall effect thruster	a	Anode
I	Current	act	Active
Isp	Specific impulse	ax	Axial
$J^{'}$	Current density or moment of inertia	bal	Balance
k	Boltzmann constant or torsional spring rate	c	Cathode
Kn	Knudsen number	ce	Charge exchange
L	Length	D	Discharge
LEO	Low earth orbit	div	Divergent
m	Mass	e	Electrons
M	Atomic mass or mach number	eff	Effective
mdot	Mass flow rate	em	Electromagnetic
MPD	Magneto plasma dynamic	eq	Equivalent
n	Particle density	ew	Electrons to the wall
NSSK	North south station keeping	ex	Exit
p	Pressure	ext	External
P	Power	h	Heavy particles
PS	Power supply	HEI	High energy ions
q	Elementary charge	i	Ions or inlet
Q	Thermal energy exchanged per unit time	in	Inlet
R	Radius	ins	Insert

ion Ionization

iw Ions to the wall

or Orifice

ps Power supply

sh Sheathsp Specificst Straight

wf Work function

Chapter I

Introduction

I.1. Research Motivation

Hollow Cathodes (HCs) play a key role in the field of electric propulsion, being used as sources of electrons for the discharge chamber and plume neutralisation in Gridded Ion engines (GIEs) and Hall Effect thrusters and as plasma contactors on board the International Space Station. The possibility of using HCs as standalone thrusters (hollow cathode thrusters, HCTs) has been extensively investigated at the University of Southampton for the last decade [1-15]. The main purpose of the research presented within this thesis is to expand the known performance of hollow cathode thrusters in terms of achievable thrust, specific impulse and power consumption. This has been done by developing a theoretical model capable of predicting the performance of HCTs with reasonable accuracy, and then using this model to design an optimized configuration of a T6 HCT which has been tested using two different direct thrust balances, of which one designed, commissioned and manufactured specifically for this research project. A T5 HCT was also tested with a direct thrust balance. The T5 and T6 HCTs tested within this research come from the HC technology developed for the UK-10, UK-25, T5 and T6 GIEs and Bepi Colombo [16-22].

I.2. Objectives and Novelty of the Research

If HCTs are to be used in practical applications onboard satellites, they will have to show performance at least comparable with other contending technologies such as cold gas, resistojets, arcjets and chemical propulsion systems too. In this context the development of a mathematical tool capable of self-consistently predicting the performance of HCTs by only giving as inputs the operational parameters (mass flow rate and discharge current) and the complete geometry becomes very important

in order to understand how HCTs can be improved. In order to reach this goal a number of steps were taken:

- 1. The physical mechanisms governing the production of the thrust in a HCT were studied and identified.
- 2. A theoretical model was developed to predict the performance of HCTs. This is the first theoretical model developed with the aim of predicting the performance of HCTs in terms of thrust, *Isp* and needed power.
- 3. An optimized variant of the T6 HCT was designed using the mathematical tool developed. The T6 HCT was also equipped with a coil able to generate a magnetic field in the orifice region to experimentally understand if it could bring advantages in terms of performance. This was also the first time that the design of a HCT was carried out with a mathematical tool for the optimization of its performance.
- 4. A direct thrust balance and supporting architecture was designed and developed, allowing for the first direct thrust measurements of HCTs in literature. Some of the thrust measurements were also replicated at Aerospazio Tecnologie, with the direct thrust balance developed there, for additional reliability.

I.3. **Propulsion in Space**

I.3.1. **Basic Equations**

In all the space systems, the propulsive force is obtained by accelerating the propellant to high velocities. According to Newton's third law of motion, a rocket experiences a reaction force equal and opposite to the time rate of change of the momentum of the propellant, called thrust (F):

$$F = M \frac{du}{dt} = -\frac{d}{dt} \left(m_p u_{ex} \right) = -\dot{m} u_{ex}$$
 (1.1)

where M and u are respectively the mass and velocity of the rocket, m_p is the mass of the propellant, u_{ex} is its exhaust velocity relative to that of the spacecraft (effective exhaust velocity) and \dot{m} is the time rate of change of the mass of the rocket, referred

to as the mass flow rate. The time rate of change of the mass of the spacecraft is equal to that of the propellant:

$$\frac{dM}{dt} = \frac{dm_p}{dt} = \dot{m} \tag{1.2}$$

By substituting equation (1.2) into equation (1.1) it is possible to obtain:

$$du = -u_{ex} \frac{dM}{M} \tag{1.3}$$

Integrating equation (1.3) over a fire, from the initial velocity of the rocket u_i (when its mass is m_i) to the final velocity u_f (when its mass is m_f), it is possible to obtain:

$$m_p = m_i - m_f = m_i [1 - \exp(-\Delta u/u_{ex})]$$
 (1.4)

where $\Delta u = u_f - u_i$ is the change of velocity of the spacecraft over the manoeuvre. Equation (1.4) shows the importance of the effective exhaust velocity, which has to be as high as possible in order to spend less propellant over a fire hence to use propellant very efficiently, and which has to be at least comparable with the total Δu (if more fires needed) requested by the mission. Typical values of Δu for a wide range of missions are listed in Table 1 [23]:

Table 1- Velocity increments needed for different missions [23]

Manoeuvre	Δu [m/s]
EWSK in geosynchronous	2/year
NSSK in geosynchronous	49/year
Drag compensation in 400-500 km LEO	<100/year
Drag compensation in 500-600 km LEO	<25/year
Attitude control (3-axis)	5/year
Momentum-wheel unloading	5/year
Escape from earth surface (impulsive)	11,200
Earth orbit to Mars orbit and return	14,000
Earth orbit to Jupiter orbit and return	64,000
Earth orbit to Saturn orbit and return	110,000

Equation (1.4) can be written in terms of specific impulse *Isp*, that is a very important parameter for rocket and a measure of its thrust efficiency; it is defined as:

$$Isp = \frac{F}{\dot{m}g_0} \tag{1.5}$$

where g_0 is the acceleration of gravity at sea-level. Rearranging equations (1.1) and (1.5) it is possible to show the relation between the specific impulse and the effective exhaust velocity:

$$Isp = \frac{u_{ex}}{g_0} \tag{1.6}$$

Equation (1.4) can be rearranged into the classical Tsiolkovsky formula [23]:

$$\Delta u = u_{ex} \ln(m_i/m_f) \tag{1.7}$$

By knowing the total change of velocity required by the mission and the specific impulse of the thruster (or the exhaust velocity) it is possible to know the mass of propellant needed (see equations (1.4) or (1.7)).

I.3.2. Classification of Space Propulsion System

Space rockets propulsion can be classified using different schemes: one of these schemes, for example, divides propulsion systems into categories by the propellant composition. The most common scheme used is that of classifying space propulsion systems by the mean in which the propellant is accelerated up to the exhaust velocity, i.e. by the method of supplying energy to the working fluid. Following this scheme, the space propulsion systems can be hence classified as:

- *Chemical*, where chemical combustion is used to supply energy to the propellant;
- *Non-chemical*, where different processes from chemical reactions, such as electric or nuclear power, are used to supply energy to the working fluid;
- Exotic and theoretical system, where new, and sometimes theoretical only, concepts are used.

Among the non-chemical systems, electric propulsion systems use electricity as source of energy. Electric thrusters are usually classified into categories depending on how the fluid is accelerated, and these categories are:

- *Electrostatic*, where a high voltage electrostatic field is used for the acceleration of the ions;
- Electromagnetic, where the interaction of the charged particles with the
 magnetic and electric field within and around the discharge chamber is used
 to accelerate the plasma. The magnetic field can be externally applied or selfproduced;
- *Electrothermal*, where the propellant is heated by means of electric power such as resistances or electric arcs.

Within these three categories, another subdivision is usually made by the techniques for propellant heating or for ion generation. The electrostatic systems include GIEs, HETs, FEEPs (Field Emission Electric Propulsion) and colloid ion. Electromagnetic systems include MPDs (MagnePlasmaDynamic Thrusters), PPTs (Pulsed Plasma Thrusters) and Helicon plasma thrusters. Electrothermal systems differ from those listed under the electromagnetic and electrostatic categories since the acceleration of the working fluid is due to thermodynamic effects primarily and not to the interaction of charged particles with electric and magnetic fields. They include resistojets, arcjets and HCTs.

In the electric propulsion systems the input energy, i.e. the electrical energy supplied by batteries or solar panels, can have ideally no upper limit. But before looking for extremely high *Isp* it is useful to remember that the batteries or solar panels have a mass which has to be considered in the overall design. An important parameter for electric thrusters becomes then the specific power, defined as the power needed per unit of thrust:

$$P_{sp} = P_{in}/F \tag{1.8}$$

where P_{in} is the input power. Typical values for P_{sp} are 10-80 W/mN depending on the efficiency of the energy conversion μ_T , defined as the ratio between the exhaust kinetic energy of the propellant and the input power:

$$\mu_T = \frac{\frac{1}{2} \dot{m} u_{ex}^2}{P_{in}} = \frac{g_0 F I sp}{2 P_{in}}$$
 (1.9)

Assuming that the mass of the power supplies or the solar panels M_{ps} is linear with the power required:

$$M_{ps} = \alpha P_{in} = \frac{\alpha g_0 F Isp}{2 \mu_T}$$
 (1.10)

where α is the specific mass of the power system, it is possible to show that for a simplified mission where F is constant (and μ_T and α are assumed to be constant), there is a value of the specific impulse which minimizes the sum of the mass of the power supplies M_{ps} and of the propellant m_p :

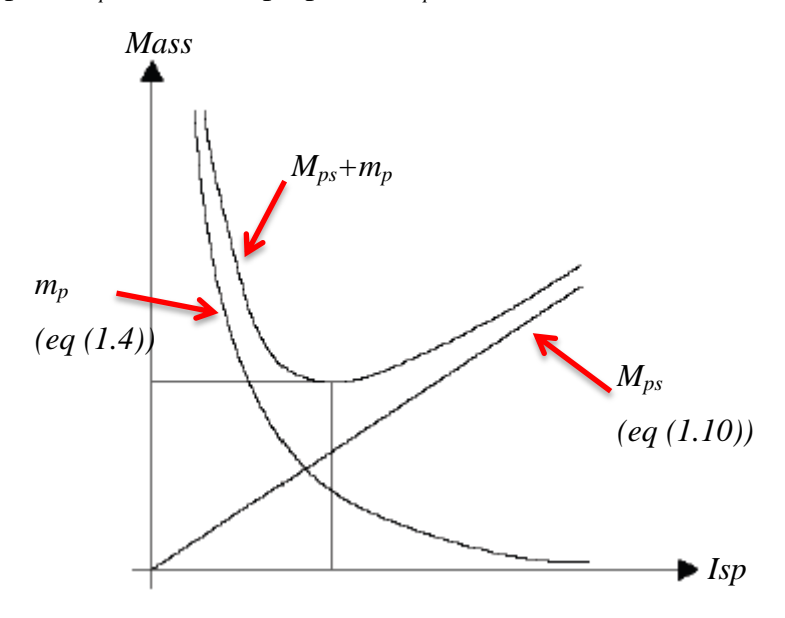


Figure 1 - Optimization of the specific impulse for an electric thruster

The optimized value of the specific impulse is:

$$\overline{Isp} = \frac{1}{g_0} \sqrt{\frac{2\mu_T \Delta t}{\alpha}}$$
 (1.11)

where Δt is the duration of the mission. By increasing or decreasing the optimized value of the specific impulse of the mission, there would be penalties due to an increase in the mass of the power supplies or in the mass of the propellant respectively as shown in Figure 1. From equation (1.11) it is clear that, for a known mission, the development of the electric propulsion needs to be aimed at achieving not only a high thruster efficiency, i.e. the fraction of the input energy converted into kinetic, but also to the development of lighter power supplies. Therefore electric propulsion systems are known to be power-limited [24].

I.4. Applications: All-Electric Spacecraft

At present, the trend in telecommunication satellites is to perform North/South station keeping (NSSK) using electric propulsion (EP). Cold gas systems or chemical propulsion (CP) in general are instead used to perform:

- fast attitude dynamics of a safe mode;
- additional wheel momentum management;
- dedicated East/West station keeping (EWSK) control.

When the CP is integrated in an existing EP system, the additional mass that the former requires in terms of added propellant (which in general will be different from the propellant for the EP), tanks and piping dramatically reduce the benefit of using EP.

Significant advantages would be brought to the mission if the EP system performing NSSK would be integrated with another EP system (in replacement of the CP system) using efficiently the same propellant and performing the listed manoeuvres. In this case there would be improvements in the specific impulse and benefits not only from the use of a single propellant but also a significant mass reduction from the removal of additional tanks and piping.

The ESA European Student Moon Orbiter mission [25] already suggested the possibility of manufacturing an all-electrical spacecraft operating on xenon using the T5 GIE already used on the GOCE (Gravity field and steady-state Ocean Circulation Explorer) mission as main thruster plus 8 HCTs for the attitude and orbit control system (AOCS). The idea was that of minimising the wet mass of the spacecraft by sharing the propellant, the tank, the power processing unit and the flow control unit among the main thruster and the HCTs.

I.4.1. Competing EP Technologies

I.4.1.1. Resistojets

In resistojets the propellant flows through a chamber whose walls are heated resistively, or where there are some elements also heated resistively, before being expanded in the nozzle.

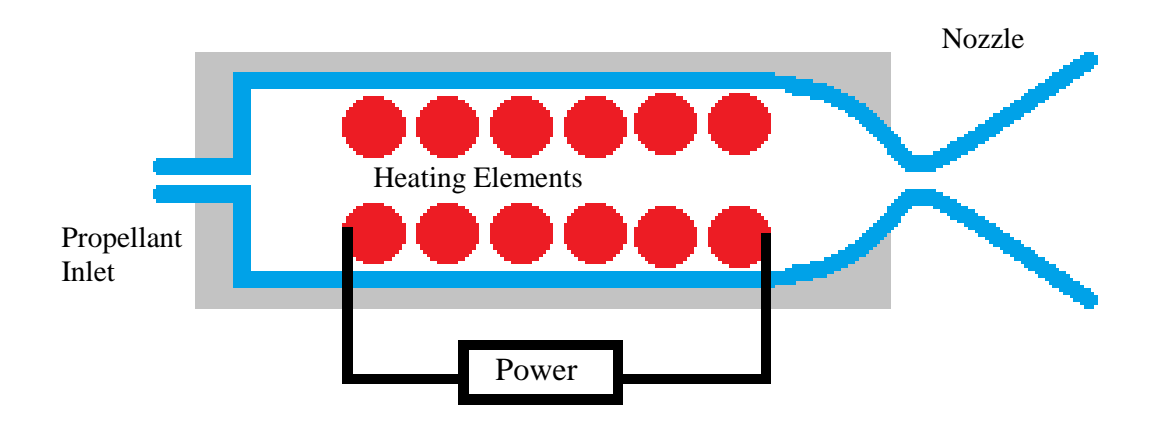


Figure 2 - Schematic of a resistojet

A wide variety of propellants such as ammonia, hydrogen, butane, nitrogen and noble gases have been used in resistojets with power ranging from 10 W to 30 kW [23, 26]. For resistojets operating on xenon, there are examples of performance given in Table 2:

Table 2- Xenon resistojet

Name	Manufacturer	Isp,	Thrust, mN	Power, W	Calculated efficiency with eq.(1.9), %
ALSAT-1					
[27]	Surrey Space Centre	48	220	80	64.7
XR 50 [28]	Alta	55	100	< 50	53.9
XR 100 [28]	Alta	63	125	<80	48.3
XR 150 [28]	Alta	65	100	<95	33.6
T15 [29]	Surrey Space Centre	57	10	30	9.3
T50 [29]	Surrey Space Centre	54	20	65	8.1

In [29] many other thrust measurements are shown in graphs for the T15 and T50 operating on xenon. While in [28] the claimed efficiency is consistent with what calculated with equation (1.9), some of the measurements in [29], reported in Figure 3 and Figure 4, show incongruent data if equation (1.9) is used. For example, as reported in Figure 3, in [29] the T50 reaches about 89 mN at about 36 s with 10W: this would result in a thrust efficiency of about 157%, which is not physical, against the about 73% claimed and shown in Figure 4.

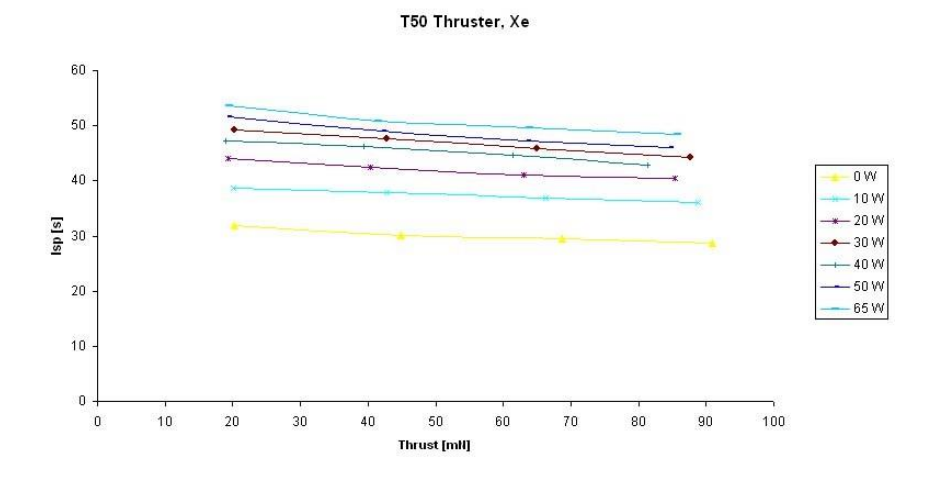


Figure 3 – Thrust vs Isp for the T50 [29]

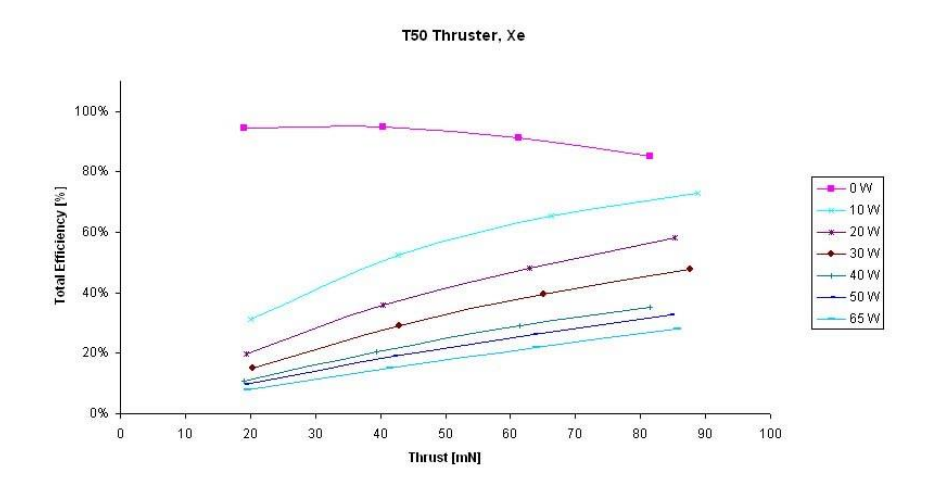


Figure 4 – Thrust vs Efficiency for the T50 [29]

Another example is for the T15, where the efficiency is about 68% at about 73mN and about 37s with a power of 10W: using equation (1.9) the computed efficiency would be about 133%.

The thrust and *Isp* obtained from the graphs in [29] (an error in retrieving the data, estimated in $\pm 5\%$, should be taken into account) have been used to calculate the efficiency with equation (1.9) and compared to what reported in [29]. The ratio of the calculated to the claimed efficiency Ω is shown in Figure 5: it increases with the thrust and decreases with the applied power.

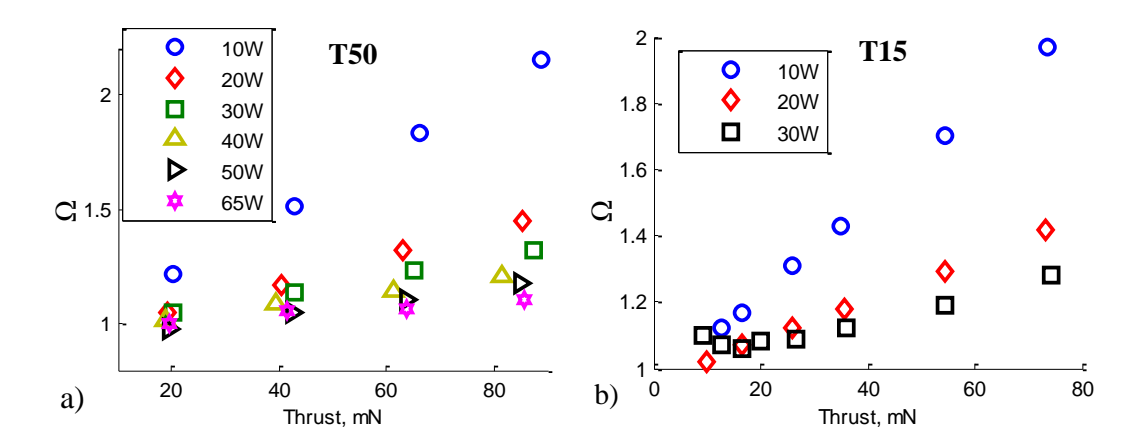


Figure 5 – Calculated (eq (1.9)) to claimed efficiency ratio for a) T50 and b) T15

One explanation could be that for high mass flow rates or low power, the cold-flow power loss [23] should not be neglected, hence the thruster efficiency should be calculated as:

$$\mu_T = \frac{g_0 \left(F \operatorname{Isp} - F^{cg} \operatorname{Isp}^{cg} \right)}{2 P_{in}}$$
 (1.12)

where F^{cg} and Isp^{cg} are the thrust and specific impulse in cold gas mode at the same mass flow rate. As shown in Figure 6, equation (1.12) underestimates the efficiency claimed in [29].

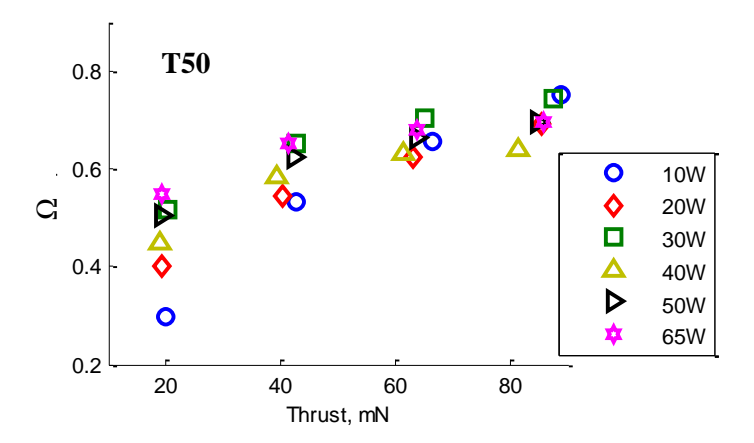


Figure 6 – Calculated (eq (1.12)) to claimed efficiency ratio for T50

In conclusion, reliable data for resistojets operating on xenon are described in [28]: a thrust of the order of 100s mN can be obtained with a specific impulse of the order of 50 s and a thrust efficiency of the order of 60%.

I.4.1.2. Arcjets

In arcjet the propellant is heated when flowing through a high current arc before the expansion in the nozzle. In this type of thruster the propellant gets ionized, but the ionization fraction is small and electromagnetic effects are negligible.

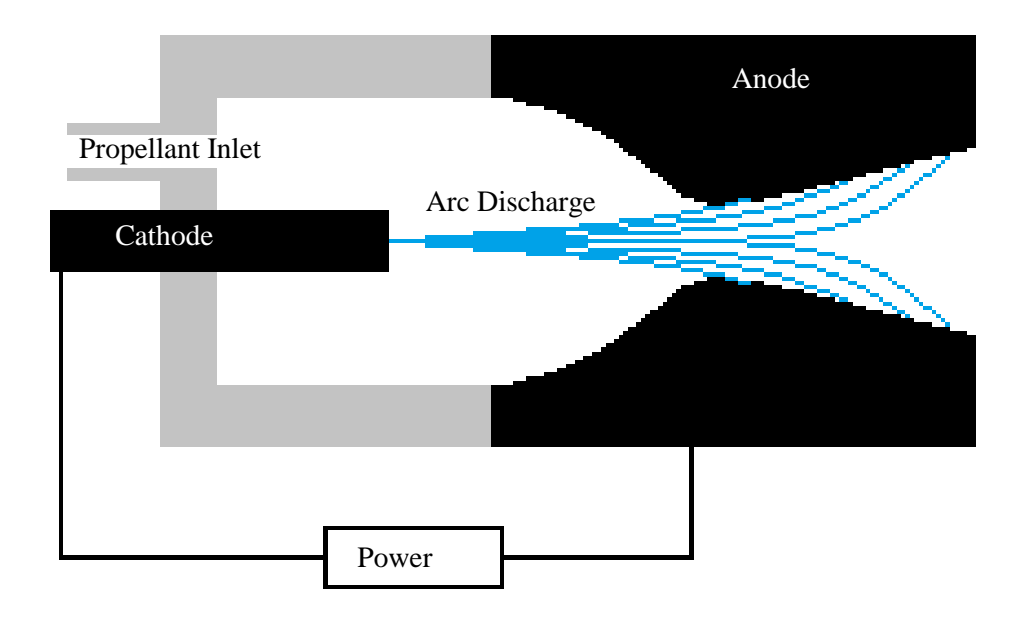


Figure 7 - Schematic of an arcjet

No data about the performance of arcjets operating on xenon have been found in the open literature. On the other hand, arcjets operating on hydrogen, helium, hydrazine and ammonia have been tested with input powers ranging 1-200 kW and *Isp* ranging 500-2100 s [23, 30, 31]. It is possible to calculate the theoretical *Isp* that these tested arcjets would achieve if xenon would be used as propellant. In doing so, the exit temperature T_{ex} of the xenon and the other propellants is assumed to be the same, and no considerations are made regarding the power input that would be needed. The exit velocity of an arcjet can be found by a simple one-dimensional energy balance, as discussed in [23]:

$$u_{ex} = \sqrt{2c_p T_{ex}} \tag{1.13}$$

where c_p is the specific heat at constant pressure. Using equation (1.6) it is possible to find the theoretical values of the *Isp* using xenon propellant, shown in Table 3:

Table 3- Xenon Arcjets

	Power, kW	Propellant	Laboratory	Isp, s	Isp* with Xe, s
-	1	H2	Giannini	1100 [23]	116
	30	H2	Giannini	1010 [23]	106
	30	H2	AVCO	1520 [23]	160
	30	NH3	AVCO	1012 [23]	281
_	200	H2	AVCO	2120 [23]	223

^{*}theoretical

In conclusion, Table 3 shows that expected *Isp* with xenon are typically low because xenon is a heavy gas (atomic mass 131 a.m.u) when compared to H2 (2 a.m.u.), hence its c_p is much larger, being:

$$c_p = \frac{\gamma}{\gamma - 1} \frac{k}{M \cdot m_u} \tag{1.14}$$

where γ is the heat capacity ratio, k is the Boltzmann's constant, M the atomic mass and m_u the atomic mass unit (1.66e-27 kg).

I.4.1.3. Hollow Cathode Thrusters

Hollow cathode thrusters are the main subject of this research hence will be described more in detail in the following chapters. The geometry of a hollow cathode thruster is shown in Figure 8 and it is very similar to that of a hollow cathode, with the only difference that in an HCT all the discharge current is collected at the keeper electrode, usually shaped as a divergent nozzle to enhance the expansion of the hot gas.

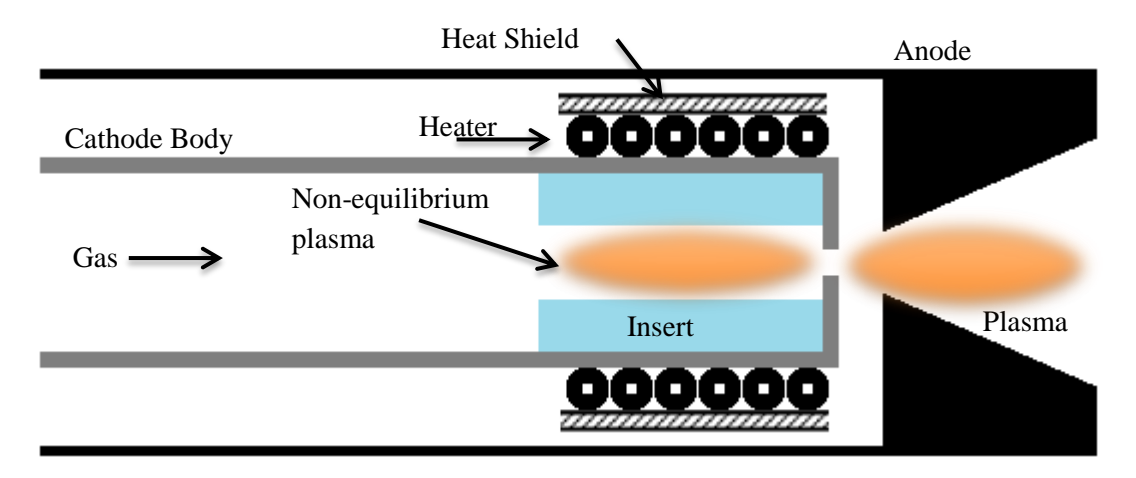


Figure 8 - General HCT configuration

The unique feature that HCTs have is that they can be operated in three different modes:

- as a cold gas thruster, in which the propellant is directly expanded through the orifice in the anode;
- as a resistojet, in which the propellant is heated by the cathode heater and later expanded through the orifice in the anode;
- in the discharge mode, when the arc current is ignited.

I.4.2. HCT Requirements for an All-Electric Spacecraft

A series of guideline requirements to employ HCTs in the AOCS of an all-electrical spacecraft operating on xenon have been derived from [32, 33]. These guideline requirements are for spacecrafts such as SmallGEO, FS1330E and EUROSTAR3000, in which the electric propulsion systems would replace the chemical system of the AOCS to perform mainly detumbling, EWSK manoeuvres and wheel momentum management.

Detumbling is usually performed at the beginning of the satellite life over a short period of time and requires about 50 mN in 130 minutes, which can be relaxed to 25 mN per thruster if for example two devices are operated at the same time. In this case the HCTs may be used in the cold gas mode.

Assuming two devices operating with a moment arm of 1 m, a thrust of 0.5 mN over 18 hours is necessary to efficiently offload a 68 Nms momentum wheel: this is

anyway a worst case scenario since the wheels are rarely in a complete state of saturation.

EWSK for these type of platforms usually requires a Δu of 13.7 mm/s per 24 hour period. Assuming 4 devices operating simultaneously, a thrust of 0.6 mN with an *Isp* of 250s per thruster is required.

A global set of guideline requirements can be obtained from the discussion above in terms of power, mass, thrust and *Isp*, and are shown in Table 4. It is important that the use of EP would provide performance at least comparable with the existing CP system since this would bring at least benefit in the mass reduction of the whole propulsion system.

Table 4- Requirement for the electric propulsion system [32, 33]

Parameter	Requirement	
System mass (12 thrusters)	< 11 kg	
Power per thruster	< 500 W	
Isp	> 250 s	
Thrust	> 0.6 mN	
Isp in cold gas mode	> 30 s	
Thrust in cold gas mode	> 25 mN	

I.5. Structure of the Thesis

Chapter II is the literature review including a comprehensive discussion on the efforts made by many authors to model the plasma inside a HC along with all the thrust measurements on HCTs available in the literature. The theoretical model is presented in chapter III: it is a 1D model for the orifice based on the fluid equations and the first theoretical model with the only aim of predicting the performance of a HCT in terms of thrust and specific impulse. The HCTs tested are described in chapter IV: they are respectively a T5 and T6 based HCT, with the latter designed with the theoretical model developed. In the same chapter the set-up and equipment for the tests carried out at Aerospazio and at the University of Southampton are described, including a full description and characterisation of the direct thrust balance designed and commissioned at the UoS. All the direct thrust measurements on the T5 and T6 HCTs carried out within this research are presented and discussed

in chapter V, together with the comparison with the results from the mathematical tool. Conclusions and recommendations for future work are given in chapter VI.

Chapter II

Background and Review

A review of the background theoretical and experimental investigations carried out on HCs/HCTs is given in this chapter. A discussion on the method used at UoS to obtain thrust measurements on HCTs is also presented.

II.1. The Hollow Cathode Thruster

The geometry of a hollow cathode thruster is very similar to that of a hollow cathode. They both consist of a cathode body, i.e. a hollow cylinder made of a refractory metal, enclosed at the downstream end with a tip with an axial orifice, as shown in Figure 8. The orifice can be straight or partially chamfered. Inside the cathode body, placed against the orifice plate, a dispenser is positioned. In the region of the dispenser, on the cathode body outer surface, a heating element is placed, usually made of a tungsten filament cemented in a ceramic material. An insulating high temperature material, preferably one with a low thermal conductivity, can be placed between the orifice and the anode/nozzle to give continuity to the diverging shape hence optimizing the plume expansion. The anode/nozzle works as a nozzle from the plume expansion point of view and as an electrical terminal, the anode, from the discharge point of view.

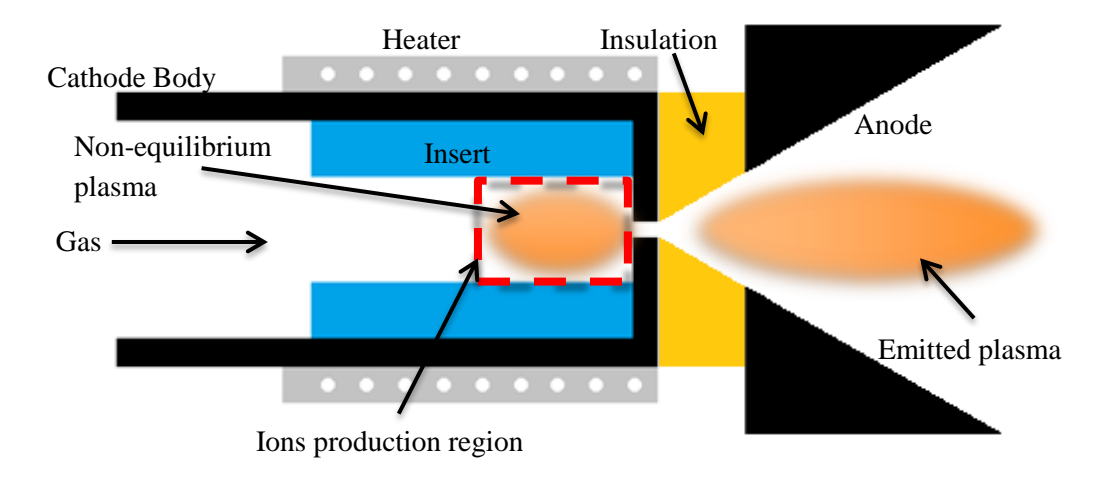


Figure 9 - General HCT configuration

As already discussed, a HCT has unique features since it can be operated in three different modes:

- as a cold gas thruster, in which the propellant is directly expanded through the orifice in the anode;
- as a resistojet, in which the propellant is heated by the cathode heater and later expanded through the orifice in the anode;
- in the discharge mode.

In discharge mode the heater is used to raise the insert to the emissive temperature (>1000 °C). The dispenser of the QinetiQ based HCTs is made of porous tungsten (generally 15%-20% porosity) impregnated with barium oxide (BaO), calcium oxide (CaO) and aluminates (Al₂O₃) in the proportion of 4:1:1. When the insert is heated above 1000 °C, BaO is produced by evaporation and streams into the tungsten matrix producing free barium, which spreads on the emitter surface lowering the emitter work function to 2 – 2.3 eV (2.08 eV at 1450 K [34]) from the 4.5 eV of the bare tungsten. Electron emission then results from the evaporation of active material from the emitting surface on a layer of Ba and oxygen on tungsten [34]. When the gaseous propellant is fed from the upstream, it is partly ionized by the electrons bombardment from the insert helping the initiation of the arc discharge. At this stage a potential gap is applied to ignite the arc discharge, which extends from the anode through the orifice to the emitter. When the discharge is ignited, a plasma is formed in the cathode. A region separating the internal plasma from the emitter surface, called sheath, is also created. This region is usually of the order of some Debye

lengths with a potential drop of 5-15 V hence providing a high electric field at the emitter surface of about 10^6 V/m.

During operation in discharge mode the cathode is in self-heating mode and the heater is then no longer required. In fact the emitter is heated mostly by ions accelerated through the sheath potential or energetic electrons overcoming the sheath potential and reaching the insert, depending on the orifice to cathode diameter ratio [35].

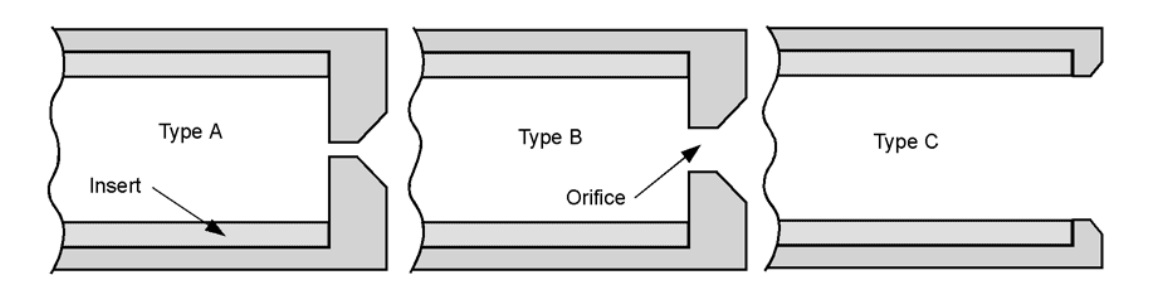


Figure 10 – Different orifice to cathode diameter ratio HCT configurations [35]

The size of the insert and orifice depends on many aspects. In particular, the size of the insert is determined by the total discharge current: a rule of thumb is that for higher discharge current, larger diameters of the insert are required since the current density emitted from its surface is limited. The orifice to cathode diameter ratio also affects the performance. For a fixed insert diameter, by reducing that of the orifice the plasma becomes very resistive: this results in a higher power needed by the HCT. On the other hand the internal gas pressure increases enhancing the performance in terms of thrust and *Isp* as already shown by Gessini [6] who demonstrated that, fixing the HCT geometry and working point, a smaller orifice led to an *Isp* almost twice higher.

II.1.1. The HCT Regions

The HCT is conventionally separated into three plasma regions: the insert, the orifice and the plume region.

The insert region of a HCT is the cylindrical region that accepts electrons emitted from the insert by the thermionic emission process. Thermionic emission describes the process for which an electron in a metal can escape its surface by increasing its vibration energy. The minimum amount of energy needed by the electron, which has to overcome the electrostatic force bounding it on the metal surface, is measured in eV and is called work function. The electron-emission of the insert in a HCT is dominated by the field-enhanced thermionic emission. The high current density obtained from the emitter surface (4-10 A/cm²) can be explained by the presence of a high electric field at the emitter surface that enhances the normal thermionic emission. The thermionic current density can be calculated with the Richardson-Dushmann equation:

$$J_{th} = A_{th} T_{ins}^2 \exp\left(-\frac{q\phi}{kT_{ins}}\right) \tag{1.15}$$

where A_{th} is the thermionic emission constant, T_{ins} is the emitter surface temperature and ϕ is the work function. In presence of an electric field E perpendicular to the surface the work function is reduced to an effective value ϕ_{eff} according to what is known as the Schottky effect [36]:

$$\phi_{eff} = \phi - \sqrt{\frac{qE}{4\pi\varepsilon_0}} \tag{1.16}$$

Emitted electrons ionize the gas fed from the upstream creating a plasma. It is important to stress that the plasma does not reach the upstream end of the insert. In this context an important parameter is the active length of the insert L_{act} , which defines the active region, i.e. the volume circumscribed by the emitting portion of the insert [37]. It influences the insert temperature and consequently the particle and power fluxes to the plasma. Its value depends on the set-point and it is always only a small part of the whole insert: for instance, the active length of the NSTAR cathode operating at TH15 is 1.7 mm [35].



Figure 11 – Active region in the cathode

The orifice is the region through which the emitted electrons are extracted to the plume region and where the ionization fraction and particle densities are the highest [35]. The plasma in this region very collisional and resistive [35] due to the electron scattering with the heavy particles (ions and neutrals), and most of the produced heating goes to the surrounding walls.

The last region is the plume region, where the gas expands and converts its static enthalpy into direct kinetic energy. The plasma here is collisionless or in the transition to collisionless [35].

II.2. Experimental Investigations on HCs Operational Modes

It has already been stated that HCTs are very similar to HCs, with the only difference of the discharge current all driven to the keeper. It is very important then to understand why HCs have started to be used and their different working modes.

Tungsten filaments heated to 2600 K were used in the 1960s to produce electrons for the plasma discharge and neutralisation in ion thrusters. Hollow Cathodes arose since they could achieve higher current densities and longer lifetime whilst running with lower power. Therefore many tests have been conducted on HCs to empirically investigate the influence of cathode geometry on the discharge parameters [38-44]. These tests showed different modes of operation, which Csiky described for the first time as spot and plume mode [38, 45, 46]. The term spot mode refers to low and non-noisy voltages whereas the plume mode is characterized by higher, noisy and oscillatory discharge voltages. Siegfried and Wilbur [43] investigated the spot to plume mode transition and the difference in the plasma parameters. The main difference between the two modes was a sharp gradient in electron temperature and plasma potential measured in the plume mode 5-10 mm downstream the orifice in a region they called the free-fall region. In this short distance electrons are accelerated through a large potential difference with no significant collision processes. Their remarks where supported also by the different luminosity of the HC discharge: in the plume mode a lighter cloud is visible downstream the keeper, whereas only a luminous spot is visible in what is called spot-mode. Rudwan [47] described the luminous cloud in the plume, shown in Figure 12, and the effect of the mass flow

rate, discharge current and HC geometry on the transition from plume mode, shown in Figure 12-a), to spot mode, shown in Figure 12-e).

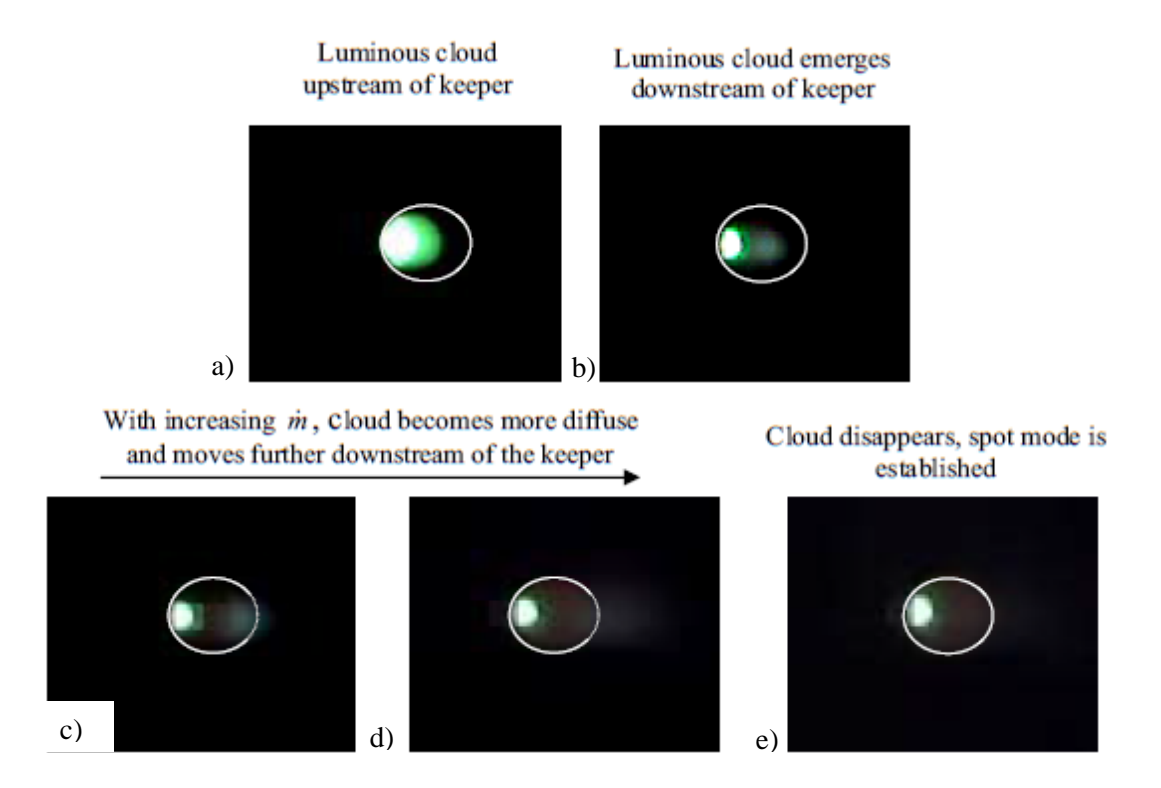


Figure 12 – Visual appearance of the HC discharge from a) plume to e) spot mode [47]

Fearn and Patterson [48-54] further investigated these operational modes with particular attention to discharge noise: they showed how the range of the spot operating mode can be extended when a keeper electrode is used and that the distance between the latter and the cathode orifice influences the voltage for the arc ignition. They also found another operating mode in diode configuration called neutralizer mode [55], which occurs at low discharge currents and mass flow rates and it is characterized by stable operation and relatively low temperatures but with significant noise generation in the discharge voltage.

In the HCT point of view the plume mode, and in general oscillatory discharge parameters, should be avoided in order to maintain stable performance and the overall thruster stability, if the HCTs are integrated in a larger subsystem.

II.3. Modelling of HCs/HCTs

Although no efforts in modelling a HCT to predict its performance in terms of thrust and Isp is in the open literature, many efforts have been made since the 1970s to model the physics of hollow cathodes. The modelling was initially an effort towards the prediction of the lifetime of HCs in order to avoid long and expensive tests. Kaufman [56] was the first to develop scaling laws for hollow cathodes in 1974. Siegfried and Wilbur [37] developed a 0D model for the insert region of mercury cathodes: their goal was that of predicting some of the operating parameters such as insert temperature and active length. They supposed the insert length, shown as L_e in Figure 13, to be between one and two primary electrons mean free path length. The model was developed with the purpose of allowing for a scaling of the device, to drive higher discharge currents without exceeding the maximum operating temperatures of the insert and surrounding materials.

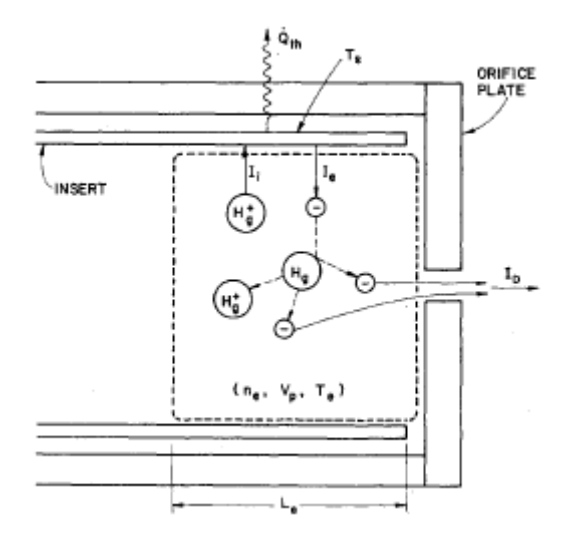


Figure 13 – Schematic of ion production region [37]

Salhi and Turchi [57, 58] developed a 0D model in which they assumed that the insert wall and the gas were at the same temperature while the neutral density was calculated using a two-temperature Saha equation. The model included a 2D variation of the plasma properties inside the cathode and ohmic heating with the classic (Spitzer) electrical conductivity for a fully ionized plasma. They showed that, given a certain discharge current, the hollow cathode with the smallest insert diameter capable of driving that current is the most efficient and ensures the

minimum discharge voltage. On the other hand, they showed that the working temperature is higher for smaller cathodes.

An effort in the modelling of the plasma inside HCs started in the late 1990s at the NASA Jet Propulsion Laboratory, when Katz et al [59] developed a model in which the orifice was treated as a cylinder containing homogeneous neutral plasma with a thin wall sheath. Their assumptions included the quasi-neutrality of the plasma and that ion loss rate was the product of the wall area and the ion thermal flux. They also assumed that the ions and the electrons were in thermal equilibrium as a result of assuming that a quasi-neutral electric field accelerates the ions toward the orifice boundary. The latter was a strong assumption which does not reflect the plasma behaviour in the HC and was removed during the improvement of the model in the following years. In fact in 2003, Katz et al [60] developed a 1D model for both insert and orifice region, including the chamfering. They started from the previous model [59] and from the observation that xenon ion mobility is diffusion limited due to the small mean free path for resonant charge exchange reactions compared to the orifice length. Some of the approximations were eliminated, such as ions having a Maxwellian velocity distribution with the electrons temperature and the use of temperature-independent electron-neutral cross section, making the tool closer to the real plasma mechanisms. In this model the ion motion is determined from the ambipolar equation, radiation losses are neglected (since the plasma is assumed to be optically thick and most of the radiation is trapped inside the plasma) and the inertial terms in the both the ion and electron momentum equations are also neglected. In order to model the emitter region they included the effects of collisions among ions and neutral and among electrons and neutrals. Most of the assumptions made within this model are extremely valid and are of significant interest for the development of the theoretical model carried out within this research.

Since 2005 *Mikellides et al* [61-65] have developed a 2D axisymmetric theoretical model for the whole HC, i.e. emitter, orifice and plume region as shown in Figure 14, which shows the plasma density in the three different regions for two different HCs. In the model inertia terms in both the ion and electron momentum equations were neglected and the ions and neutrals are assumed to be in thermal equilibrium. This model consists, for the first time, in the solution of the full conservation

equations system describing the multicomponent fluid and it is the most complete model to date.

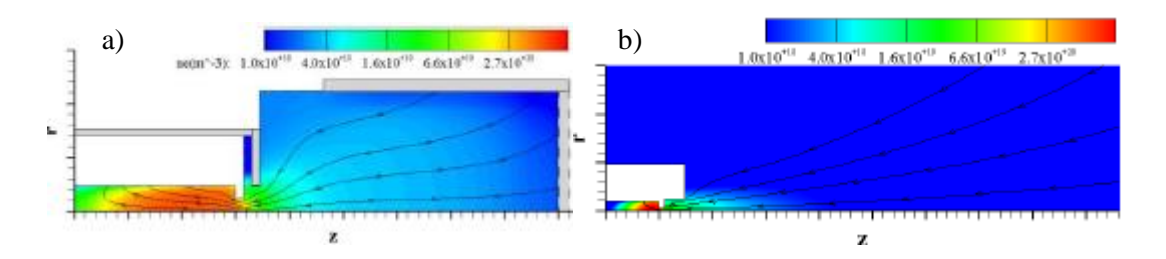


Figure 14 – Plasma density for two different HC geometries [65]

All of the theoretical models have been developed with the aim of predicting the plasma parameters evolution inside the hollow cathodes to mainly predict lifetime. None of the models developed up to now have been used to predict the performance of the HCTs in terms of thrust and the specific impulse not for an optimization of such a device. The 2D theoretical tool developed by *Mikellides et al* [61-65] could be used in principle to predict the thrust and *Isp* since it models all the plasma regions, but it is not freely available.

II.3.1. Modelling of HCTs with External Applied Magnetic Field

Models to predict the effect of an externally applied magnetic field on a Magneto Plasma Dynamic Thruster have been developed by *Fradkin* [66], *Sasoh* [67], *Mikellides* and *Turchi* [68] and *Coletti* [69]. These models are of particular interest since they might be used for HCTs application with an external magnetic field, as MPDs and HCTs present similarities in the geometry.

II.3.2. Modelling of Arcjet Constrictors

The constrictor is that narrow passageway in an arcjet between the cathode and the anode where the arc current passes through before attaching to the anode/nozzle walls, as shown in Figure 15.

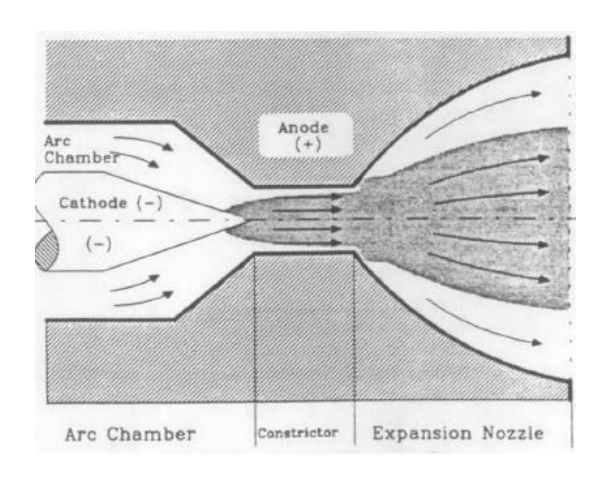


Figure 15 – The constrictor region in an Arcjet [70]

The configuration of the hollow cathode orifice is very similar to that of the arcjet constrictor. Many efforts have been made to model the physics of the plasma in arcjet thrusters. A first attempt was made at NASA Lewis [71], where the flow in the constrictor was divided into two regions with homogeneous properties. Based on the idea of dividing the flow in the constrictor into different regions with different properties, such as temperature and velocity, a dual-channel model was derived by *Glocker* [72], who further improved the model until a three channel model was developed [70]. The introduction of different flow regions with different properties may better reflect the change in the radial properties of the flow. Nevertheless its complexity would be beyond the aim of the model for the current research, which it is meant to be a simple and effective way to calculate the performance of HCTs.

II.4. Previous Work on HCs/HCTs Thrust Measurements

No direct thrust measurements on HCs/HCTs are available in the open literature. The first experiments on HCTs to obtain the performance by the employment of a direct thrust balance have been carried out within this research project. To perform reliable thrust measurement a direct thrust balance was designed, commissioned and developed within this research. Direct thrust measurements are performed typically using hanging [73, 74] and inverted or torsional pendulums [75, 76]. The configuration developed within this research is a hanging pendulum, which was preferred to that of a null-reading balance because it allows for the using of a real-time acquisition method that, together with the selected balance design, allows for the cancellation of the thermal drifts.

Up to now, thrust measurements on HCs/HCTs have been performed with indirect thrust balances only, where the displacement of a target, due to the impinging plume, is the measure of the thrust. The thrust data obtained with indirect target thrust balances need to be corrected to take into account the effect of the collisions between the propellant flow and the target balance. The indirect to direct thrust ratio ψ is very helpful in this context; it is a key parameter in every indirect thrust measurement system because it corrects the measured thrust value taking into account the effect of collisions between the thruster plume and the thrust balance target.

$$\psi = \frac{Indirect \quad Thrust \quad Measurement}{Direct \quad Thrust \quad Measurement} \bigg|_{\stackrel{\bullet}{m}}$$
(2.1)

With an indirect thrust balance where a target is used, the propellant particles once ejected from the thruster will hit the target. Depending on the kind of collision the measured thrust will overestimate the real thrust value [5, 14, 77]. The two extremes are represented by non-elastic collisions and by elastic collisions where the particles are reflected 180° (hence exactly in the opposite direction to the one they came) after hitting the target.

If the collisions between the jet particles and the target are non-elastic, the particles will transfer to the target all their momentum hence producing a measured thrust that is equal to the actual thrust. In this condition the parameter ψ will be equal to one. The ψ ratio will be equal to one also if the deflection angle of the particles after hitting the target results in 90°, as shown in Figure 16, because of the conservation of the momentum vector.

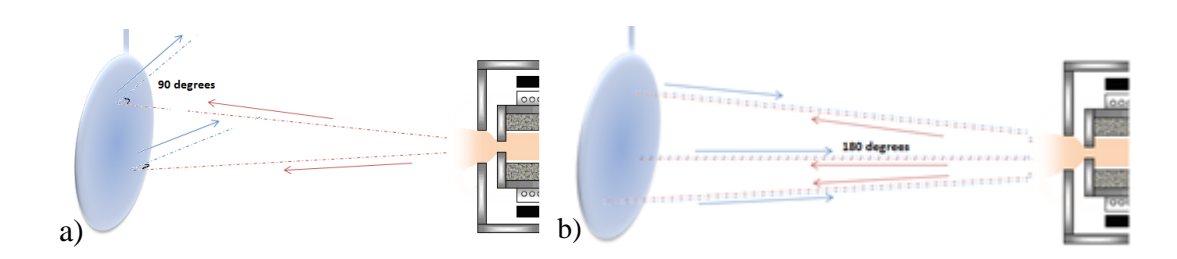


Figure 16 – a) Inelastic and b) elastic collisions of particles against the target

If instead the collisions are elastic with 180° reflection, for the conservation of momentum the particles will transfer to the target twice their momentum hence producing a measured thrust that is twice the actual value.

It should be noted that when performing indirect thrust measurements, the values of ψ and/or the actual thrust are unknown. Only assumptions and comparison to theoretical values, if available, can be made.

Snyder and Banks at NASA Lewis [78] were the first to perform thrust measurements in 1972, on a HC in the discharge mode to understand the impact of the HC thrust on the SERT II ion thruster thrust vector. They used a synthetic mica target on a torsion pendulum to collect the thrust from a mercury HC which had a barium carbonate coated insert of 3.2 mm of diameter and a orifice diameter of 0.25 mm.

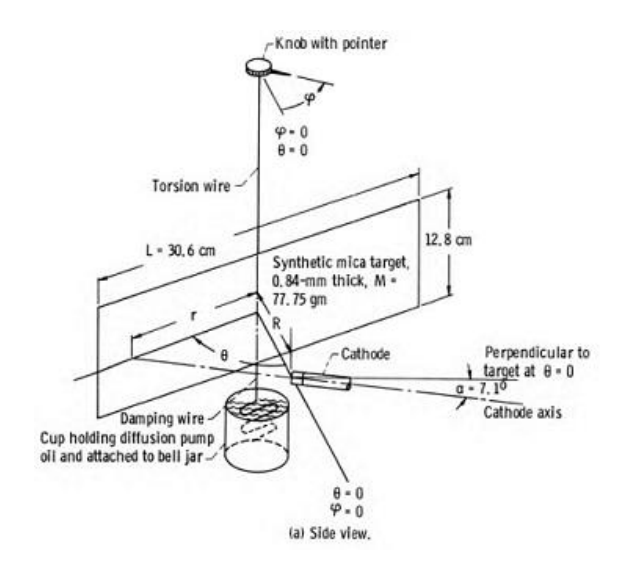


Figure 17 – The pendulum used in [78]

The thrust increased with mass flow rate, discharge power and tip temperature (that was measured with an optical pyrometer). With no keeper discharge and at a target angle of 10 degrees, at the nominal operating conditions of 47 mA of equivalent neutral flow and tip temperature of 1100 K, the measured thrust was between 52 μ N (corrected with ψ =1) and 26 μ N (corrected with ψ =2). The former overestimated the thrust theoretically predicted with a sonic flow at the cathode tip temperature while the latter led to an underestimation of the theoretical value. A thrust close to the theoretical value was obtained by applying a correction factor of ψ =1.5. With the

keeper discharge on, i.e. in discharge mode, at 0.75 A and 19 V with the same flow rate, tip temperature and target angle, the measured thrust was about 66.4 μ N (corrected with ψ =1).

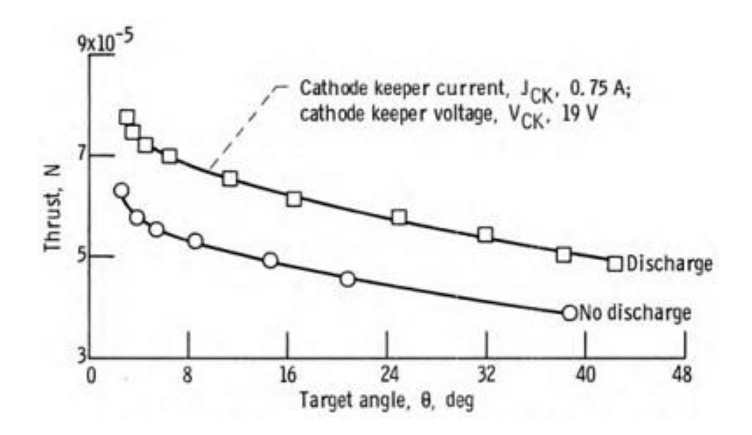


Figure 18 – Measured cathode thrust as a function of target angle [78]

Gessini at the University of Southampton [6] tested a T6 HC with an orifice diameter of 0.5 mm later increased to 1 mm and tested again. He used an indirect thrust balance with a cantilever beam and laser-optical-lever system, which suffered thermal drift problems caused by the differential expansion of the cantilever beam. He obtained thrust measurements with krypton, argon and xenon. In particular, thrust measurements with xenon were ranging 0.36-5 mN with *Isp* ranging 57-478s [6], showing that the smaller orifice led to an *Isp* almost twice higher than the bigger one, as shown in Figure 19. The thrust measured was not corrected to take into account the interaction between the target and the impinging plume.

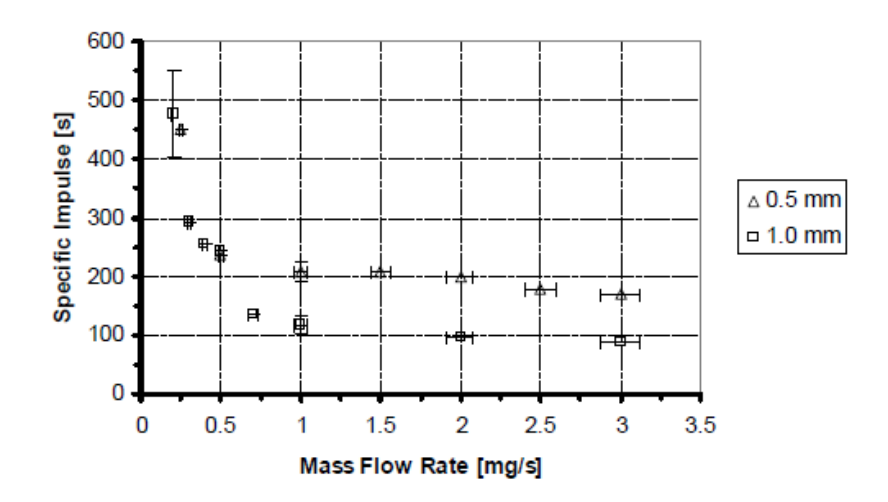


Figure 19 – Isp measured on a T6 HCT varying the orifice diameter with xenon at 25 $\,$ A [6]

He also showed that a transition from spot to plume mode occurs when decreasing the mass flow rate under a characteristic value at a constant discharge current as shown in Figure 20. This characteristic value depends on the gas, the discharge current and the HCT geometry.

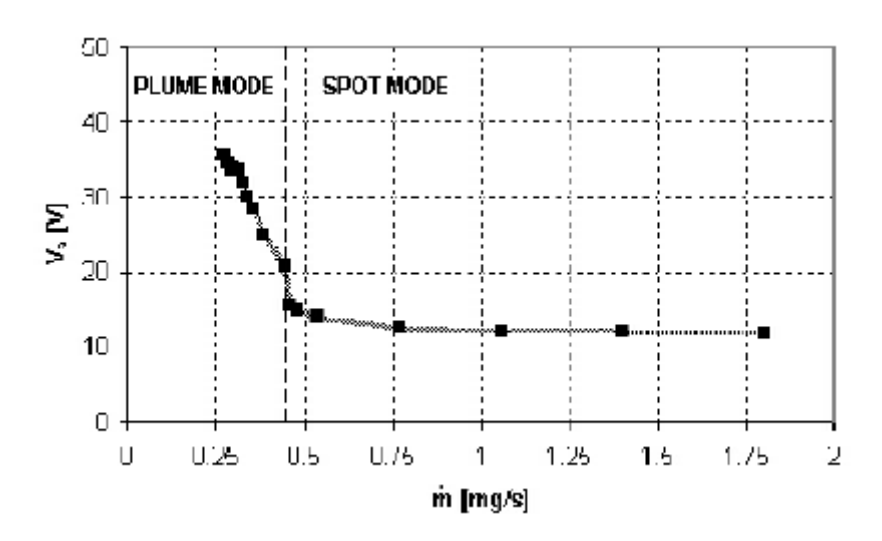


Figure 20 – Plume-to-spot mode transition with argon at 12 A on a T6 HCT [6]

Gessini was followed by *Grubisic* [12, 14], who designed and commissioned a new indirect thrust balance at the University of Southampton to collect thrust measurements from both the T5 and T6 HCs. He used a pendulum consisted of a circular target which position was monitored thanks to a He-Ne laser driven into the chamber and reflected by a mirror, connected to the target, to a two-dimensional tetra-lateral photo-sensitive detector. His research again showed the transition from spot to plume mode and that the thrust increases with mass flow rate and discharge current. As shown in Figure 21, a thrust up to 0.7 mN with an *Isp* of 70 s was measured with 1 mg/s of Argon in cold gas mode [12] whereas in resistojet mode a thrust up to 1.3 mN with an *Isp* of 110 s was measured with 1.2 mg/s of Argon [12]. With xenon the thrust measured in cold gas mode was in the range 0.22-0.43 mN with an *Isp* ranging 27-31s [12]; in resistojet mode, with the heater at 50W, the thrust measured was 0.1-0.58 mN with an *Isp* ranging 29-38s [12].

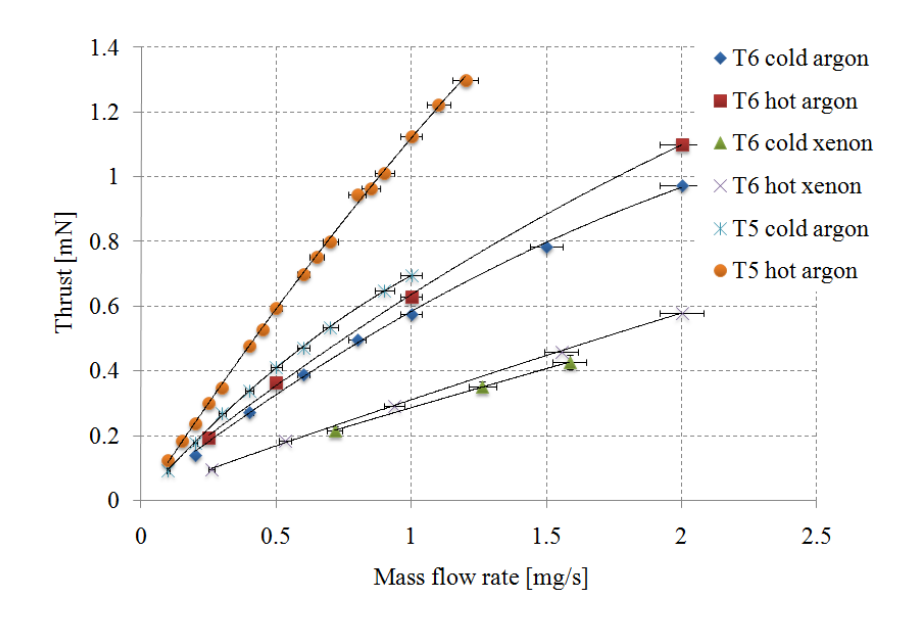


Figure 21 - Thrust obtained in operation of the T5 and T6 cathodes in hot and cold gas mode [12]

In discharge mode a thrust up to 2.5 mN, as shown in Figure 22, and Isp up to 650 s was measured with argon, with a thruster efficiency in the range 1 - 14 % [6, 12] whereas with xenon thrust was up to 1.5 mN, Isp up to almost 1000 s and thrust efficiency always below 0.30% [6, 12], as shown in Figure 23.

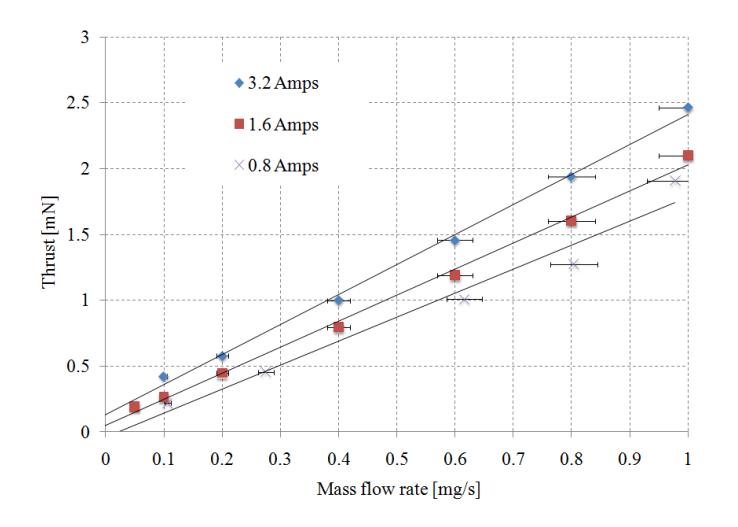


Figure 22 - Thrust for the T5FO cathode with argon [12]

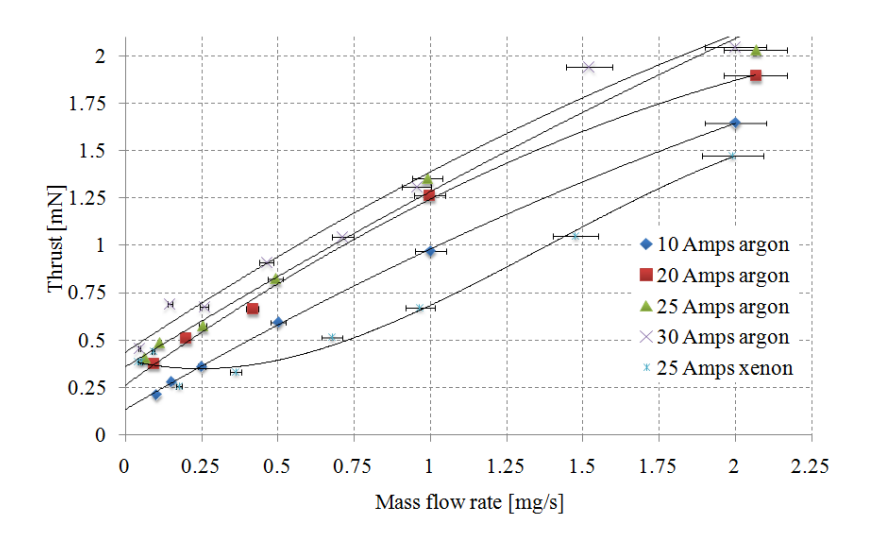


Figure 23 - Thrust for the T6 HCT with argon and xenon [12]

Grubisic did not correct the presented measured thrust. On the other hand he tried to find a value for ψ by comparing the theoretical thrust with the measured thrust values obtained with xenon and argon in cold and resistojet modes. He found an accommodation coefficient (measured to theoretical value) ranging from 1.08 to 0.28, shown in Figure 24. He suggested that the values <1 could arise from the fact that the plume was expanding at a high divergence angle.

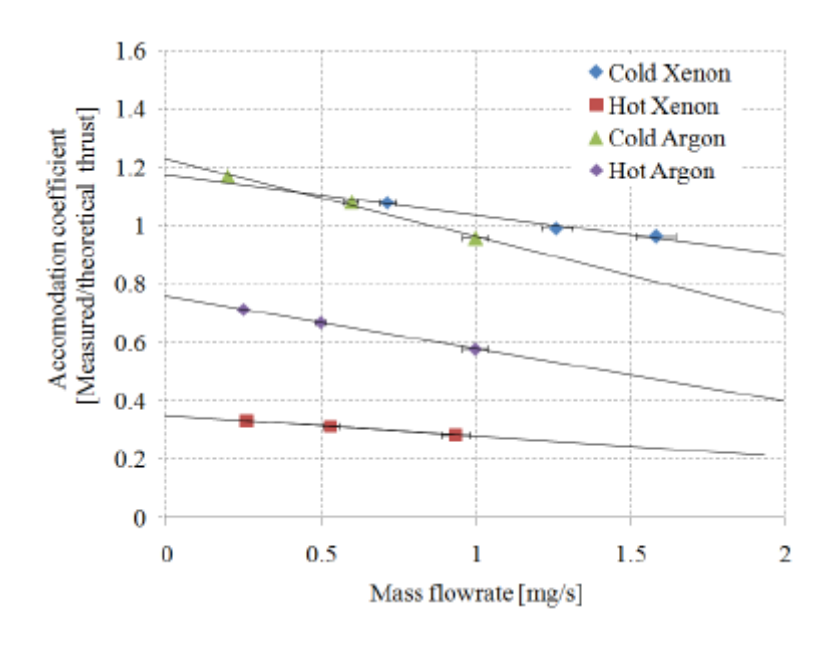


Figure 24 – Comparison between theoretical and measured thrust [12]

Considering that in [6, 12] an indirect thrust balance system has been used, depending on the type of these collisions (elastic or inelastic) the previous data could be overestimated of up to 100%.

II.5. Theoretical Thrust Mechanisms

The physical processes which may contribute to the generation of the thrust are:

- Heavy particles gasdynamic contribution
- Electrons gasdynamic contribution
- Electromagnetic thrust
- High energy ion production

II.5.1. Heavy Particles Gasdynamic Contribution

The heavy particle (ions and neutrals) gasdynamic contribution $F_{h,gas}$ is the thrust contribution relative to the ions and neutrals exit velocity and pressure. This contribution can be expressed as [24]:

$$F_{h,gas} = \dot{m}_i u_i + \dot{m}_n u_n + (p_i + p_n - p_{ext}) A_{ex}$$
 (2.2)

Where \dot{m} , u and p are respectively the mass flow rate, velocity and pressure of the specie (the subscripts n and i indicate respectively neutrals and ions), p_{ext} is the external pressure and A_{ex} the exit cross-sectional area. Equation (2.2) can be applied to a HCT: being in general the mass flow rate $\dot{m} = \rho u A$ and the density $\rho = mn$ and being $p_{ext} = 0$ in open space, it is possible to write:

$$F_{h,gas} = \left(m_i u_i^2 n_i + m_n u_n^2 n_n\right) A_{ex} + p_i A_{ex} + p_n A_{ex}$$
 (2.3)

where m and n are respectively the mass and the particle density of the specie. This mechanism of thrust production was already discussed in [12].

II.5.2. Electrons Gasdynamic contribution

The electron gasdynamic contribution is the thrust relative to electrons exit velocity and pressure and it can be written following what has already been done for the heavy particles as:

$$F_{e,gas} = (m_e u_e^2 n + p_e) A_{ex}$$
 (2.4)

The subscript e in equation (2.4) indicates electrons. This contribution can be neglected since most of the electrons emitted by the cathode will be collected at the anode/nozzle (or keeper depending on the configuration) hence no net force can be produced on the HCT assembly since electrons and HCT body form a closed system. The only electrons escaping the HCT are the ones needed to maintain quasineutrality of the plume. On the assumption that only single charged particles are in the plasma, assuming the limiting case where the propellant is fully ionized the flux of ions leaving the HCT will be equal to the mass flow rate expressed in Amperes I_{eq} hence:

$$I_{eq} = \frac{q\dot{m}}{m_h} \tag{2.5}$$

Where q is the electron charge, m_h is the mass of the heavy particles and \dot{m} is the total mass flow rate. To maintain quasi-neutrality the flux of electron leaving the HCT will hence be equal to I_{eq} . In Figure 25 the value of I_{eq} , calculated with equation (2.5), is reported for different mass flow rates.

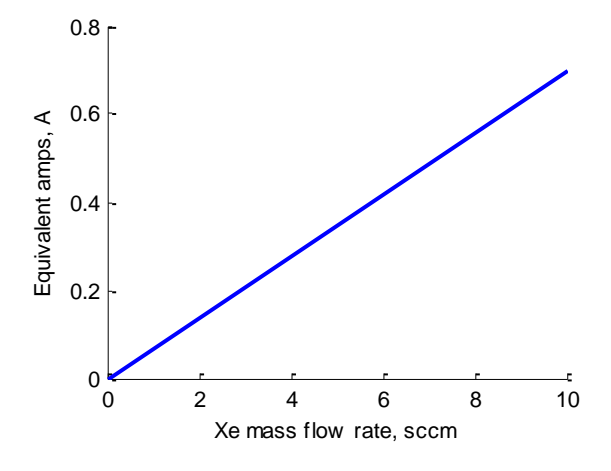


Figure 25 - Equivalent amps in a HCT

As it can be seen, even assuming the limiting case of a fully ionized propellant, the value of I_{eq} is always below 1 A (for mass flow rates up to 10 sccm of xenon) and in particular looking at mass flow rates up to 4 sccm is lower than 0.3 A. This means that assuming a 100% ionized flow and assuming a T5 HCT running at 4 sccm and 3 A of discharge current, only 10% of the electrons exiting from the orifice will leave

the HCT. This will proportionally decrease with the ionization fraction hence if the propellant flow is 10% ionized only 1% of the electrons exiting the orifice will leave the HCT. This fraction further decreases with discharge current hence for a T6 HCT this fraction will be even smaller (i.e. 0.1% for a 30 A, 4 sccm T6 HCT with 10% ionization fraction). The gasdynamic electrons pressure contribution was discussed to be able to produce an important thrust level [12], with electron temperature being responsible for producing such a high electron pressure.

II.5.3. Electromagnetic Thrust

In the hypothesis of continuum flow regime, the electromagnetic force is generated by the crossing of the self-generated azimuthal magnetic field with the arc current through the cathode orifice and keeper or anode/nozzle. Considering the HCT as an MPD and following the analytical treatment presented in [23] integrating the magnetic stress tensor over the two control volumes indicated by the dashed and dotted lines in Figure 26 the electromagnetic force F_{em} produced can be expressed as:

$$F_{em} = \frac{\mu_0 I_D^2}{4\pi} \ln \left(\frac{R_a}{R_c}\right) \tag{2.6}$$

Where I_D is the discharge current, μ_0 is the vacuum magnetic permeability, R_c is the cathode radius and R_a is the keeper or anode/nozzle radius calculated at the current attachment point as shown in Figure 26.

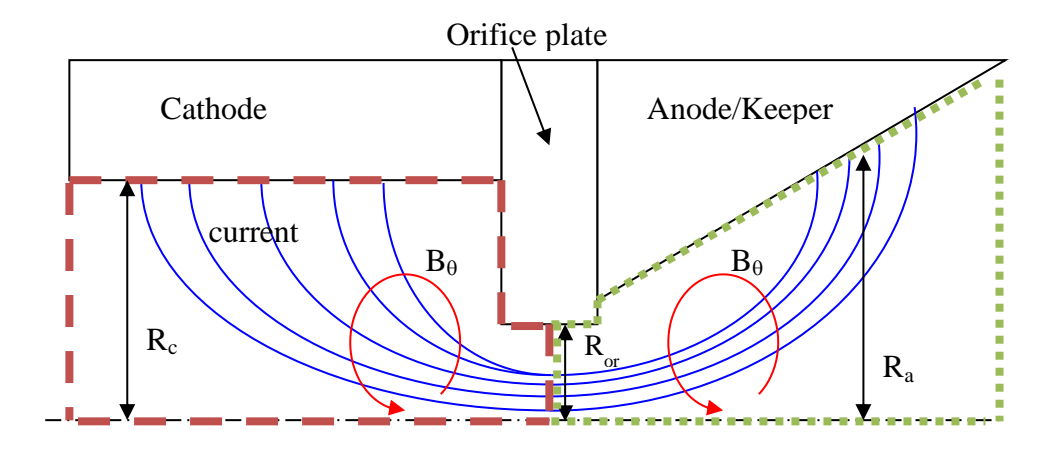


Figure 26 - Sketch for the determination of the electromagnetic thrust contribution

Following what has been done in [23] and considering the upstream part of the domain enclosed in the dashed lines in Figure 26, the electromagnetic force is directed towards the upstream end of the cathode and has an absolute value of:

$$F_{em}^{dashed} = \frac{\mu_0 I_D^2}{4\pi} \left[\ln \left(\frac{R_{or}}{R_c} \right) + \frac{1}{4} \right]$$
 (2.7)

where R_{or} is the orifice radius. Considering now the downstream part of the domain enclosed in the dotted lines in Figure 26, the electromagnetic force is instead directed towards the downstream end of the cathode and has an absolute value of:

$$F_{em}^{dotted} = \frac{\mu_0 I_D^2}{4\pi} \left[\ln \left(\frac{R_a}{R_{or}} \right) + \frac{1}{4} \right]$$
 (2.8)

The vector sum of equations (2.7) and (2.8) gives the total electromagnetic thrust, which has a direction towards the downstream end of the cathode and a value given by:

$$F_{em} = -F_{em}^{dashed} + F_{em}^{dotted} = \frac{\mu_0 I_D^2}{4\pi} \ln \left(\frac{R_a}{R_c} \right)$$
 (2.9)

The extent of the electromagnetic contribution to the total thrust was already investigated in [10], where the contribution given by equation (2.8) was neglected hence overestimating it.

II.5.4. High Energy Ions Production

Many experiments showed the production of high energy ions (HEI) during HCs discharges [79-83], with *Rawlin* [84] observing for the first time HEI from the hollow cathode with energies above the discharge potential. Before delving into the topic, there is the need to make a distinction between the high energy ions accelerated from the internal parts of the cathode to the exit, which may contribute to the thrust, and those accelerated back from the plume, which cause erosion of the HCT and may contribute with a negative thrust. High energy ions production mechanisms were proposed to be due to potential-hills [85], orifice pinch [80], plasma potential oscillations [63, 86] and ion acoustic turbulence [65, 87]. The potential hill phenomenon was introduced by *Friedly* and *Wilbur* [81] and suggests the creation of a region of positive potential in the plasma higher than that of the

keeper which would let the ions accelerating. The orifice pinch model postulated by Latham [80] explains the HEI as the result of a magnetohydrodynamic effect in the orifice region. The most comprehensive investigation of high energy ions production mechanisms was carried out at JPL [63, 86], where a possible cause was proposed to be discharge plasma potential oscillations with amplitudes about twice the average discharge voltage, large enough to let the ions accelerate through the potential gap between this oscillation peaks. Recently it was proposed that the main cause of high energy ions production may be instead the onset of ion acoustic turbulence [65, 87].

Experiments performed on the XIPS cathode with xenon [12] showed that the distribution of the high energy ions is similar to a Maxwellian one, with ion energy peaks significantly high (about 60 eV), decreasing with mass flow rate and discharge current. In [12], using a discharge current of 16 A and a mass flow rate of 2.05 sccm of Xenon, the collected high energy ion current was calculated to be 0.275 mA: this represents a mass flow rate of 3.75E-4 mg/s that, assuming an average ion energy of 80 eV, leads to a net thrust F_{HEI} of about 4 μ N, which has been calculated as:

$$F_{HEI} = \frac{I_{HEI} m_i}{q} u_{HEI} \tag{2.10}$$

where I_{HEI} is the high energy ion current and m_i and u_{HEI} are respectively the mass and the velocity of the ions, with the latter assumed to be [12]:

$$u_{HEI} = \sqrt{\frac{2q\overline{E}_{HEI}}{m_i}}$$
 (2.11)

where \bar{E}_{HEI} is the average energy of the ions, 80eV. The results reported in [12] indicate that at present the thrust that can be extracted from this process is so small that can be neglected and can contribute only as a small source of thrust noise.

Chapter III

The Theoretical Model

In this chapter a full description of the theoretical model developed within this research is given. The model is intended to predict the performance of HCTs in terms of thrust, Isp and needed power. It simulates the plasma inside the insert and orifice region of the HCT and the gasdynamic expansion of the propellant inside the anode/nozzle. It is comprised of three sub-models:

- a 0D model developed at JPL [35] for the plasma in the insert region, encircled by red lines in Figure 27;
- a 1D model developed within this research activity for the plasma in the orifice region, encircled by green lines in Figure 27. This part of the model is divided into two sub-models, one for the straight part and one for the diverging part of the orifice. The latter includes also the insulation part since the discharge arc extends through it up to the initial cross sections of the nozzle and takes part in the heating of the plasma.
- a classic 1D gasdynamic model for the expanding gas in the nozzle, encircled in blue lines in Figure 27.

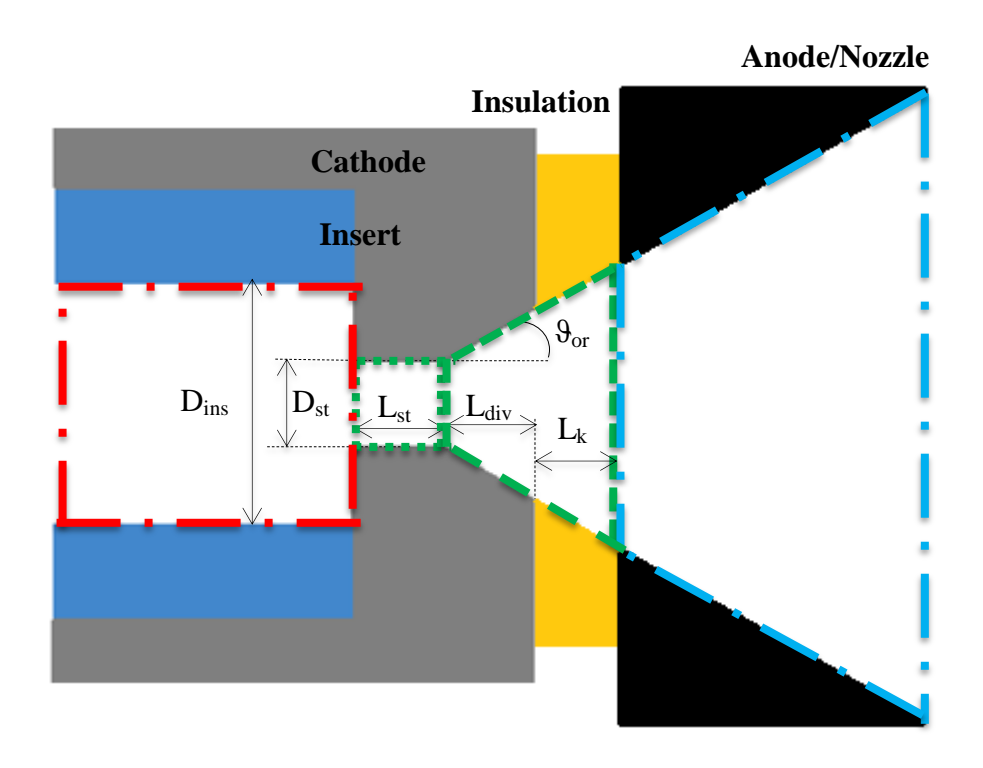


Figure 27 - HCT geometry and domain region

In the following paragraphs a full description and discussion of each of the submodels will be given, starting from the definition of the geometry of the HCT.

III.1. Inputs and Outputs

The theoretical model for the whole HCT needs as inputs the complete geometry of the device, the set-point at which it runs (discharge current and mass flow rate), and three parameters needed for the 0D model for the insert: the insert heat losses H, the ratio between the heavy particles and the wall temperature β , and the active length of the insert L_{act} . The insert heat losses H depends on the power level and the heat shield of the HCT and can be found with the use of thermal models. The model gives as outputs the predicted thrust and the Isp at the set-point, and for each submodel gives the values of the plasma parameters as schematically shown in Figure 28.

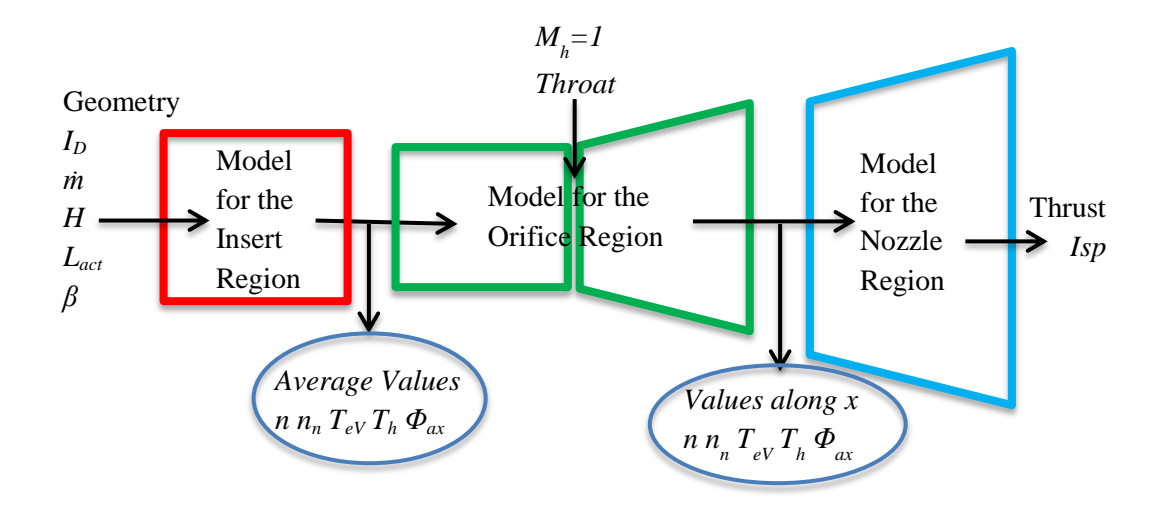


Figure 28 – Inputs and outputs in the model

For the geometry, the insert diameter (D_{ins}) needs then to be defined together with the orifice geometry: it is possible to choose a fully straight, fully diverging or part straight and part diverging orifice. Depending on the case, it is possible to design the shape of the orifice by setting:

- the length (L_{st}) and diameter (D_{st}) of the straight orifice;
- the length (L_{div}) , initial diameter (D_{st}) and divergence angle (θ_{or}) of the diverging orifice;
- the length (L_{st}) and diameter (D_{st}) of the straight part and the length (L_{div}) and divergence angle (θ_{or}) of the chamfered part of the orifice

After the exit section of the orifice it is also possible to design a nozzle deciding the diameter of the upstream section (D_{noz}) , the divergence angle (θ_{noz}) , the nozzle length (L_{noz}) and the spacing between the cathode orifice tip and the nozzle (L_k) .

The inputs to the theoretical model are summarised in Table 5:

Table 5 – Geometry variables which can be defined in the model

Variable			
D_{ins}	Insert Cathode Diameter		
D_{st}	Orifice Diameter (straight part)		
L_{st}	Orifice Length (straight part)		
L_{div}	Orifice Length (divergent part)		
$artheta_{or}$	Orifice Divergence Angle		
L_k	Cathode-Nozzle Spacing		
D_{noz}	Nozzle Upstream Diameter		
L_{noz}	Nozzle Length		
$artheta_{noz}$	Nozzle Divergence Angle		
I_D	Discharge Current		
ṁ	Mass Flow Rate		
H	Insert Heat Loss		
L_{act}	Active Length		
	Heavy particles to wall		
β	temperature ratio		

III.2. The Theoretical Model for the Insert Region

The plasma in the insert region is modelled using the model developed at JPL by Goebel and Katz: an overview of the model is given in this paragraph, whereas a full description can be found in [35]. The inputs to the model are the insert diameter D_{ins} , the diameter D_{st} and length L_{st} of the straight part of the orifice, the HC operating conditions (discharge current and mass flow rate), the insert heat losses H, the ratio between the heavy particles and the wall temperature β , and the active length of the insert L_{act} . The first equation is the solution to the steady-state ions diffusion equation for cylindrical geometries, from which the electron temperature can be obtained [35, 60]:

$$\left(\frac{D_{ins}/2}{B_{01}}\right)^{2} n_{n} \sigma_{ion} \sqrt{\frac{8kT_{e}}{\pi m_{e}}} - \frac{q}{m_{h}} \frac{T_{hV} + T_{eV}}{\sigma_{ce} n_{n}} \sqrt{\frac{m_{h}}{kT_{h}}} = 0$$
(3.1)

where B_{0I} is the first zero of the zero-order Bessel function, n_n is the neutral density and T_e and T_h are respectively the electrons and heavy particles temperature in Kelvin (or expressed in eV when the subscripts V is used). In equation (3.1) σ_{ion} and σ_{ce} are respectively the ionisation and the charge exchange cross section, m_e and m_h are respectively the electrons and heavy particles mass and k is the Boltzmann constant. Equation (3.1) is obtained in [35, 60] from the observation that axial ion density gradients are small inside HCs and the assumption that the generated ions must equal those lost, which phenomenon is described by the diffusion rate to the walls. The second equation is the conservation of the current [1]:

$$I_{D} = I_{th} + I_{iw} - I_{ew} ag{3.2}$$

where I_D is the total discharge current and I_{th} , I_{iw} and I_{ew} are respectively the thermionic current and the ion and electron currents flowing back to the insert walls as shown in Figure 29.

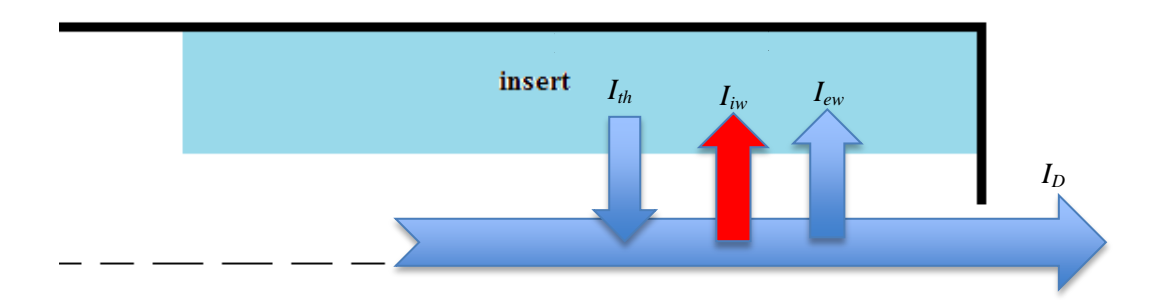


Figure 29 – Currents in a HCT

In the plasma bulk the heating of plasma, due to the resistive heating $(\Re I_D^2)$ and electron bombardment from the insert $(I_{th} \phi_{sh})$, is balanced by the energy loss, due to ions and electrons lost to the walls and to the convection of Maxwellian electrons flowing away the insert region through the orifice. The third equation is then the power balance in the cathode plasma [35]:

$$\Re I_D^2 + I_{th}\phi_{sh} = I_{iw}\varepsilon_i + \frac{5}{2}T_{eV}I_D + (2T_{eV} + \phi_{sh})I_{ew}$$
(3.3)

where \Re is the resistance of the plasma, ϕ_{sh} is the voltage drop across the sheath and ε_i is the first ionisation potential of the gas. The fourth equation is an equation for the cathode sheath voltage, obtained by combining an equation for a power balance at the insert with equations (3.2) and (3.3) [35]:

$$\phi_{sh} = \frac{H}{I_D} + \frac{5}{2}T_{eV} + \phi_{wf} - \Re I_D$$
 (3.4)

where Φ_{wf} is the insert work function. The fifth equation is obtained assuming a Poiseuille flow inside the orifice, from which the neutral density can be found [35]:

$$p_1 = \sqrt{p_2^2 + \frac{0.78\dot{m}\,\varsigma\,T_r L_{st}}{D_{st}^4}} = n_n \,k\,T_h \tag{3.5}$$

where \dot{m} is the mass flow rate (in sccm in this case), p_1 and p_2 are respectively the pressure upstream and downstream of the cathode orifice in torr; ζ is the viscosity in poises and T_r is defined as [35]:

$$T_r = T_h(K)/289.7$$
 (3.6)

The output given by this model are the neutral and plasma densities n_n and n, the electron and heavy particle temperatures T_e and T_h and the voltage at the sheath ϕ_{sh} . It is also important to know the plasma potential on the axis at the orifice entrance ϕ_{cat} (with respect to the emitter potential) since it will be used as an input to the 1D model for the orifice, which will be discussed in the next paragraph. Although ϕ_{cat} is not calculated in [35], an estimation of it can be done assuming that ϕ_{cat} is the sum of three main contributions: the voltage drop across the sheath at the emitter wall, the resistive ohmic heating in the insert region and the voltage drop from the plasma bulk to the sheath. The latter can be estimated as half the electron temperature [35] in agreement with the experimental results on the NSTAR cathode [35].

III.3. Theoretical Model for the Orifice Region

The model for the orifice developed is a 1D model based on the plasma dynamic equations and applied to a steady flow in the most general conditions, including the variation of the cross sectional area. It is a 2-fluid model, where the heavy particles (ions and neutrals) and electrons are treated independently. The simulation domain is divided into two sub-regions: the straight part of the orifice and the diverging part.

III.3.1. Assumptions

The assumptions are that the plasma is quasi neutral $(n_i=n_e=n \text{ where } n_i \text{ and } n_e \text{ are in general the density of respectively ions and electrons and } n \text{ is what is known as plasma density)}$ and only single charged particles are in the plasma, that the ions and neutrals (heavy particles) are in thermal equilibrium [88] $(T_i=T_n=T_h \text{ where } T_i \text{ and } T_n \text{ are in general the temperature of respectively ions and neutrals)}$ and have the same group velocity $(u_i=u_n=u_h \text{ where } u_i \text{ and } u_n \text{ are in general the velocity of respectively ions and neutrals)}$, that the heavy particles are in sonic conditions at the final section

of the straight part of the orifice [62] and that the Mach number of the electrons M_e does not change significantly in the orifice (M_e =const). The electrons Mach number is defined as:

$$M_e = \frac{u_e}{\sqrt{\frac{5}{3}T_e \frac{k}{m_e}}} \tag{3.7}$$

where u_e is the electrons group velocity, m_e and T_e are respectively their mass and temperature and k is the Boltzmann constant. A further discussion on each of the assumptions is given in the following paragraphs.

III.3.1.1. Equilibrium Between Heavy Particles

The collisions between heavy particles are mainly resonant charge exchange collisions (CEX), where a neutral becomes an ion and vice versa both maintaining their relative temperature and velocity [77]. If a high number of charge exchange collisions exist in the orifice, ions and neutrals can hence be considered in equilibrium. The mean free path λ_{ce} for this type of collisions, shown in Figure 30 for different values of n_n , is defined [61, 77] as the inverse of the product of the neutral density n_n and the CEX cross section σ_{ce} (100 Å² for xenon [89]).

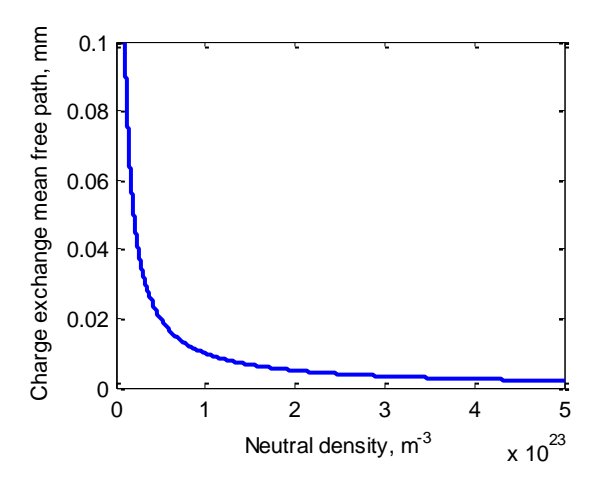


Figure 30 - Charge exchange mean free path in the orifice

Figure 30 shows that the typical length of the orifice (1 to 2 mm) is much greater than λ_{ce} , hence the equilibrium among ions and neutrals will quickly be reached. For example, numerical predictions showed an average neutral density of n_n of $2x10^{23}$

m⁻³ in the orifice of the NSTAR neutralizer cathode [60]; for a T5 sized HCT at 2.5 A and 2.5 sccm a similar value has been calculated with the model presented in this research study. According to Figure 30 the charge exchange mean free path in the orifice, for both the T5 HCT and the NSTAR, is λ_{ce} =0.005 mm with such a value of n_n . The charge exchange mean free path is much smaller than the total length of the orifice, which is of the order of 1 to 2 mm for the T5 [12], and 0.75 mm for the NSTAR [60] hence it is then reasonable to assume equilibrium among ions and neutrals for what concerns the temperature and the group velocity. The model is then built as a 2-fluid model, the electrons and the heavy particles (ions and neutrals) are treated as two independent fluids.

III.3.1.2. Constant Electron Mach Number

The Mach number of the electron is considered constant and fixed at its value at the orifice inlet. Following the analysis presented in [24], hence combining the mass, momentum and energy equations for ions and neutrals with the definition of the Mach number (equation (3.7)) and the ideal gas law, a general equation for the rate of change of the Mach number can be found:

$$\frac{dM}{dx} = \frac{M(1+\delta M^2)}{(1+M^2)mnuA} \left[-\frac{1}{A} \frac{dA}{dx} + \frac{1+\gamma M^2}{2} W - \gamma M^2 \frac{1+\gamma M^2}{u} X + \frac{1+\gamma M^2}{2h_0} Y \right]$$
 (3.8)

where W, X and Y are the mass, momentum and energy source terms respectively and $\delta = (\gamma - 1)/2$. The Mach number in the model is defined as for a fluid, i.e. the ratio between the fluid velocity and the speed of sound $a = \sqrt{\gamma k T/m}$ since equation (3.8) is derived starting from fluid equations. Equation (3.8) has been applied to the cylindrical orifice of a T5 HCT running on argon at 3.2 A and the NSTAR cathode running on xenon at TH8 to study in first approximation the trend of the electron Mach number. Reasonable values have been assigned to unknown parameters, such as a higher temperature than that of cathode wall reported in [90] for the average heavy particles temperature in the orifice (2000 K), sonic condition for the heavy particles at the orifice exit, an electron temperature of 2.3 eV for xenon [35] and a higher value, 3.3 eV, for argon and a ionization fraction of 10%. The value for the

ionization fraction seems reasonable looking at the measurements in the T5 performed with krypton [91] and the numerical results found in the NSTAR cathode (4.1% at the orifice entrance [61]).

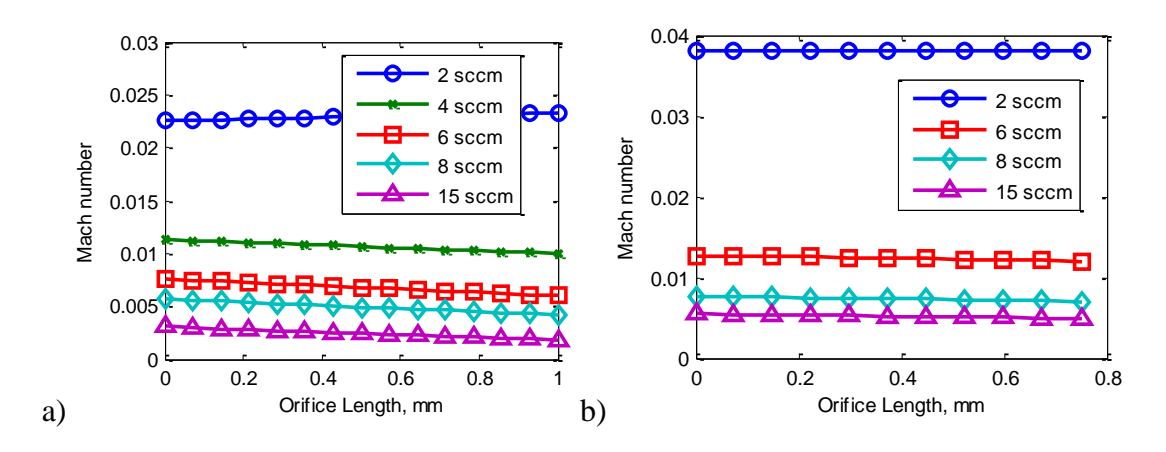


Figure 31 - Mach number in the orifice of a a) T5 at 3.2 A with Argon and b) NSTAR at 8.1 A with Xenon

The electron Mach number along the orifice is shown in Figure 31: its change along the orifice length is modest as shown already by Mikellides [65], hence it is reasonable to fix its value at the orifice entrance.

III.3.2. Source Terms

In this paragraph the source terms for the mass, momentum and energy equations W, X and Y will be discussed in detail. They include the main physical processes that characterize the plasma behaviour such as collisions, ionization, the action of the electric field and heat conduction. The source terms for the electrons mass and momentum equation W_e and X_e are not used in the model hence they will not be discussed.

III.3.2.1. For the Mass Equation

Ionization and particles loss to the wall are included in the mass equation source term for ions and neutrals as shown in Figure 32.

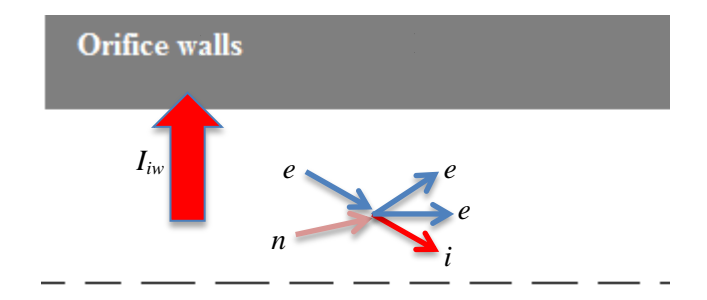


Figure 32 – Source and sink terms for the mass

The mass source for the ions for the ionization process is $m\dot{n}$, where the ion production rate per unit volume \dot{n} is defined as in [60, 61, 77]:

$$\dot{n} = n \, n_n \left\langle \sigma_{ion} u_e \right\rangle \tag{3.9}$$

where $\langle \sigma_{ion} u_e \rangle$ is the collision rate averaged over the Maxwell-Boltzmann distribution, and being σ_{ion} is the ionisation cross section. In the model developed within this research it is not possible to calculate radial components of the variables since the model is one-dimensional. The only way to include particle losses to the wall is by introducing sink and source terms to the equations: the current density of ions flowing to the wall is assumed to be equal to the random thermal flux [57]:

$$J_{iw} = qn\sqrt{\frac{kT_h}{2\pi m_h}} \tag{3.10}$$

Assuming that the ions hitting the walls get neutralized and return as neutrals, the source terms for the ions and neutrals for the mass equation are:

$$W_i = \left(m_h \dot{n} - \frac{m_h}{q} J_{iw} \frac{2}{R_{or}}\right) A \tag{3.11}$$

$$W_n = \left(-m_h \dot{n} + \frac{m_h}{q} J_{iw} \frac{2}{R_{or}}\right) A$$
(3.12)

The source term for the heavy particles is the sum of the source terms for the ions W_i , shown in equation (3.11), and for the neutrals W_n , shown in equation (3.12):

$$W_h = W_i + W_n = 0 (3.13)$$

From equation (3.13) it can be seen that there is no net contribution from the ionization or from the particles flux to the walls to the mass equation for the heavy particles. This is a consequence of treating ions and neutrals as a single fluid, the

heavy particles. Considering the particles flux to the walls, an ion hitting the wall is assumed to get neutralized and return as neutral whereas in the ionisation process a neutral, in the collision with an electron, will become an ion hence remaining a heavy particle.

III.3.2.2. For the Momentum Equation

The action of the electric field, elastic collisions, ionization and losses to the wall characterize the source term for the momentum equation. As discussed for the mass equation source term, when an electron collides with a neutral the latter becomes an ion. As for the momentum equation, ionization is then a sink of momentum $m_h u_h \dot{n}$ for the neutrals; on the other hand the newly formed ions do not provide any net contribution to the momentum of the specie since it is assumed that they will be generated with a random velocity direction. It was discussed that ions flowing to the wall are assumed to be re-emitted as neutrals: this represents a sink of momentum for the ions but not a source for the neutrals since it is also assumed that the reemitted neutrals will have a diffused velocity direction hence producing no net contribution to the species momentum. The electric field E is defined as E=-dV/dxand do not affect the neutrals as they are not charged particles. It is directed from the anode/nozzle towards the emitter inside the HCT and its effect is to slow down the ions flowing in the opposite direction. The result is a sink of momentum qEn for the ions. For what concerns the mean change in momentum R due to elastic collisions between heavy particles and electron, this contribution is given by [92]:

$$\dot{R}_{ie} = -n \, m_e \, v_{ie} \, (u_h - u_e) = -\dot{R}_{ei}
\dot{R}_{ne} = -n \, m_e \, v_{ne} \, (u_h - u_e) = -\dot{R}_{ne}$$
(3.14)

where v is the collision frequency. It should be noted that \dot{R}_{in} =- \dot{R}_{ni} =0 since ions and neutrals (heavy particles) are assumed to have the same velocity. The resulting source terms for the ions and neutrals momentum equation can be expressed respectively as:

$$X_{i} = \left(\dot{R}_{ie} + \dot{R}_{in} + qEn - I_{iw} \frac{m_{h}u_{h}}{q} \frac{2}{R_{or}}\right) A$$
(3.15)

$$X_{n} = (\dot{R}_{ne} + \dot{R}_{ni} - m_{h} u_{h} \dot{n}) A$$
 (3.16)

Following what has already been done for the source terms for mass equation, the sum of the source terms for the ions, shown in equation (3.15), and for the neutrals, shown in equation (3.16), gives the source term for the heavy particles:

$$X_h = X_i + X_n \tag{3.17}$$

III.3.2.3. For the Energy Equation

Elastic collisions, the action of the electric field, ionization, losses to the wall and heat conduction characterize the source terms for the energy equation. In the elastic collision between heavy particles and electrons there is also heat exchange due to the friction, being $u_h \dot{R}$ the frictional contribution, and to the different temperature of the particles, which can be expressed by the thermal energy exchanged per unit time Q [92]:

$$Q_{ie} = -3n \frac{m_e}{m_h} v_{ie} k (T_h - T_e) = -Q_{ei}$$

$$Q_{ne} = -3n \frac{m_e}{m_h} v_{ne} k (T_h - T_h) = -Q_{ne}$$
(3.18)

It should be noted that Q_{in} =- Q_{ni} =0 since ions and neutrals (heavy particles) are assumed to have the same temperature. In the ionization process it is assumed that the old neutral and the newly formed ion will have the same energy hence the associated source and sink terms will be the same in absolute value. The impacting electron will instead use, and hence lose, the energy $qn\varepsilon$ (where ε is the propellant first ionization potential) to ionize the neutral. The action of the electric field on ions and electrons respectively decreases and increases their energy of a quantity qnEu. The assumption made for the source terms for the mass equation, equations (3.11) and (3.12), was that the ions hitting the wall would get neutralized and come back at the wall temperature. As a consequence the energy lost to the wall by the ions is gained by the neutrals. It is assumed instead that the energy that the electrons lose at the wall is equal to the sheath voltage drop since the only electrons that can reach the wall are those with energy at least equal to the voltage drop at the sheath. With the discussion carried out within this paragraph, the source terms for the energy equation can be expressed for the ions, neutrals and electron respectively as:

$$Y_{i} = \left[Q_{ie} + Q_{in} + \dot{R}_{ie} u_{h} + \dot{R}_{in} u_{h} - \frac{\gamma}{\gamma - 1} k \left(T_{h} - T_{w} \right) n \sqrt{\frac{kT_{h}}{2\pi m_{h}}} \frac{2}{R_{or}} + \left(m_{h} \frac{u_{h}^{2}}{2} + \frac{3}{2} k T_{h} \right) \dot{n} + q E n u_{h} - \left(m_{h} \frac{u_{h}^{2}}{2} + \frac{3}{2} k T_{h} \right) \frac{J_{iw}}{q} \frac{2}{R_{or}} \right] A$$
(3.19)

$$Y_{n} = \left[Q_{ne} + Q_{ni} + \dot{R}_{ie} u_{h} + \dot{R}_{in} u_{h} - \frac{\gamma}{\gamma - 1} k \left(T_{h} - T_{w}\right) n_{n} \sqrt{\frac{kT_{h}}{2\pi m_{h}}} \frac{2}{R_{or}} - \left(m_{h} \frac{u_{h}^{2}}{2} + \frac{3}{2} k T_{h}\right) \dot{n} + \left(m_{h} \frac{u_{h}^{2}}{2} + \frac{3}{2} k T_{h}\right) \frac{J_{iw}}{q} \frac{2}{R_{or}}\right] A$$
(3.20)

$$Y_{e} = \left(Q_{ei} + Q_{en} + \dot{R}_{ei}u_{h} + \dot{R}_{en}u_{h} - q\varepsilon\dot{n} - qEnu_{e} - J_{ew}\phi_{sh}\frac{2}{R_{or}}\right)A$$
(3.21)

Where T_w is the temperature of the orifice wall and J_{ew} is the electron current density to the wall, defined as in [35]:

$$J_{ew} = \frac{1}{4} \sqrt{\frac{8kT_e}{\pi m_e}} nq \exp\left[-(\phi_{ax} - \phi_{sh})/T_{eV}\right]$$
 (3.22)

where Φ_{ax} is the plasma potential along the axis. As already done for the mass and energy equations, the sum of the source terms for the ions, shown in equation (3.19), and for the neutrals, shown in equation (3.20), gives the source term for the heavy particles:

$$Y_h = Y_i + Y_n \tag{3.23}$$

III.3.3. Equations

The theoretical model solves a system comprised of two algebraic and four ordinary differential equations. The system of equations is the 2-fluid equation for a plasma flow, modified for the HCT geometry and for the assumptions listed in paragraph III.3.1. The model is first applied to the straight part of the orifice, with the condition of sonic flow applied to the heavy particles at the throat as shown in Figure 33, and then to the diverging part of the domain.

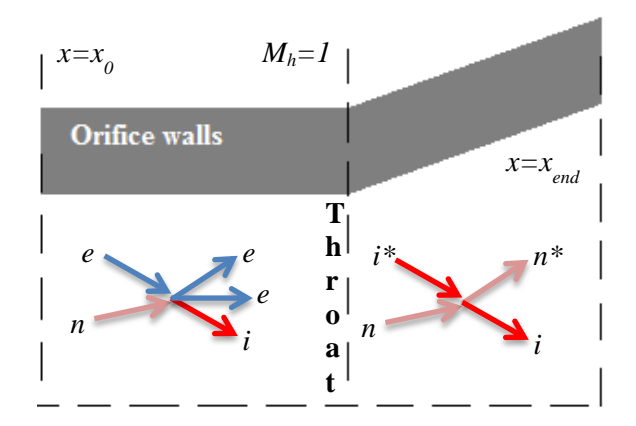


Figure 33 - Computational region division in the orifice and main collision processes

The first equation is derived from the continuity equation for a 2-fluid plasma (conservation of mass for ions and neutrals while electrons are neglected) at steady state:

$$\frac{d}{dx} [A m_h u_h (n + n_n)] = W_i + W_n = 0$$
(3.24)

where n and n_n are respectively the plasma and neutral densities. The term in the square brackets in equation (3.24) is the definition of the mass flow rate \dot{m} . By using equation (3.13) one can obtain the first equation of the model, stating that the mass flow rate is constant in all the cross sections along the orifice:

$$\dot{m} = A m_h u_h (n + n_n) = const \tag{3.25}$$

The second algebraic equation is the definition of the discharge current I_D , defined as the net current flowing through the general section of the orifice:

$$I_D = \int_A \overrightarrow{J} \cdot \overrightarrow{dA} = qn \ A(u_e - u_h) = const$$
 (3.26)

where \overrightarrow{J} is the total current density.

The equation for the heavy particle Mach number M_h , identical to equation (3.8) but applied to the heavy particles, is the first differential equation of the model [24]:

$$\frac{dM_h}{dx} = \frac{M_h (1 + \delta M_h^2)}{(1 + M_h^2) m n u_h A} \left[-\frac{1}{A} \frac{dA}{dx} + \frac{1 + \gamma M_h^2}{2} W_h + \right]$$
(3.27)

$$-\gamma M_{h}^{2} \frac{1+\gamma M_{h}^{2}}{u_{h}} X_{h} + \frac{1+\gamma M_{h}^{2}}{2h_{0h}} Y_{h}$$

The ion and neutral Mach numbers are the same $(M_i=M_n=M_h)$ as a consequence of the assumption made of thermal $(T_i=T_n=T_h)$ and group velocity $(u_i=u_n=u_h)$ equilibrium between ions and neutrals. Since ions and neutrals are monoatomic gases, γ and δ have the same value (respectively 5/3 and 1/3) for the two species.

The plasma potential in the orifice V is obtained by the second differential equation of the model. Equation (3.28) is obtained from the electrons momentum equation by neglecting the inertial term as already described by different authors [60, 61]:

$$\frac{dV}{dx} = \eta J + \frac{1}{qnA} \frac{d}{dx} (p_e A)$$
 (3.28)

where $J = qn(u_e - u_h)$ is the net current density in the axial direction and η is the resistivity in the orifice, defined as [35]:

$$\eta = \frac{m_e (v_{ie} + v_{en})}{q^2 n} \tag{3.29}$$

where ν_{ie} and ν_{en} are respectively the collision frequencies for ions-electrons and electrons-neutrals collisions. The gradient of the pressure term $\frac{d}{dx}(p_eA)$ in equation (3.28) do not need a dedicated boundary condition at the orifice inlet since it can be expressed analytically as:

$$\frac{d}{dx}(p_e A) = \frac{d}{dx}(n k T_e A) = n k T_e \frac{dA}{dx} + n k A \frac{dT_e}{dx} + k T_e A \frac{dn}{dx}$$
(3.30)

The term dA/dx is in fact obtained from the knowledge of the geometry whereas the terms dT_e/dx and dn/dx can be expressed analytically starting from the momentum and energy equations for the electrons.

The third and fourth differential equations are the standard energy equation for a fluid [24] written for the heavy particles and for the electrons. The former is obtained by the sum of the energy equations for ions and neutrals.

$$\frac{d}{dx}(h_{0e}m_enu_eA) = Y_e \tag{3.31}$$

$$\frac{d}{dx}\left[h_{0h}m_h\left(n+n_n\right)u_hA\right] = Y_h \tag{3.32}$$

where Y_h , and Y_e are the source terms of the energy equation respectively for heavy particles and electrons and h_{0h} and h_{0e} are respectively the total enthalpy of the heavy particles and the electrons expressed as:

$$h_{0h} = \frac{\gamma}{\gamma - 1} \frac{kT_h}{m_h} + \frac{u_h^2}{2} \tag{3.33}$$

$$h_{0e} = \frac{\gamma}{\gamma - 1} \frac{kT_e}{m_e} + \frac{u_e^2}{2} \tag{3.34}$$

III.3.4. Boundary Conditions

This 1D model consists in both algebraic equations (3.25)-(3.26) and differential equations (3.27), (3.28), (3.31) and (3.32), with the assumption that the electron Mach number is constant along the orifice. The model solves a boundary value problem (BVP) in the straight part of orifice with boundary conditions at the inlet and outlet whereas in the diverging part of the orifice, the second part of the domain, all the variables needed are given at the inlet and taken from the outputs of the first domain. The boundary conditions at the inlet of the straight part of the orifice are obtained using the values of T_h and Φ_{cat} from the 0D model of the insert discussed in paragraph III.2, the assumption M_e =const and from the solution of a system comprising of equations (3.25), (3.26) and (3.35). The gas accelerates inside the straight part of the orifice reaching the sonic condition at the throat, the downstream end of the first domain, where the sonic condition for heavy particles is in fact imposed. The gas will experience a further acceleration in the diverging part of the orifice and in the nozzle.

$$\begin{cases}
\left(\frac{D_{ins}/2}{B_{01}}\right)^{2} n_{n} \sigma_{ion} \sqrt{\frac{8kT_{e}}{\pi m_{e}}} - \frac{q}{m_{h}} \frac{T_{hV} + T_{eV}}{\sigma_{cx} n_{n}} \sqrt{\frac{m_{h}}{kT_{h}}} = 0 \\
(n + n_{n})kT_{h} = \sqrt{\frac{0.78 \dot{m}_{sccm} \xi T_{r} L_{st}}{D_{st}^{4}}}
\end{cases}$$
(3.35)

The system in (3.35) is comprised of an equation for the electrons temperature, also used in the model for the insert [60], and an equation for the pressure of the heavy

particle obtained by assuming a Poiseuille flow in the orifice [93]. In (3.35) D_{st} and L_{st} are respectively the diameter and length of the straight part of the orifice expressed in cm, D_{ins} is the cathode diameter, B_{01} is the first zero of the zero-order Bessel function, \dot{m}_{SCCM} is the total mass flow rate in sccm, T_{eV} and T_{hV} are expressed in eV, ζ is the viscosity in poises and T_r is defined as [93] $T_r = T_h(K)/289.7$.

III.3.5. Mesh and Solution

A finite difference code based on an implicit Runge-Kutta scheme developed at MatlabTM, the bvp4c solver [94], is used to solve the BVP in the first part of the domain. In the divergent part, the second part of the domain, a fourth order Runge Kutta method is used to solve the model. The values of M_h , h_{0h} , h_{0e} and V at the various axial locations can be found from the solution of the model and from their values, together with the solution of an algebraic system comprised by equations (3.25) and (3.26), the definition of the heavy particles and electrons Mach number and the definition of the total enthalpy of both the heavy particles and the electrons, it is possible to find the values of the variables n, n_n , u_h , u_e , T_h and T_{eV} .

III.4. Model for the Anode/Nozzle Region

In the anode/nozzle the flow is assumed to experience a gasdynamic expansion. The model used in this region is the classical adiabatic expansion in a supersonic nozzle, which is briefly discussed within this paragraph. Neglecting the heat exchange between the flow and the walls, the flow can be assumed isentropic and isenthalpic [24]. From the knowledge of the static temperature of the propellant at the orifice exit T_{ex} , the stagnation temperature of the propellant T_0 can be easily found as [24]:

$$T_0 = T_{ex} \left(1 + \delta M_{ex}^2 \right) \tag{3.36}$$

The stagnation pressure of the propellant p_0 is [24]:

$$p_0 = p_{ex} \left(1 + \delta M_{ex}^2 \right)^{\frac{1}{\gamma - 1}}$$
 (3.37)

Then the static temperature of the propellant T_x at a distance x from the orifice exit can be found [24]:

$$T_{x} = \frac{T_{0}}{\left(1 + \delta \cdot M_{x}^{2}\right)} \tag{3.38}$$

where is the Mach number M_x at a distance x from the orifice exit calculated through the area law [24]:

$$\frac{A}{A_{or}} = \frac{1}{M_x^2} \left(\frac{1 + \delta M_x^2}{\frac{\gamma + 1}{2}} \right)^{\frac{\gamma + 1}{2(\gamma - 1)}}$$
(3.39)

hence the velocity of the propellant u_x at a distance x from the orifice is [24]:

$$u_x = M_x \sqrt{\gamma T_x k/m} \tag{3.40}$$

and the static pressure of the propellant p_x at a distance x from the orifice [24]:

$$p_x = p_0 \left(\frac{T_0}{T_x}\right)^{-\frac{\gamma}{\gamma - 1}} \tag{3.41}$$

III.5. Where the Thrust is Calculated

Inside the model developed, particular attention is paid to the Knudsen number along both the orifice and the nozzle in order to understand up to which section of the HCT the flow is influenced by the geometry of the thruster (either orifice or external nozzle) and hence at which point the thrust has to be calculated. In particular the model is based on the assumption that the flow is in continuous conditions hence its validity ceases when moving into free molecular flow regime. The model self consistently calculates the Knudsen number along the HCT orifice and nozzle and stops the integration if the propellant flow passes into the free molecular regime. It is then assumed that once the propellant reaches the free molecular flow regime no further conversion of static enthalpy into direct kinetic energy will take place in the nozzle hence from that point on the nozzle will become "useless". The thrust is then calculated ideally cutting the nozzle at the section in which the Knudsen number reaches the value of 1, hence when the flow reaches the free molecular regime.

The Knudsen number, that is the ratio of the gas mean-free path (λ) to the characteristic dimension of the body (L) enclosing the gas flow, is calculated to understand if the variation in the geometry (in either the orifice or the nozzle) plays an actual role in the expansion of the gas. It is useful to briefly note that a gas can be categorized into three categories:

- Viscous flow or continuum regime $Kn = \lambda/L_{kn} < 0.01$;
- Transition regime 0.01 < Kn < 1;
- Molecular flow or rarefied regime Kn > 1.

In the case of the HCT the mean free path for particle collisions can be calculated as described in [95]:

$$\lambda_x = \frac{1}{\sigma_{ce} n} \tag{3.42}$$

being σ_{ce} the charge exchange cross section scattering, 100 Å² for xenon [77]. The characteristic dimension of the geometry is calculated as the minimum between the radius of the orifice and the characteristic length of the variation of the cross sectional area:

$$L_{Kn} = \min\left(R, \frac{A_x}{dA/dx}\right) \tag{3.43}$$

with dA/dx being the derivative of the function of the orifice or nozzle cross sectional area. It should be noted that even if a transition regime exists between the continuum and the free-molecular flow ones, the assumption made of calculating the thrust at Kn=1 is the same made by other authors in what is called sudden freeze models [96]. In these simplified models the flow is assumed continuum up to a certain section of the nozzle, beyond which the transition to the free molecular regime occurs abruptly.

III.6. Trends of the Plasma Parameters

The model has been applied to the NSTAR cathode at TH8 and TH15 throttle levels, shown in Table 6, and to the T5 HC. The results are shown in terms of the evolution of the plasma and neutral densities, plasma potential and electron temperature in the orifice.

Table 6 – NSTAR geometry and throttle level [35, 97]

Variable		Value	
		TH8	TH15
D_{ins}	Insert Cathode Diameter	2.80 mm	
D_{st}	Orifice Diameter (straight part)	1 mm	
L_{st}	Orifice Length (straight part)	0.75 mm	
I_D	Discharge Current	8.2 A	13.1 A
m	Mass Flow Rate	2.47 sccm	3.7 sccm

It should be noted that both the T5 and NSTAR HCs were in the keeper configuration and had a fully straight orifice, hence the results will be shown in this part only, as sketched in Figure 34.

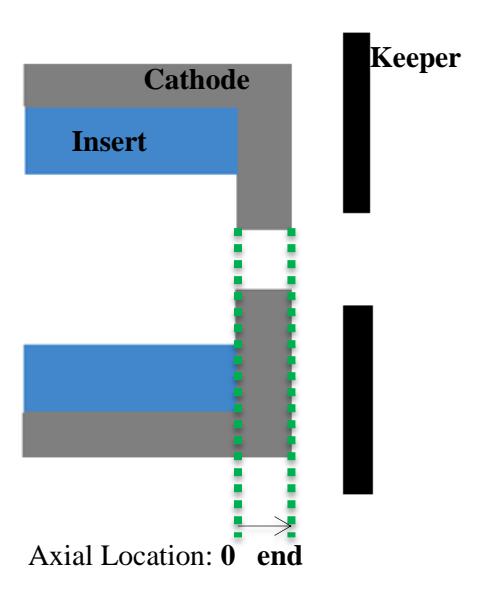


Figure 34 – Geometry of the T5 and NSTAR cathodes

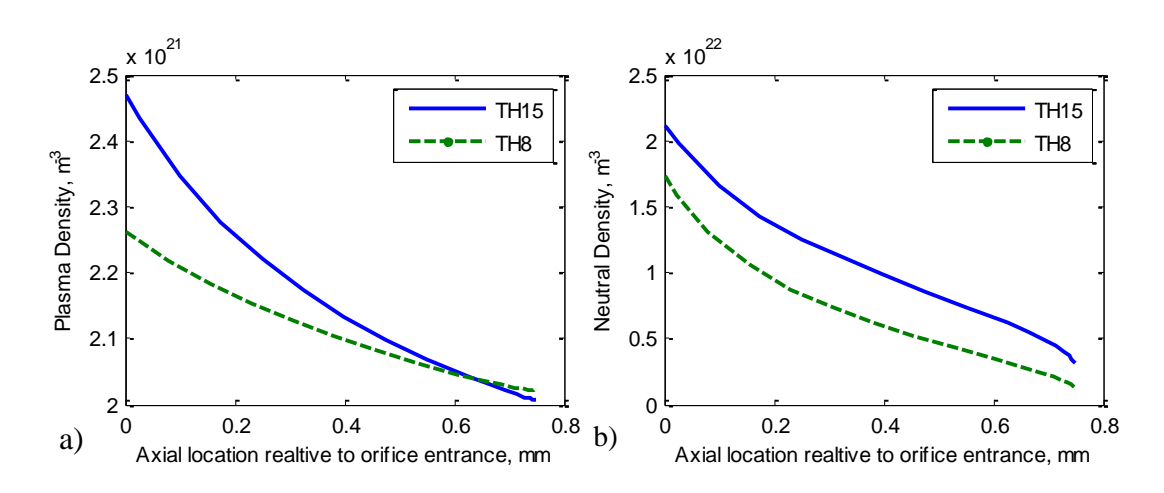


Figure 35 – a) Plasma and b) neutral density profiles in the orifice of the NSTAR cathode at TH8 and TH15 computed with the model

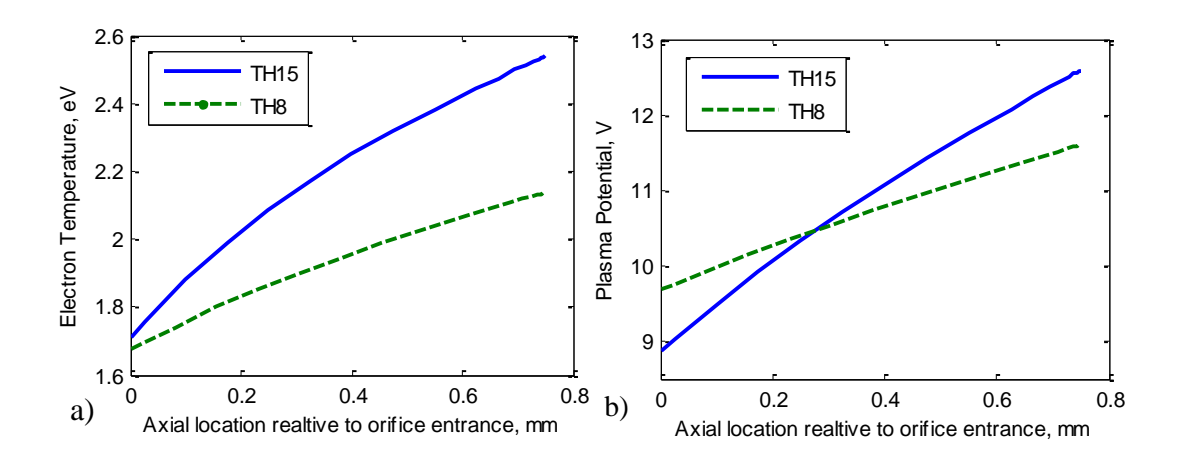


Figure 36 - a) Electron temperature and b) plasma potential profile in the orifice of the NSTAR cathode at TH8 and TH15 computed with the model

Figure 35 and Figure 36 show the computed evolution of the parameters in the orifice of the NSTAR cathode at TH8 and TH15. A first comparison can be made between the measured voltage drop in the orifice, 2 V at TH8 and 4 V at TH15 [35, 97] for the NSTAR, and the value computed by the model, 1.93 V for the TH8 case and 3.85 V for the TH15 case.

In [35, 97] graphs with measurements showing the trend of T_e and n along the whole cathode are reported but retrieving those trends for the orifice region was too difficult and subject to errors since the scale and the size of the graphs was too small, hence they are not reported here for the comparison. On the other hand, the evolution of the parameters in Figure 35 to Figure 36 present the same qualitative trend already derived numerically by other authors in [62]. The neutral density is about an order of magnitude greater than the plasma density, and they both monotonically decrease along the orifice. The electron temperature increases along the orifice and so does the plasma potential.

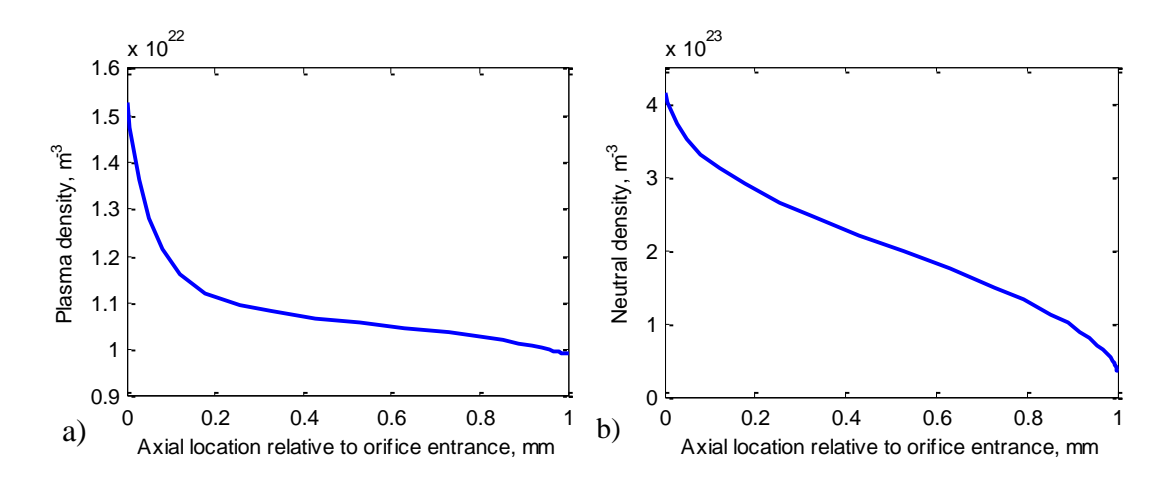


Figure 37 - a) Plasma and b) neutral density profile in the orifice of the T5 HC at 3.2 A and 2.7 sccm

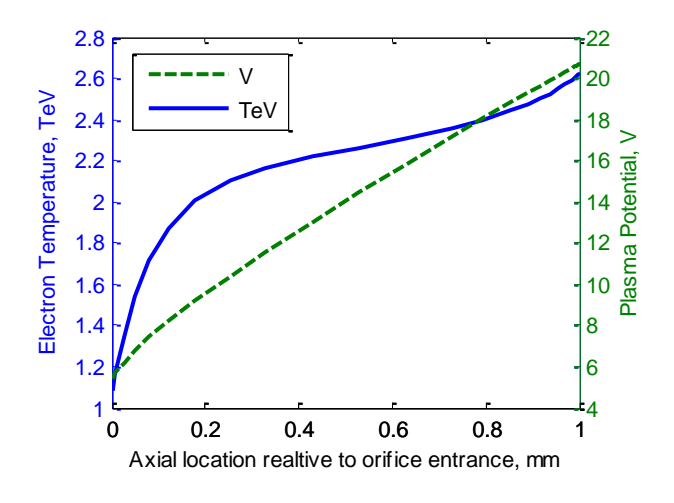


Figure 38 - Plasma potential profile in the orifice of the T5 HC at 3.2 A and 2.7 sccm

In the case of the T5 HC the computed values of the plasma and neutral densities are about one order of magnitude greater than those computed for the NSTAR. These differences lie in the fact that the orifice of the T5 HC is longer than that of the NSTAR cathode (1 mm and 0.75 mm respectively) and much narrower (0.2 mm and 1 mm [97] in diameter respectively): this results in a higher value of the internal pressure that produces higher plasma densities. The shape of the T5 orifice also leads to higher electrical resistance as shown by the large voltage drop computed in the orifice, about 15 V, compared to that of the NSTAR, about 2 V at TH8 and 4 V at TH15 [35, 97].

III.7. Model Sensitivity

In this paragraph the trends of the discharge parameters, computed during the optimisation study, will be shown. Also the sensitivity of the model to small inputs change will be shown. A "baseline" configuration was chosen and then the simulation over a range of discharge current was performed letting one variable (geometrical or mass flow rate) at a time to vary. The baseline configuration was assumed with the characteristics reported in Table 7:

Table 7 – Baseline dimensions of the HCT to show the trends

Variable		Value
	Insert Cathode	
D_{ins}	Diameter	1 mm
	Orifice diameter	
D_{st}	(straight part)	0.6 mm
$L_{st}+L_{div}$	Total orifice Length	2.5 mm
	Orifice divergent	
$L_{div}/(L_{st}+L_{div})$	total length ratio	40%
	Orifice divergence	
$artheta_{or}$	angle	45 degrees

The first parameter which was let to vary was the diameter of the straight part of the orifice D_{st} . The results are shown in Figure 39-a in terms of thrust, in Figure 39-b in terms of specific impulse, in Figure 40-a in terms of discharge voltage and in Figure 40-b in terms of discharge power.

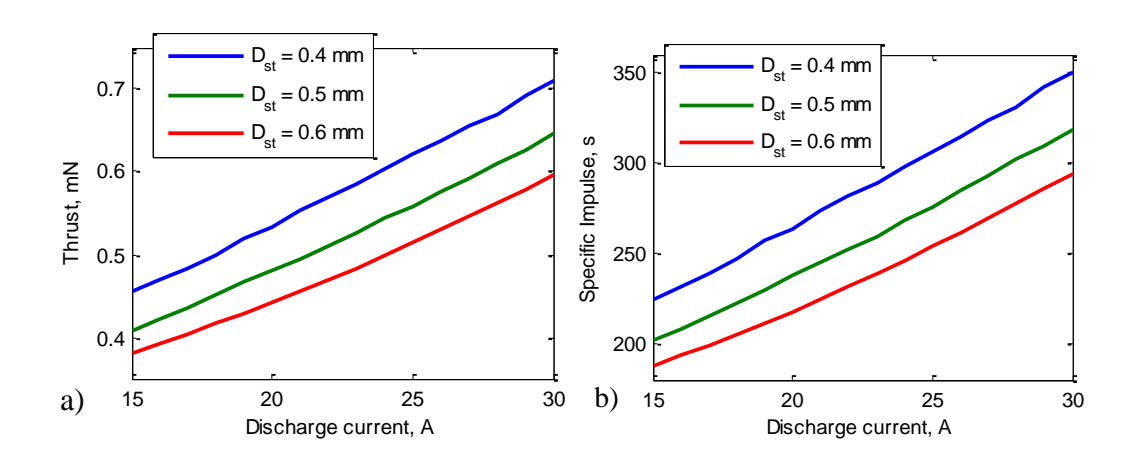


Figure 39 – Trends of a) Thrust and b) Specific impulse varying D_{st}

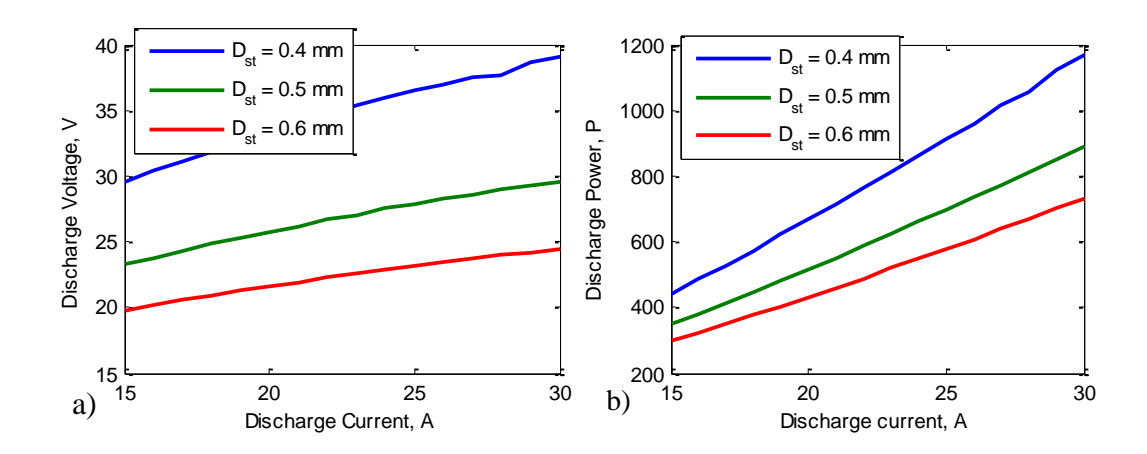


Figure 40 – Trends of a) Discharge Voltage and b) Discharge Power varying D_{st}

All the discharge parameters plotted (thrust, *Isp*, discharge voltage and power) increase with the discharge current and by decreasing the orifice diameter. These were the expected behaviours, except for the discharge voltage (and power) which was expected to decrease if the discharge current would increase. The discharge voltage is a combination of the internal potentials (plasma potential and sheath voltage) and this behaviour in the simulations may be due to the fact that the model does not calculate the voltage drops in the orifice sheath and in the anode sheath, which may be significant. Hence, this can be assumed as a worst case assumption of the discharge voltage.

The second parameter for which a variance was allowed was the length of the straight part of the orifice L_{st} . The results are shown in Figure 41-a in terms of thrust, in Figure 41-b in terms of specific impulse, in Figure 42-a in terms of discharge voltage and in Figure 42-b in terms of discharge power.

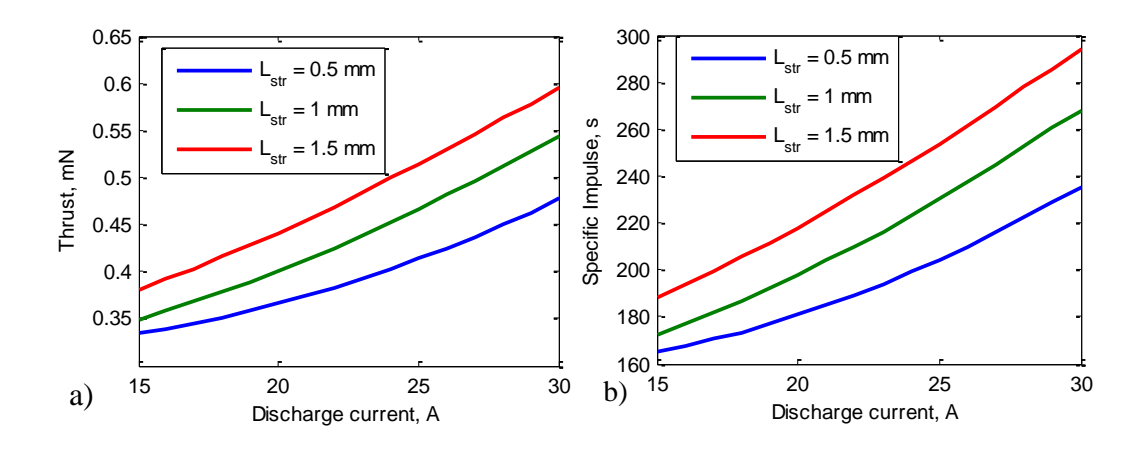


Figure 41 – Trends of a) Thrust and b) Specific impulse varying L_{st}

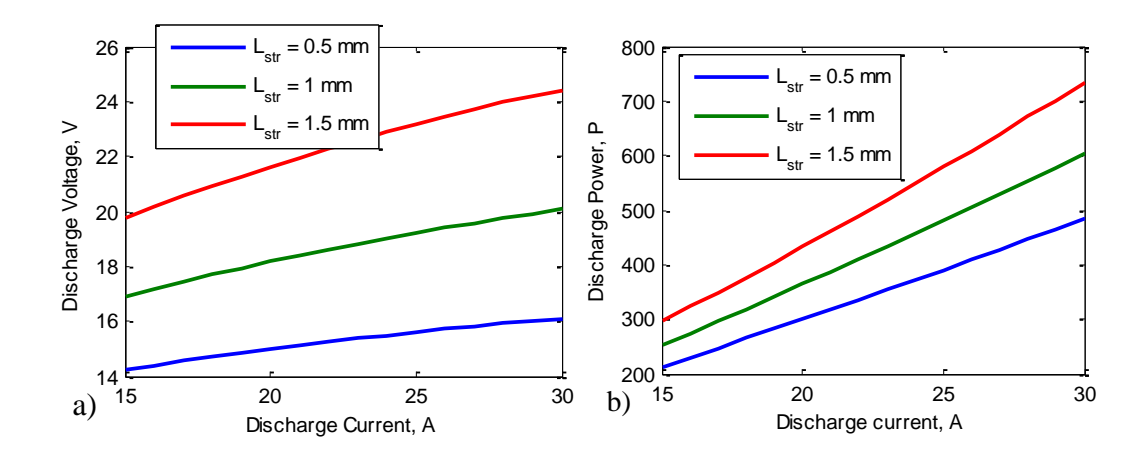


Figure 42 – Trends of a) Discharge Voltage and b) Discharge Power varying L_{st}

The thrust, specific impulse, discharge voltage and discharge power increase with the length of the straight part. This is the behaviour expected since with a longer orifice the gas can be heated more leading to a higher thrust level while the resistance of the orifice becomes higher adding a straight piece to the orifice.

The third parameter which was allowed to vary was the length of the diverging part of the orifice L_{div} . The results are shown in Figure 43-a in terms of thrust, in Figure 43-b in terms of specific impulse, in Figure 44-a in terms of discharge voltage and in Figure 44-b in terms of discharge power.

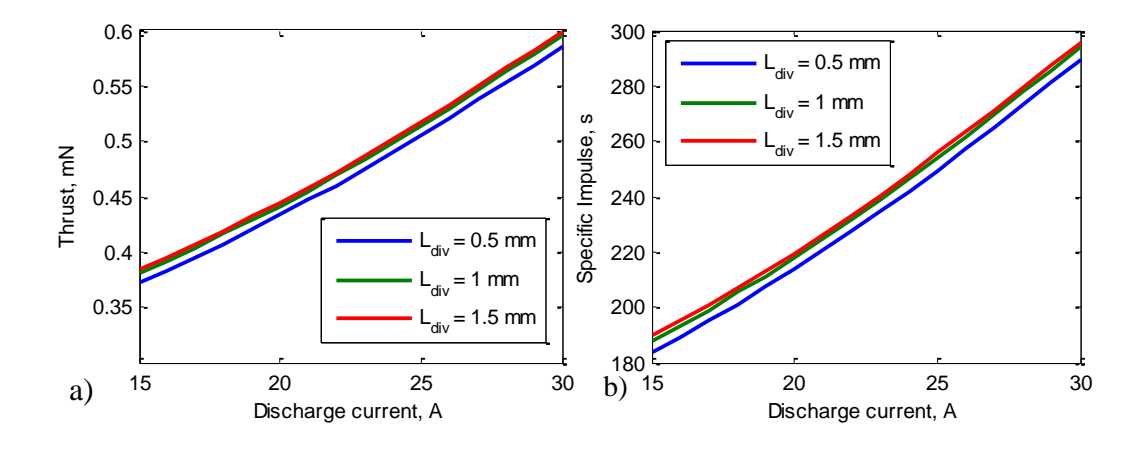


Figure 43 – Trends of a) Thrust and b) Specific impulse varying L_{div}

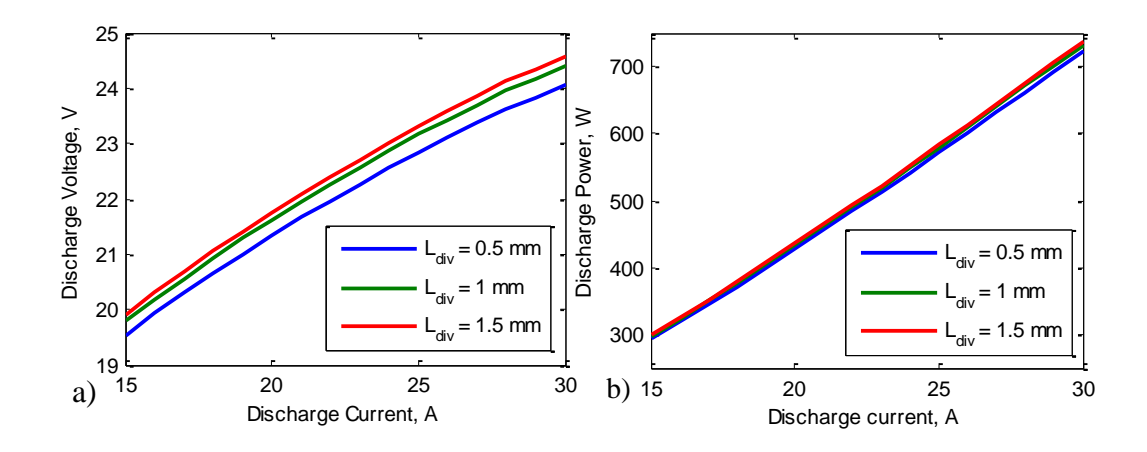


Figure 44 – Trends of a) Discharge Voltage and b) Discharge Power varying L_{div}

Although all the parameters show an increase with the increase of the length of the diverging part of the orifice, the results show that none of them is significantly affected by the variation of length of the diverging part of the orifice.

The fourth parameter which was allowed to vary was the angle of the diverging part of the orifice \mathcal{V}_{div} . The results are shown in Figure 45-a in terms of thrust, in Figure 45-b in terms of specific impulse, in Figure 46-a in terms of discharge voltage and in Figure 46-b in terms of discharge power.

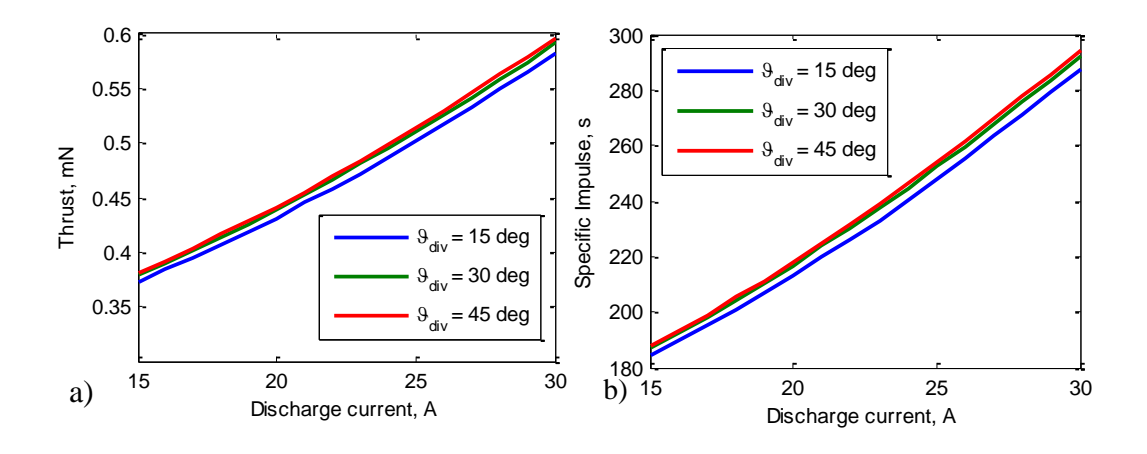


Figure 45 – Trends of a) Thrust and b) Specific impulse varying \mathcal{V}_{div}

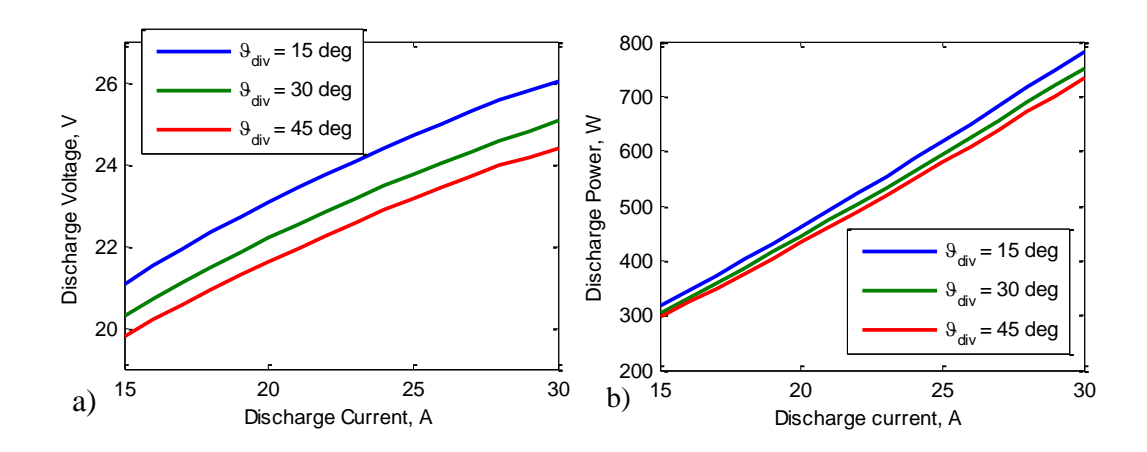


Figure 46 – Trends of a) Discharge Voltage and b) Discharge Power varying \mathcal{Y}_{div}

The results show that the thrust and the specific impulse are not affected significantly by this parameter. The discharge voltage tends to increase with decreasing the angle: this was expected since the smaller is the cross section of the orifice the more resistive it will be.

The last parameter which was allowed to vary was the mass flow rate. The results are shown in Figure 47-a in terms of thrust, in Figure 47-b in terms of specific impulse, in Figure 48-a in terms of discharge voltage and in Figure 48-b in terms of discharge power.

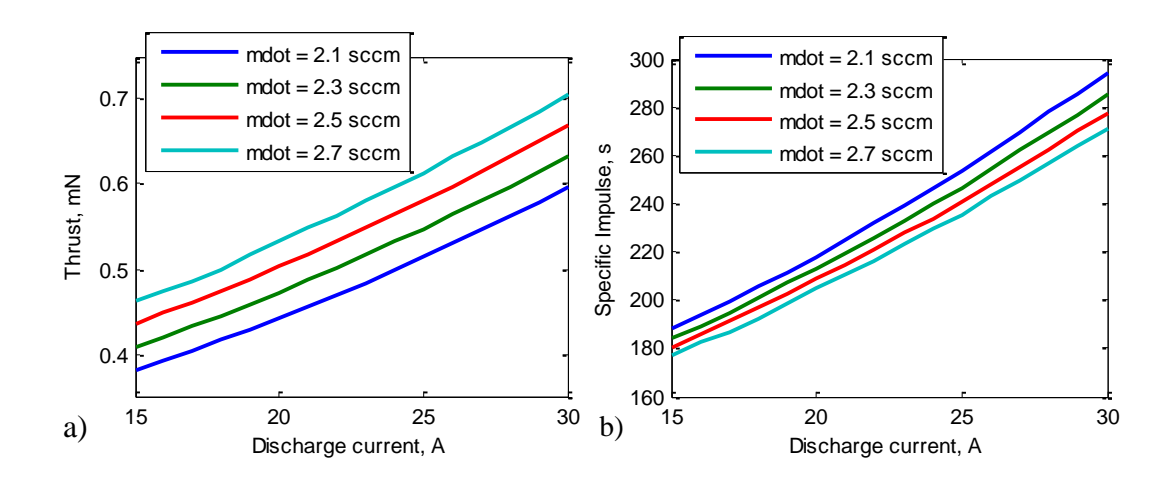


Figure 47 – Trends of a) Thrust and b) Specific impulse varying the mass flow rate

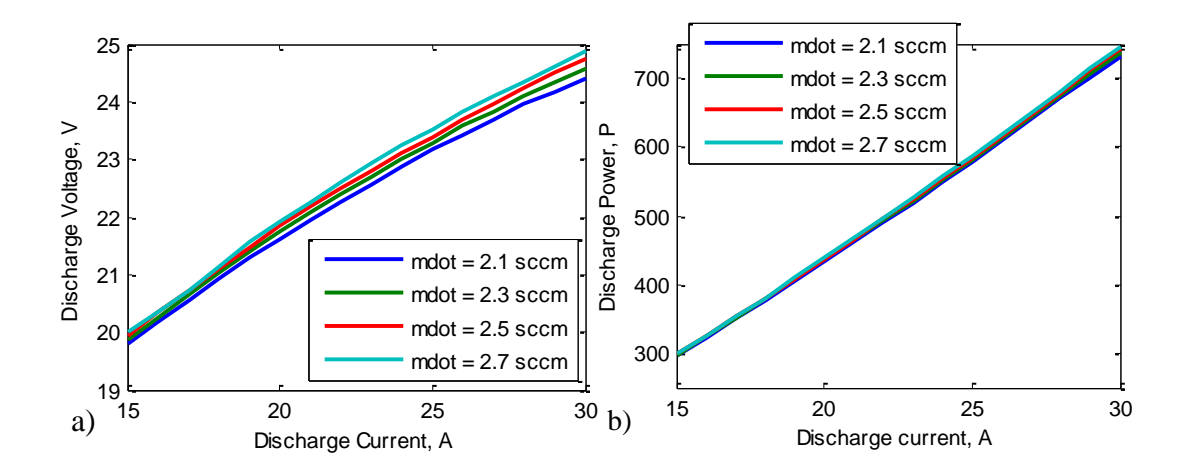


Figure 48 – Trends of a) Discharge Voltage and b) Discharge Power varying the mass flow rate

It should be noted that while the thrust increases with the mass flow rate, the specific impulse decreases if the mass flow rate is increased. The discharge voltage and discharge power are not affected significantly by the change of mass flow rate instead.

III.8. Application of an External Magnetic Field in the Model

In this section the effects that an applied magnetic field might have over the hollow cathode thruster performance will be investigated. These effects will be divided into the influence of the applied field over the electromagnetic thrust (treating the HCT like an MPD) and in the effect that the B field will have over the HC behaviour.

III.8.1. Effect on the Electromagnetic Thrust

The effect that an applied magnetic field will have on the electromagnetic thrust produced by an HCT will be treated as in [69]. The main effects of an applied magnetic field over an MPD-like thruster is the generation of a swirling motion on the plasma column and the conversion of this swirling motion into axial kinetic energy in the magnetic nozzle formed by the diverging magnetic field lines downstream of the thruster.

In [69] the generation of the swirling motion is studied using the magnetic stress tensor and considering the plasma column as a rigid body whereas the effect of the magnetic nozzle will be obtained assuming that the plasma detaches from this nozzle far enough downstream that the magnetic field can be regarded as the one created by a magnetic dipole. The angular swirling velocity ω of the plasma can be then expressed as [69]:

$$\omega = \frac{B_z I_D}{\dot{m}} \left(\ln \frac{R_a}{R_C} + \frac{1}{2} \right) \tag{3.44}$$

Where B_z is the axial applied field in the thruster, I_D the HCT discharge current, R_a the radius at the anode current attachment point and R_C the cathode inner radius. From this the electromagnetic thrust can be calculated as [69]:

$$F_{B} = \frac{1}{2} \left(v_{z0} + \sqrt{v_{z0}^{2} + \omega^{2} R_{a}^{2} - \omega^{8} R_{a}^{8} \frac{R_{m}^{3}}{\alpha^{3} k^{6}}} \cos \theta_{div} \right) \dot{m}$$
 (3.45)

Where R_m is the radius of the coil generating the applied magnetic field and v_{z0} , α are expressed as [69]:

$$v_{z0} = \frac{\mu_0 I^2}{4\pi} \ln \left(\frac{R_a}{R_c}\right) \frac{1}{\dot{m}}$$
 (3.46)

$$\alpha = \left(R_m^{3/2} \frac{B_z}{3} \frac{q}{m_i}\right)^2 \tag{3.47}$$

and where m_i is the ion mass in kg. The values of k and θ_{div} in equation (3.45) represent respectively the ratio between the magnetic field characteristic length and the Larmor radius at the detachment point and the average plasma plume divergence at the exit of the magnetic nozzle.

III.8.2. Effect on the HCT Behaviour

The effect of an applied magnetic field on the HCT behaviour has not been included in the present model and in this paragraph only some zero order estimates of this effect will be provided. The performances of the HCT in different magnetic field configurations will be collected experimentally. The aim is to understand if the applied magnetic field can enhance the performances of the HCT without severely affecting the power requirements and to identify the configuration which gives the best performances.

III.8.3. Analytical Treatment

By applying a magnetic field on the HCT, the electrons will be forced to move in Larmor orbits, experiencing a force F_L called Lorentz force defined as:

$$\overrightarrow{F_L} = \overrightarrow{qu} \times \overrightarrow{B} \tag{3.48}$$

Consider the fluid equation for the momentum, valid for both ions and electrons [35]:

$$mn\left(\vec{u}\cdot\nabla\right)\vec{u} = qn\left(\vec{E} + \vec{u}\times\vec{B}\right) - \nabla\cdot\vec{p} - mn\upsilon\vec{u}$$
(3.49)



Figure 49 – Radial and axial direction in the cathode

Assuming steady state and considering the electrons, referring to Figure 49, in which B acts only in the z direction and following the analytical treatment presented in [35], equation (3.49) can be written for the r and ϑ coordinates as:

$$mn\upsilon u_{r} = -qnE_{r} + qnu_{g}B - kT\frac{\partial n}{\partial r}$$
(3.50)

$$mn\upsilon u_{g} = -qnu_{r}B - \frac{kT}{r}\frac{\partial n}{\partial \theta}$$
(3.51)

Combining equations (3.50) and (3.51) it is possible to find the velocities u_r and $u_{\mathcal{V}}$.

$$u_{r} = \left(-\mu E_{r} - \frac{D}{n}\frac{\partial n}{\partial r} + \frac{\omega}{v}\frac{D}{rn}\frac{\partial n}{\partial \theta}\right)\frac{1}{1 + \omega^{2}/v^{2}}$$
(3.52)

$$u_{\mathcal{G}} = \left(-\frac{\omega^2}{v^2} \frac{E_r}{B} + \frac{\omega}{v} \frac{D}{n} \frac{\partial n}{\partial r} - \frac{D}{nr} \frac{\partial n}{\partial \mathcal{G}}\right) \frac{1}{1 + \omega^2/v^2}$$
(3.53)

where the mobility μ , the diffusion coefficient D and the Larmor frequency ω are defined as [35]:

$$\mu = \frac{q}{m\nu} \tag{3.54}$$

$$D = \frac{kT}{m\upsilon} \tag{3.55}$$

$$\omega = \frac{qB}{m} \tag{3.56}$$

It should be noted that the total collision frequency is defined as in [35]:

$$\upsilon = (\upsilon_{ie} + \upsilon_{en}) \tag{3.57}$$

and that ω/v is the Hall parameter Ω . The analytical treatment in [35] shows how to calculate the velocity of the particles perpendicular to the magnetic field B. It should be noted that unfortunately it is not possible to implement such equations in the developed 1D theoretical model, since to implement equations (3.52) and (3.53) the gradient of the density and the electric filed must be known in more than one dimension (in particular in the radial direction if the applied B field is axial) hence requiring a 2D model. Some zero order estimates of the magnetic field effect will be given in the next paragraphs and from these a recommendation on the shape that the magnetic field should have can be provided.

III.8.3.1. Axial Field

In this paragraph a discussion on the effects of the axial magnetic field is carried out. Since the magnetic field is axial it will have an effect on the particles motion in the radial direction hence this discussion will mainly focus on the effects of the applied field over the current densities flowing from the insert wall to the plasma bulk and vice versa.

III.8.3.1.1. Effect on the current density towards the plasma bulk (thermionic emission)

The applied magnetic field in the cathode will have an effect on the thermionic electrons leaving the insert surface and travelling through the sheath that is formed between the insert wall and the bulk plasma.

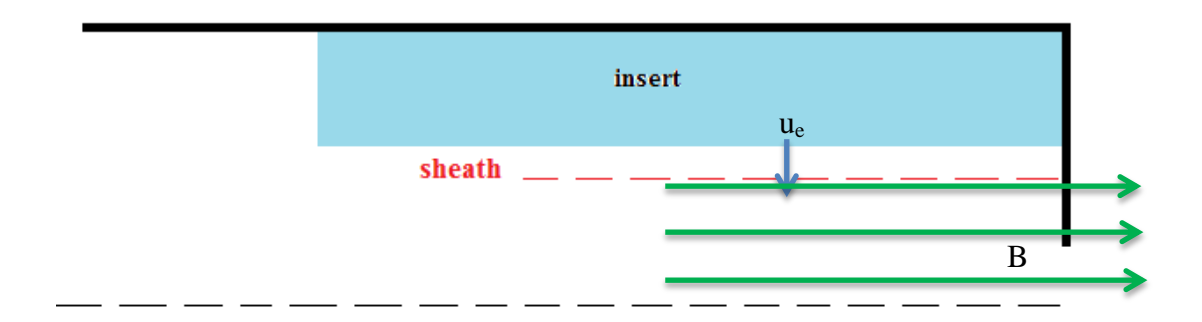


Figure 50 - Magnetic field configuration

If an electron is emitted from the insert in a magnetic field configured like in Figure 50 it will experience the Lorentz force given by equation (3.48). The force acts only in the azimuthal direction (perpendicular to B) hence not affecting the motion in the axial direction, hence the electron will spiral around the magnetic field lines. If the Larmor radius is much smaller than the thickness of the sheath the electrons will be "trapped" in the sheath. The power supply powering the HCT will anyway force the electrons to flow to the plasma since a fixed current (being the power supply generally in current control) has to flow from the cathode to the anode; to overcome the effect of the magnetic field there will be an increase in the discharge voltage and hence in the discharge power needed to run the HCT. For the electrons not to be trapped in the sheath the condition which has to be verified is that the Larmor radius should be much larger than the sheath thickness:

$$R_L >> t_S \tag{3.58}$$

here t_S is the thickness of the sheath, usually few times the Debye length [77], which is defined as [77]:

$$\lambda_D = \sqrt{\frac{\varepsilon_0 k T_e}{n_e q^2}} \tag{3.59}$$

The electron Larmor radius is defined as [77]:

$$R_L = \frac{m_e u_{e\perp}}{aB} \tag{3.60}$$

Combining equations (3.58) to (3.60) it is possible to find a condition on the strength of the magnetic field:

$$B << \frac{m_e u_{e\perp}}{q t_s} \tag{3.61}$$

The 0D model for the insert region gives as results an electron density and temperature of respectively $n=3.5 \times 10^{21}$ m⁻³ and $T_e=1.7$ eV and a neutral density of $n_n=2.5 \times 10^{22}$ m⁻³ for the standard T6 at 24 A and 5 sccm. Using these values a Debye length of 0.16 μ m can be calculated. The upper limit for B, which comes from setting the LHS equal to the RHS in equation (3.61), is then 4245 gauss as shown with the blue circle in Figure 51. This limit has been calculated assuming that t_s is five times the Debye length and that electrons leave the insert surface at the wall temperature [61] hence with a radial velocity equal to their thermal velocity. This velocity is defined as:

$$u_{e,th} = \sqrt{\frac{kT_w}{2\pi m_e}} \tag{3.62}$$

where Tw is the temperature of the insert surface that for these calculations it is assumed to be 1550 K [98].

With these values of n, n_n and T_e in the insert region it is possible to calculate the ratio t_S/R_L for different magnetic field values. These two parameters are reported in Figure 51:

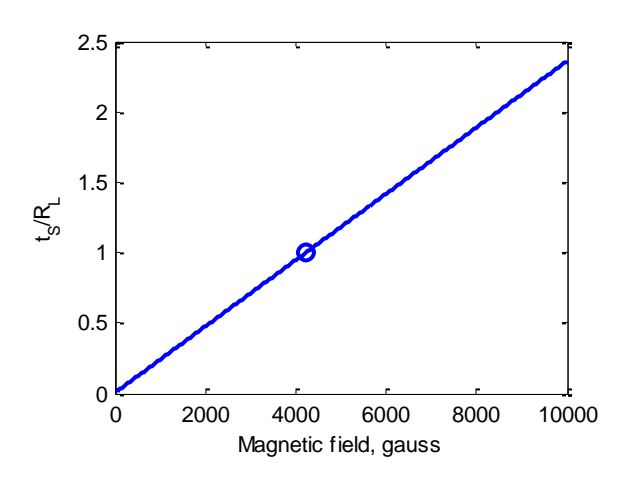


Figure $51 - t_S/R_L$ vs axially magnetic field applied in the insert region

The calculated upper limit at which the magnetic field will "trap" the electrons in the sheath is 4245 gauss, with a safety factor of 1.5; it is possible to confidently say that a lower magnetic field will not have a dramatic effect on the thermionic current.

III.8.3.1.2. Effect on the current density towards the walls – insert region

The magnetic field will have an effect also on the current density flowing to the walls. Since the ions are unmagnetized, only the electrons current density will be treated. The electron current density to the walls will be decreased since the plasma electrons are forced to spiral into Larmor orbits around the magnetic field lines. This will increase the residence time of the electrons in the plasma, hence each electron will experience a higher number of collisions in the plasma. This effect might lead to a higher ionization fraction in the plasma bulk, which in turn can lead to hotter heavy particles possibly enhancing the performances of the thruster.

As discussed in paragraph III.8.3, the electron radial velocity with an axial magnetic field is given by equation (3.52). If no magnetic field is applied the factor $1/(1+\Omega^2)$ is equal to 1 and the equations reduce to the one relative to common diffusion in the absence of magnetic field, hence it is possible to write:

$$u_r^B = u_r^{B=0} \frac{1}{1 + \Omega^2}$$
 (3.63)

In the insert region, using the same mean values discussed in paragraph III.8.3.1.2, it is possible to calculate the coefficient $1/(1+\Omega^2)$ to correct the electron backstreaming current density flowing to the walls.

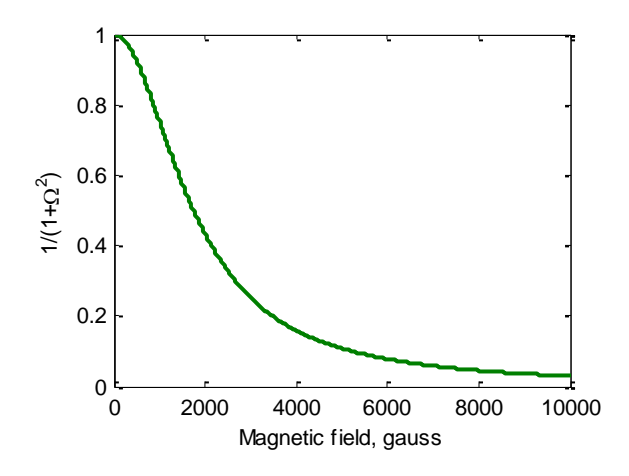


Figure 52 - $1/(1+\Omega^2)$ vs axially magnetic field applied in the insert region

It is possible to use the value of this coefficient to correct the expression of the electrons current density flowing back to the walls, which is defined as:

$$j_{ew} = qnu_r \tag{3.64}$$

where u_r is taken from equation (3.63). The variables in equation (3.64) are in the radial direction, which neither the 0D model for the insert nor the 1D model for the orifice are capable of capturing. To simulate this effect in the 0D model, as an example, a coefficient $1/(1+\Omega^2)$ of 0.5 has been chosen. This coefficient refers to a magnetic field of about 1750 G (Figure 52). Inserting this coefficient in the model to correct the expressions of the electron current density to the walls the effect of the magnetic field over the plasma properties can be estimated. The results with and without the correction factor, obtained with the 0D model for the insert region for the standard T6 at 24 A and 5 sccm, are shown in Table 8:

Table 8 - Variables in the insert region with and without correction

	No correction	With correction
1/(1+Ω^2)	1	0.5
$n, {\rm m}^{-3}$	3.53E+21	4.73E+21
$n_n, {\bf m}^{-3}$	2.51E+22	2.51E+22
T_e , eV	1.70	1.70

According to Table 8, with a correction factor of 0.5 to correct the electron current density to the walls, a lower electron current density is lost to the walls hence producing as expected a higher plasma density n and a higher ionization fraction.

III.8.3.1.3. Effect on the electron current density towards the walls – orifice region

For the orifice region, it is possible to consider the results given by the 1D model in the orifice. An average electron density and temperature of respectively $n=3.98 \times 10^{21}$ m⁻³ and $T_e=2.46$ eV and a neutral density of $n_n=8.34 \times 10^{21}$ m⁻³ have been calculated for a standard T6 at 24 A and 5 sccm. The coefficient $1/(1+\Omega^2)$ in the orifice region is reported in Figure 53:

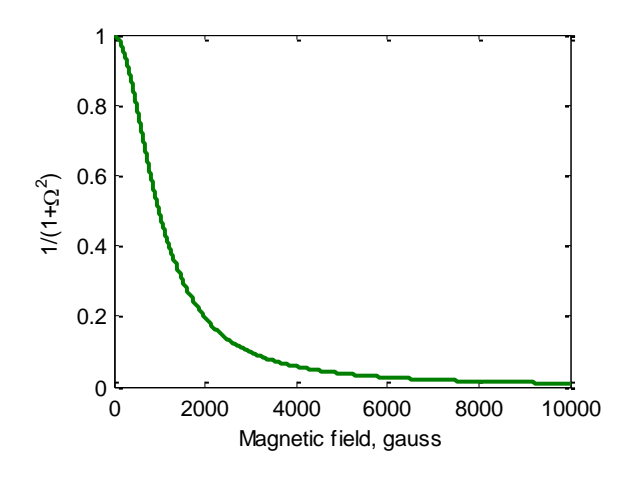


Figure 53 – Variables vs axially magnetic field applied in the orifice region

Considering the same value for the magnetic field (1750 gauss) used in the previous example in paragraph III.8.3.1.2, a coefficient $1/(1+\Omega^2)$ of 0.32 is obtained. It is possible to put this coefficient in the 1D model for the orifice to correct the expressions of the electrons current flowing to the walls. The results with and without the correction are shown in Table 9, ideally considering that the axial magnetic field acts also in the insert region hence a correction factor of 0.5 for the electron current density flowing to the insert wall is taken into account:

Table 9 - Variables in the orifice region with and without correction

	No correction	With correction
1/(1+Ω^2) [insert]	0.5	0.5
$1/(1+\Omega^2)$ [orifice]	1	0.32
n, m^{-3}	3.98E+21	3.91E+21
n_n , m ⁻³	8.34E+21	8.09E+21
T_e , eV	2.46	2.55
I_{ew} , Am ⁻²	2.10E+06	2.52E+06
Thrust, mN	0.898	0.913
Discharge Power, W	349	341

According to Table 9 the magnetic field will not have a dramatic effect on the plasma parameters inside the orifice. The electron current density is slightly increased, whereas the plasma and neutral densities and the electron temperature have not changed significantly. The electron current density to the wall, defined in equation (3.22), has an exponential term $\exp(-\Phi_{ax}/T_{eV})$ which is of the order of 2E-2 (considering Φ_{ax} =10 V [12] and T_{eV} from Table 9) hence the value of the

backstreaming current is already small as well as with no applied magnetic field and it is not dramatically affected by the correction factor of 0.32. It should also be noted that the thrust, calculated without taking into account the effect it may have on the electromagnetic thrust, is slightly increased while the discharge power is instead slightly decreased.

III.8.3.2. Radial Magnetic Field

In this section the effect of a radial magnetic field will be discussed. If an electron is emitted from the insert in a magnetic field configured like in Figure 54 it will experience a force given by Eq (3.50).

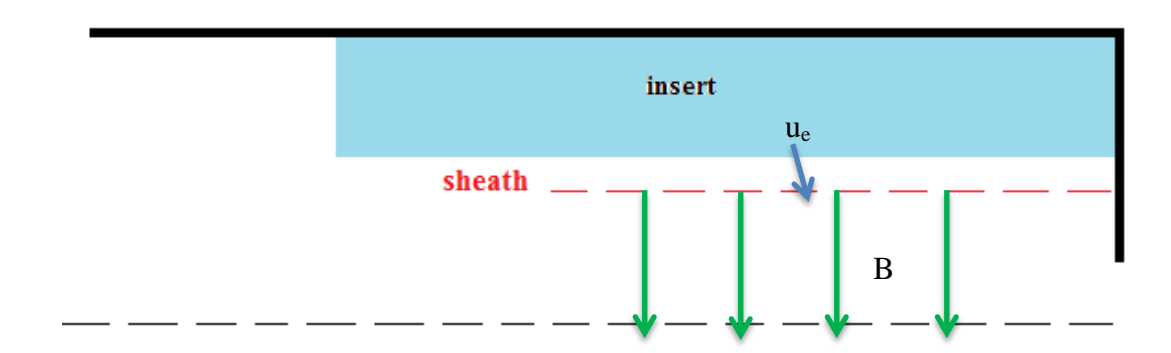


Figure 54 – Magnetic field configuration

The electron velocity will not be purely radial but in general will have also an axial component. The force will act only on the axial component of the electron velocity not affecting the motion in the radial direction hence in this case the thermionic effect is not affected by the magnetic field. For the same reason the electron current density to the walls is not affect by the radial magnetic field since the electron can reach the wall travelling along the magnetic field streamlines.

III.8.4. Ideal Magnetic Field Shape

In this paragraph some guidelines can be given concerning the shape of the magnetic field in the HCT. The shape suggested is shown in Figure 55, with the magnetic field lines following the shape of the current density lines.

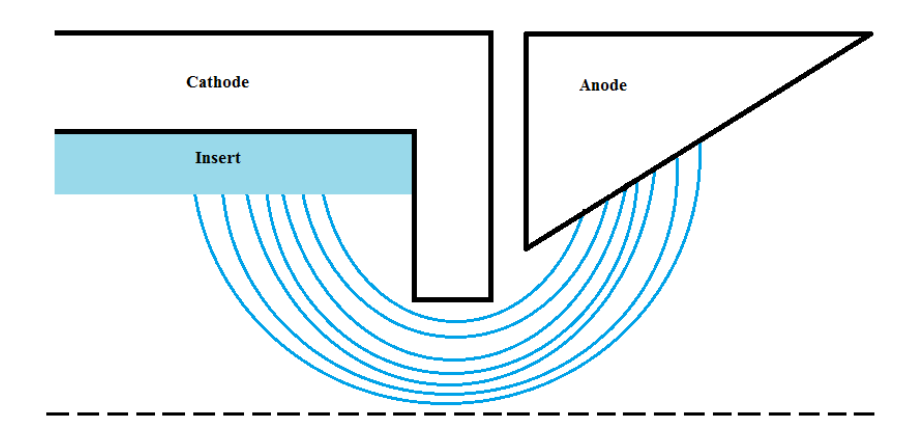


Figure 55 – Suggested shape for the magnetic field

With the discussion in paragraph III.8.3.1 and paragraph III.8.3.2 in mind, it might be beneficial to have the magnetic field lines coming from the insert perpendicular to it. This initial shape will not disturb the radial motion of the particles to and from the insert (thermionic electrons and electron backstreaming current). The shape reported in Figure 55 will also tend to "guide" the electrons to the orifice, decreasing loss to the orifice plate. It might be beneficial to have a constant magnetic field in the orifice, with the field lines in the axial direction to decrease electron current density loss to the walls. The magnetic field lines should then bend outside of the orifice to follow the total current density lines shape towards the anode.

Chapter IV

HCTs Designs, Test Set-Ups and Equipment

It was shown already that HCTs with different geometries have different performances in terms of thrust and specific impulse [6, 12]. A major part of the research was related to the optimization of the geometry of the orifice and the anode to obtain the best possible performances in terms of *Isp*, thrust and power consumption and to commission the manufacture of the HCTs to QinetiQ. This chapter will provide a description of the two HCTs designed within this research as well as a description of the equipment and set-ups used during the experimental tests, including the direct thrust balance developed within this research.

IV.1. The T5 HCTs

The T5 HCTs are based on a QinetiQ's GOCE T5 discharge cathode. The cathode contains a tungsten dispenser (1 mm i.d. x 2.8 mm o.d. x 11 mm) impregnated with a mixture of barium and calcium oxides and aluminates (BaO, CaO and Al₂O₃ in a proportion 4:1:1). The insert is pushed against the orifice tip, which contains an axial orifice 1 mm long and 0.224 mm in diameter. The T5 HCT was initially chosen to start with since:

- 1. It was readily available;
- 2. A similar one was used in [9, 10, 12] and the results could have been compared to those already available in [9, 10, 12] and discussed in chapter II. To do so the orifice was modified from the original design to match the orifice geometry of the STRV1 neutraliser used by Grubisic in [9, 10, 12];
- 3. A first series of directly measured thrust data would have been used for a first validation or verification of the theoretical model.

The T5 was used in two configurations:

- T5K, which is shown in Figure 56. In this configuration the T5 is with its original keeper, which has a 3 mm diameter aperture and it is mounted 3.2 mm downstream the orifice exit;
- T5A, shown in Figure 57. In this configuration the original keeper is removed and replaced by the spacer and the nozzle.



Figure 56 – The T5K HCT

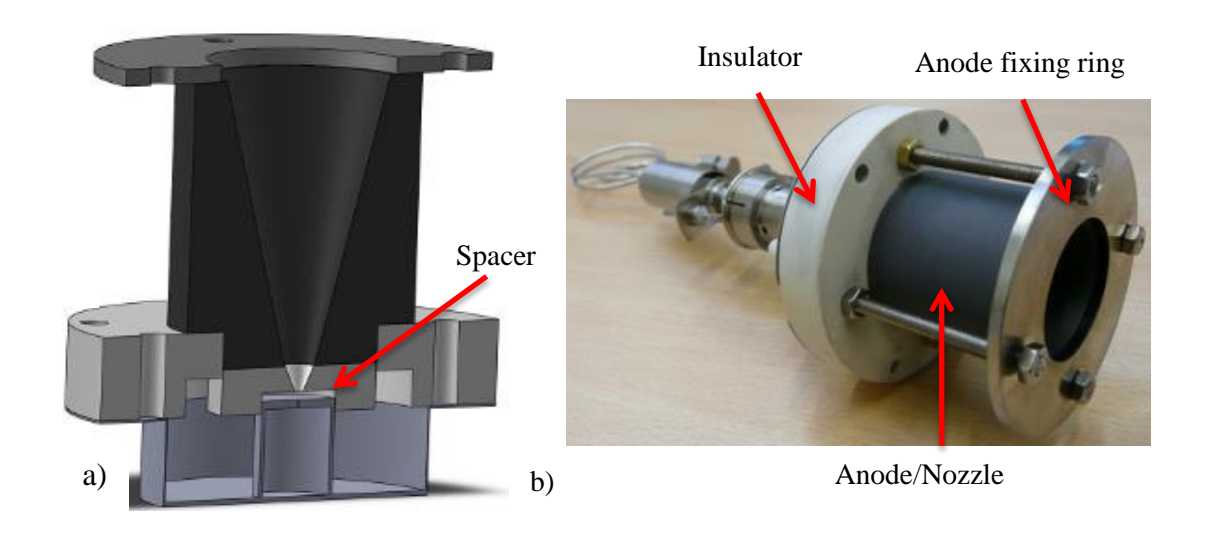


Figure 57 – The T5A HCT

To change the thruster configuration from T5K to T5A the following pieces were designed:

- the anode/cathode insulator, shown in Figure 57. It is made of shapalM and is used to avoid contact/short-circuiting between the anode and the cathode;
- the nozzle shapalM spacer, shown in Figure 57. Its function is to "fill" the gap between the cathode orifice and the nozzle providing a continuous surface between the two electrodes;
- the anode/nozzle, shown in Figure 57. It is made of graphite and placed 4 mm downstream of the cathode tip. It has a semi-angle divergence of 30 degrees, an entrance and exit diameter of respectively 4 and 22.4 mm and a length of 34.31 mm. This particular geometry has been chosen to match the T5CA (Conical Anode) configuration used by Grubisic in his tests at the UoS [9, 10, 12];
- the anode fixing ring, shown in Figure 57. It is a stainless steel ring used to
 mechanically fix the anode to the cathode body. The electrical connections to
 the anode were made connecting the anode cable to this ring using an eyelet
 connector.

IV.2. The optimization of the HCT

The optimized HCT was designed with an optimization process with the use of the theoretical model discussed in chapter III to at least achieve the requirement obtained in chapter I (250 s at 0.6 mN with power consumption less than 500 W). At the time of the optimisation process, the available HCs at QinetiQ (which had to manufacture the optimised HCT) were the T5 and T6 HCs. In order to have the optimised HCTs in the shortest time possible, and since the manufacture of a HC starting from zero would have taken a very long time, it was decided to modify either an unused T5 HC or an unused T6 HC. Hence only the orifice and nozzle geometry of either a T5 or T6 HCTs were the features to be optimized; this optimization process was aimed at finding the best possible performance in terms of *Isp* with some constrains:

- thrust higher than 0.6 mN;
- power consumption less than 500 W;
- temperature of the cathode walls not to exceed maximum working temperature of the materials;

• working point to be in spot mode.

IV.2.1. Flowchart and Boundaries

The geometrical parameters to be optimized are shown in Figure 58, whereas the parameters range of value is shown in Table 10 for the T5 and T6 HCTs.

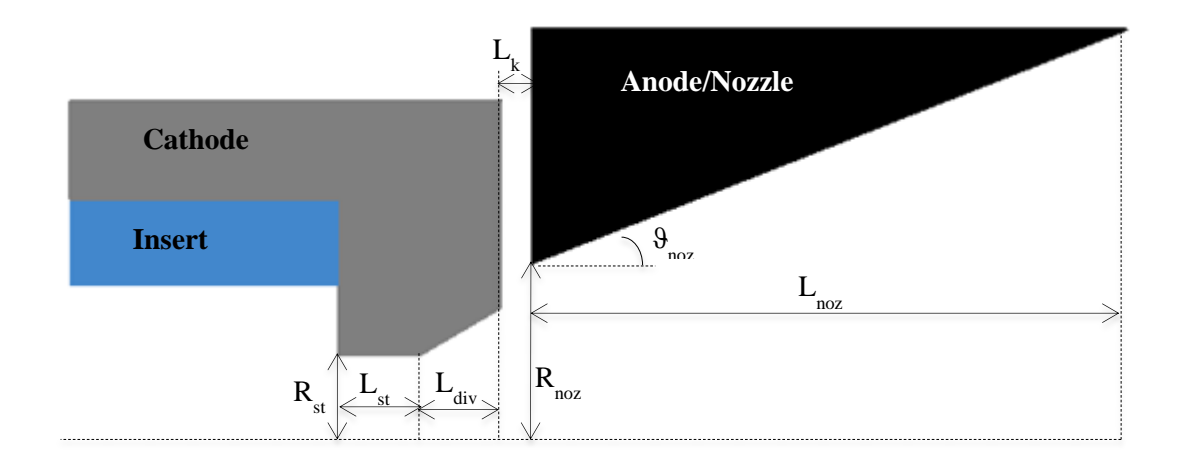


Figure 58 – Dimension to be optimised (insulating spacer not shown)

Table 10 – Range of parameters for the T5 and T6

Variable	T5 HCT		T6 HCT	
v ar lable	Min Range	Max Range	Min Range	Max Range
R_{st}	0.1 mm	0.66 mm	0.2 mm	1.6 mm
$L_{st}+L_{div}$	0.1 mm	4 mm	0.1 mm	8 mm
$L_{div}/(L_{st}+L_{div})$	0	1	0	1
$artheta_{or}$	0 degrees	45 degrees	0 degrees	45 degrees
L_k	0.1 mm	10 mm	0.1 mm	10 mm
R_{noz}	R_{or}	$3R_{or}$	R_{or}	$3R_{or}$
L_{noz}	0.5 mm	50 mm	0.5 mm	50 mm
g_{noz}	0 degrees	45 degrees	0 degrees	45 degrees
I_d	1 A	6 A	5 A	30 A

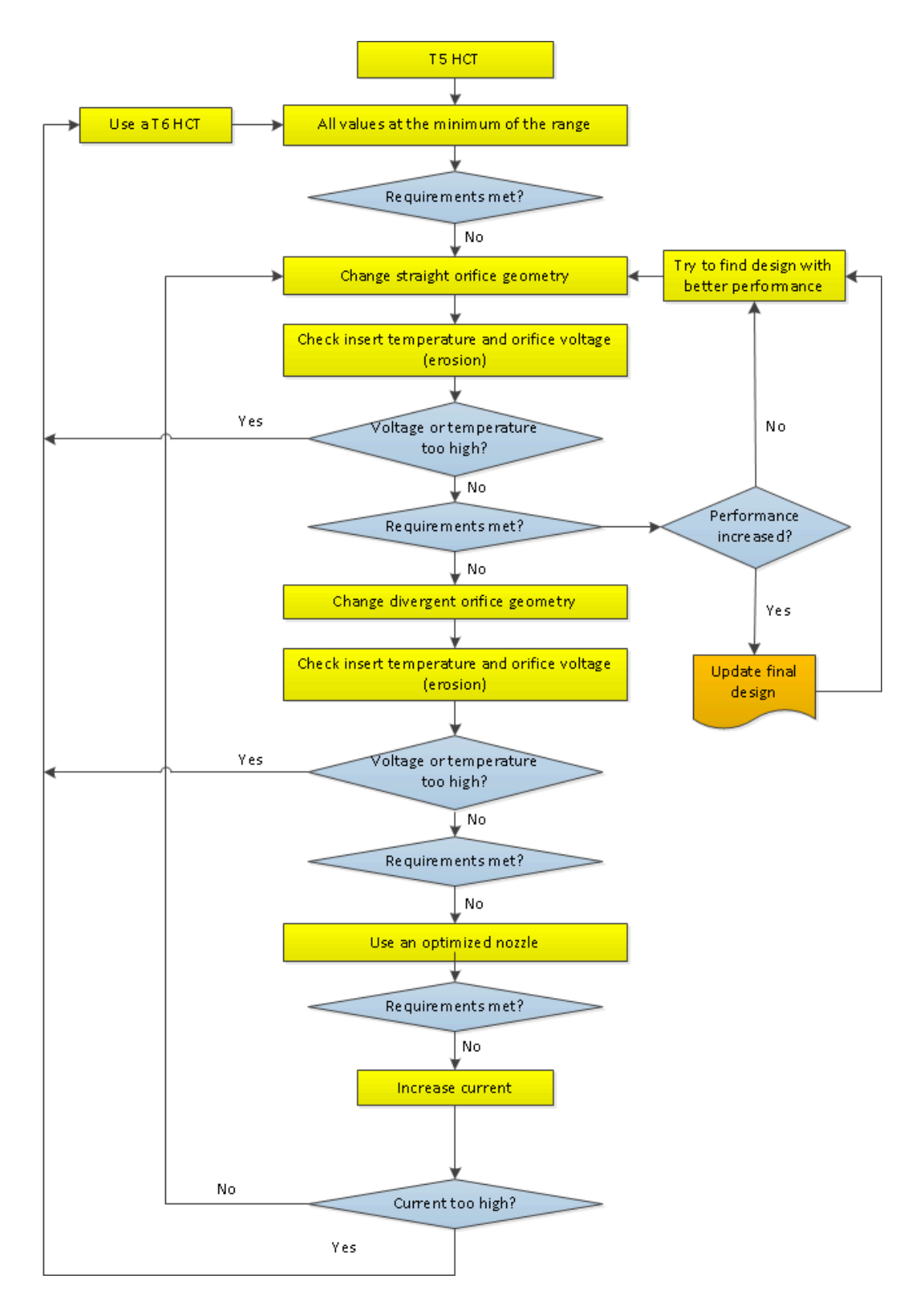


Figure 59 – Flowchart

IV.2.2. The Optimised T6 HCT

As discussed already and shown in the flowchart, the optimisation study investigated the performances that the HCT could achieve over a wide range of geometries and set-points. The best performances predicted by the theoretical model are shown in Table 11:

Table 11 – Best performance predicted by the model

Variable	Value	
I_D	24 A	20 A
Mass flow rate	4.5 sccm	5 sccm
Thrust	1.19 mN	1.21 mN
I_{sp}	277 s	253 s

The HCT showing the performance listed in Table 11 was found to be a T6 based HCT (hence with an insert radius of 1 mm) with an orifice diameter 60% smaller than that of the original T6 HC and the orifice 1.5 times longer. The values of the optimised parameters are listed in Table 12:

Table 12 – Optimized T6 HCT geometry

Variable	Value	Value/Nom_val
R_{ins}	1 mm	100%
R_{st}	0.2 mm	40%
$L_{st}+L_{div}$	2.5 mm	125%
$L_{div}/(L_{st}+L_{div})$	0.4	80%
$artheta_{or}$	45 degrees	100%
L_k	2 mm	-
R_{noz}	3.2 mm	-
L_{noz}	20 mm	-
$artheta_{noz}$	45 degrees	-

A cutaway view of the HCT is shown in Figure 60, where all the different parts needed to convert the HC to a HCT can be seen and which are described.

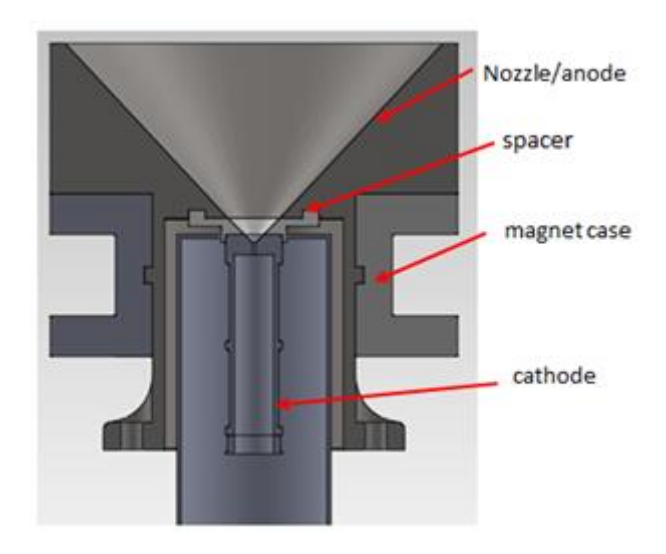


Figure 60 – T6 HCT Cutaway

The nozzle is shown in Figure 61-a. It is made of graphite, machined from a single piece.

The spacer is shown in Figure 61-b and is made of a thermally non-conductive material (Boron Nitride), and is placed between the orifice plate and the cathode to provide electrical insulation and it is shaped to match the cross sections of the orifice exit on one side and the nozzle entrance on the other side.

The magnet case is shown in Figure 61-c. It is made of Macor and it is composed of two pieces hold together by compression of the magnet coil that will be wrapped around it. The magnet wire is a Ceramawire 22AWG Kulgrid HT ceramic coated wire.

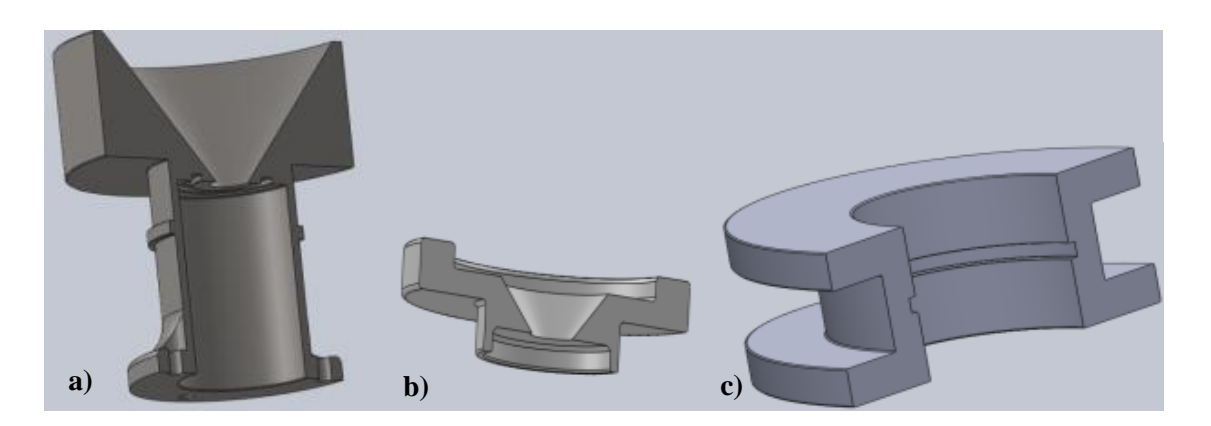


Figure 61 – Pieces manufactured for the T6 HCT.

The fully assembled optimized T6 HCT is shown in Figure 62:



Figure 62 – The T6 HCT

IV.2.3. Magnetic Field Calibration

The coil wrapped around the T6 HCT generates a magnetic field when a current is passed through it. A calibration test was carried out at QinetiQ and the test set-up is shown in Figure 63. The set-up is comprised of a power supply connected to the coil operating in current control, and a three axis magnetic probe positioned at the upstream section of the nozzle. The calibration test consisted in applying the current to the coil with the power supply to generate the magnetic field and measured its axial component.

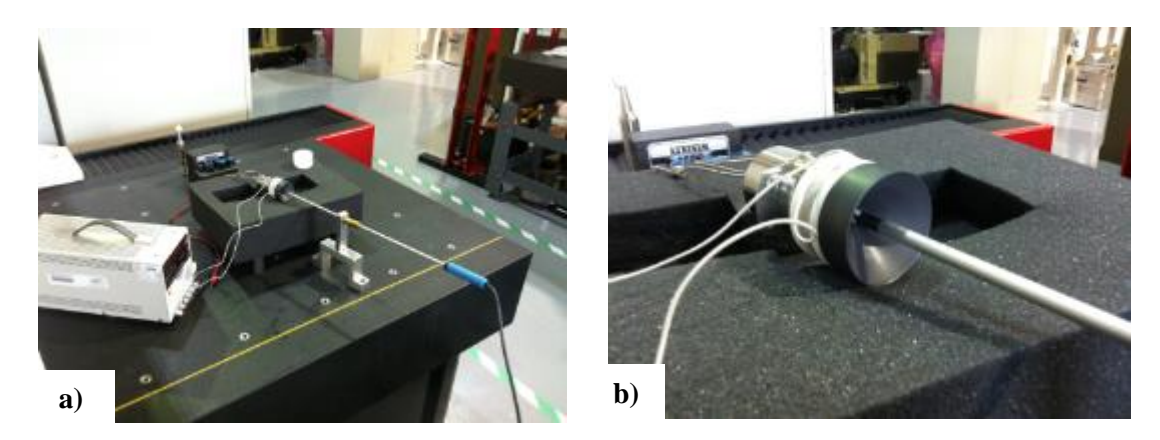


Figure 63 – Test set-up of the calibration test of the magnetic field

The results from the calibration test are shown in Figure 64: the measured axial magnetic field is linear with the applied current.

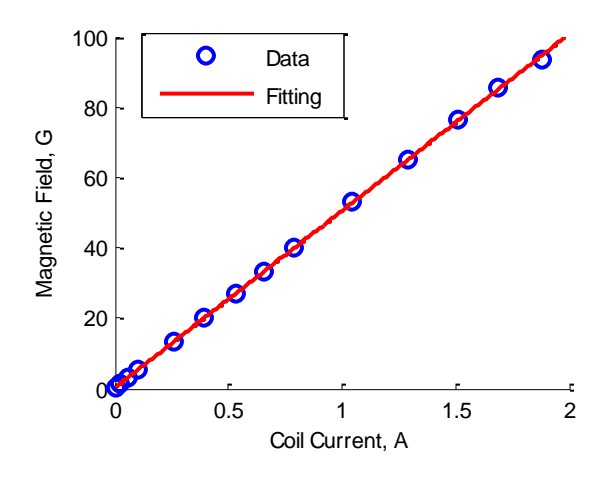


Figure 64 – Results of the calibration of the magnetic field

IV.3. Test Equipment and Set-Up at AER

IV.3.1. Vacuum Rig and diagnostic

The test facility at Aerospazio is the MVTF-1, a vacuum chamber 3 m long and 1.3 m in diameter. The level of vacuum is reached with a Turbomolecular pump (700 l/s air) backed by a Dry Rotary pump and a Cryopump (1500 l/s air) and it is monitored by a vacuum gauge (Leybold Ionivac ITR-90, range $1x10^{-2} - 1x10^{-8}$) placed on top of the chamber approximately 40 cm downstream the exhaust plane of the thruster. The base pressure reached in the chamber was $\sim 5x10^{-7}$ mbar.

IV.3.2. Fluidic Line

The propellant used was Xenon grade 4.9. The propellant feed system is shown in Figure 27 and consists of a breadboard equipped with Digital Mass Flow Controllers and Meters supplying different feed lines. Each feed line is equipped with valves and pressure sensors remotely controlled. An oxygen filter cartridge is installed in the feed line in order to trap the impurities.



Figure 65 – Fluidic lines at AER

IV.3.3. Test equipment

The power supplies needed to operate the thruster are located in a breadboard rack called Test Power Supply (TPS). The TPS consists of an acquisition and control box, a computer and the power supplies. The TPS also provides the control voltages for the flow control units and for the electro-pneumatic valves of the propellant feed system. It also provides data channels for upcoming test purposes and digital input/output lines to perform automatic control of the system.



Figure 66 – The TPS

The full list of the test equipment used at AER is reported in Table 13 and Table 14:

Table 13 - Test equipment with the T5K HCT at AER

Requirement	Name	Output Range
Heater Power Supply	TDK-Lambda GEN 600- 5.5	600V - 5.5A
Discharge Power Supply	TDK Lambda ZUP 36-6	36V - 6A
HV Power Supply	Bertan 205B-01R	1kV - 30mA
To acquire HCT discharge voltage	DPO 3034 4-Channel Oscilloscope	Tektronix
Mass Flow Controller	Celerity 7361C 10 sccm	10 sccm $\pm 0.5\%$ of reading $\pm 0.1\%$ of full scale
Electrical test and PS validation	FLUKE Insulation tester 1507	

Table 14 - Test equipment with the T6 HCT at AER

Requirement	Name	Output Range
Heater Power Supply	TDK-Lambda GEN 600- 5.5	600V - 5.5A
Discharge Power Supply	Glassman LV80-37	80V – 37A
HV Power Supply	FUG MCP 4200-1250	1.25kV - 3A
Coil Power Supply	TDK Lambda ZUP 36-6	36V - 6A
To acquire HCT discharge voltage	DPO 3034 4-Channel Oscilloscope	Tektronix
Mass Flow Controller	Celerity 7361C 10 sccm	10 sccm $\pm 0.5\%$ of reading $\pm 0.1\%$ of full scale
Electrical test and PS validation	FLUKE Insulation tester 1507	

IV.3.4. Electric Interfaces

The set-ups for the T5K and T6 HCTs tests at AER are shown in Figure 67:

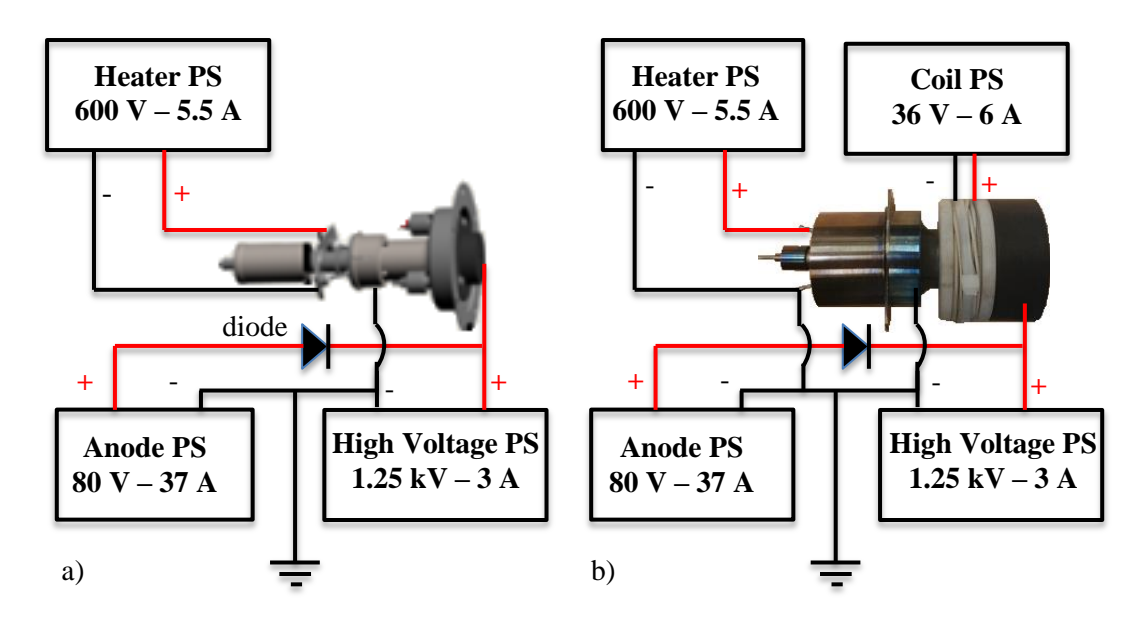


Figure 67 - Electrical test set-up at AER for a) the T5K and b) the T6 HCT

The electrical connections needed are 4, both heater terminals, anode and ground, for the T5 HCT and 5, one heater terminal, anode, ground and both the coil terminals, for the T6 HCT since in both the cases cathode body was connected to the ground. Five electric cables are available in the balance for supplying the installed thruster and they are crimped to a DISTRELEC plug shown in Figure 68.

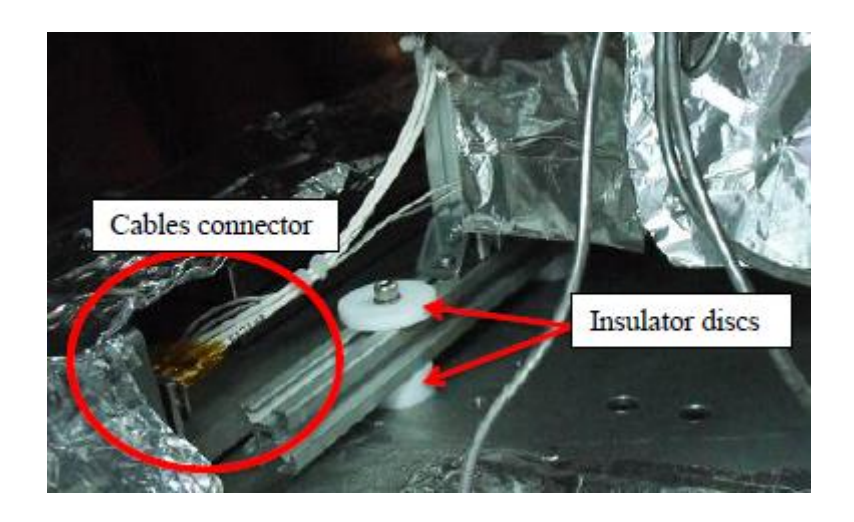


Figure 68 – Electrical connections at AER

The cables used for each thruster is shown in Table 1:

Table 15- Cable used

Cable number	T5K HCT	T6 HCT
1	Anode	Anode
2	Heater	Heater
3	Heater Return	Coil
4	Ground	Coil Return
5		Ground

IV.3.5. Mechanical Interfaces

The HCTs were mounted on the thrust balance as shown in Figure 69. Four M3 studs were used to install each thruster with its mounting flange on the balance to minimize the heat transfer to the balance. The balance was wrapped with MLI and aluminium foils to minimize the radiated heat transfer.

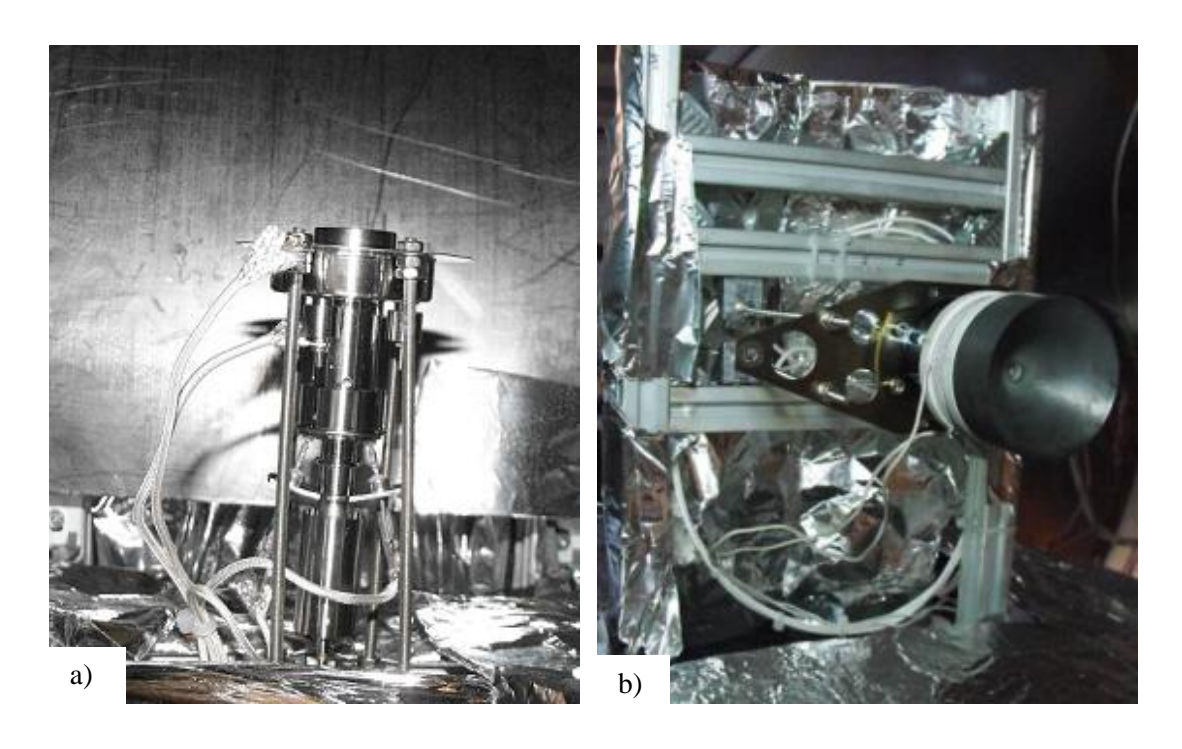


Figure 69 - a) T5K and b) T6 HCTs on the thrust balance at AER

IV.3.6. The Thrust Balance at Aerospazio

The direct thrust balance at Aerospazio was completely designed, commissioned and developed at Aerospazio and it consists of a parallelogram composed of two plates (an upper one and a lower one) connected together by means of four bars and the corresponding hinges. The stiffness of the hinges can be chosen so that thrusters of

different weight and thrust level can be accommodated on the upper plate (the movable one). The lower plate is the fixed part connected to the test facility. Thus, the thrust balance features a spring of a known value. In order to provide better accuracies, the balance works on the principle of the null reading. It means that a sensor performs a continuous monitoring of the reference position of the balance and provides the signal to an actuator (a voice coil) which counteracts the propulsive force of the thruster in order to maintain a zero reading (i.e. zero displacement) of the sensor. In order to damp oscillations an eddy current brake is used. The thruster is mounted on the upper plate. The electrical and propellant feeding is performed through special hinges that maintain a constant stiffness over the time in vacuum conditions. A water-cooled enclosure provides a thermally controlled environment for all in-vacuum sensors and electronic equipment. The thrust balance is continuously cooled down by a dedicated chiller providing a temperature control of $\pm 1^{\circ}$ C. In addition the external surfaces of the balance have been fully enclosed in a MLI protection in order to provide a more stable thermal environment.

The electronic system consists of a PID controller which receives the displacement signals and drives the voice coil supplying the given current. An additional mechanical system allows the calibration of the balance over a set of known masses.

IV.3.6.1. The Working Principle

Being a null reading balance, the thrust is the force produced by the voice coil in order to have a zero reading (i.e. displacement) of the sensor. The force is:

$$F = C_V \sqrt{R_V I_V^2} \tag{4.1}$$

In equation (4.1) I_V and R_V are respectively the current passing through the circuit of the voice coil and the resistance of the circuit itself, whereas C_V is a constant characteristic of the voice coil, given by the manufacturer with an uncertainty of $\pm 10\%$. Equation (4.1) can be rewritten as follows:

$$F = I_V K_V \tag{4.2}$$

where $K_V = C_V \sqrt{R_V}$. It should be noted that R_V is known, being measured at the time of the balance assembling, and constant since the flowing current (tens of nano to milli ampere) does not affect it. Since R_V is a known constant (measured with an

uncertainty <<1%) and I_V is the flowing current given by the power supply (with an uncertainty <<1%), the only uncertainty arising from equation (4.2) is that of the voice coil gain K_V . This uncertainty can be reduced if a calibration process is undertaken: therefore an overall thrust balance calibration gain has been found as explained in the paragraph below.

IV.3.6.2. The Thrust Balance Calibration Gain

The balance calibration gain is determined and verified by means of an in situ calibration system equipped with a series of sample weights corresponding to forces in the range of the expected thrusts. The masses of the calibration weights are shown in Table 16: they were measured using a XP205 MettlerToldedo balance with a resolution of 0.01mg. Each weight has been measured 6 times providing values with standard deviations lower than 0.02%.

Table 16 - Sample weight used for calibration

Sample	Mass, g	δMass, g	Thrust, mN	δThrust, mN
1	0.0201383	1.17E-5	0.19749	0.00011
2	0.0535133	2.29E-5	0.52479	0.00022

Raw data are corrected for the calibration gain calculated by evaluating the response of the thrust balance to a known applied force produced by means of the weights shown in Table 16. Although the evaluation of the calibration gain was carried out mainly by the test engineers at Aerospazio, with the supervision of the author, it is reported here for a better clarity. Data for application/removal of calibration weights are fitted linearly: the reciprocal of the line slope represents the correction factor for the raw thrust. A different calibration gain is determined for each operational point in order to take into account the variations of the thrust balance's behaviour: in particular the application/removal of calibration gain is superimposed to the thrust measurements. The calibration gain for the cold gas thrust measurements and two examples for the discharge thrust measurements are shown in Figure 70 and Figure 71:

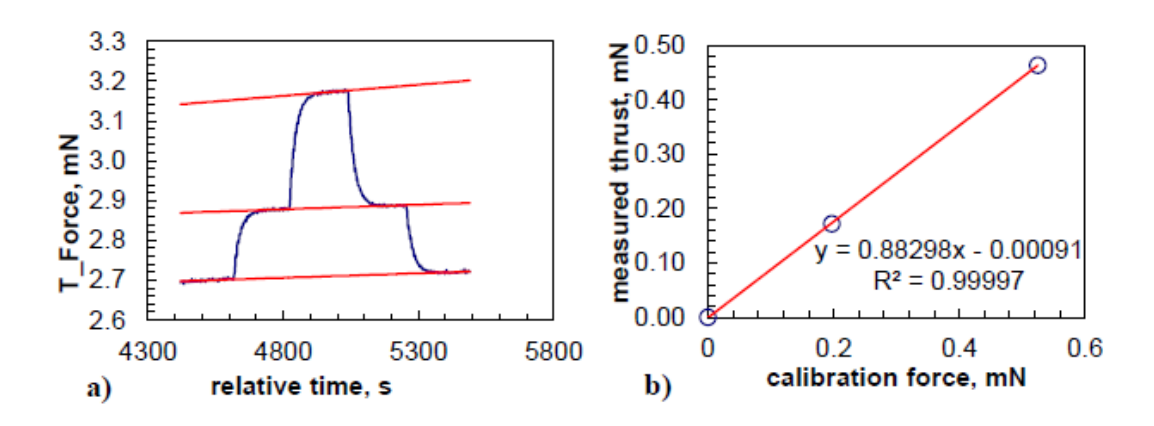


Figure 70 – Calibration graphs for cold gas thrust measurements on the T6 HCT

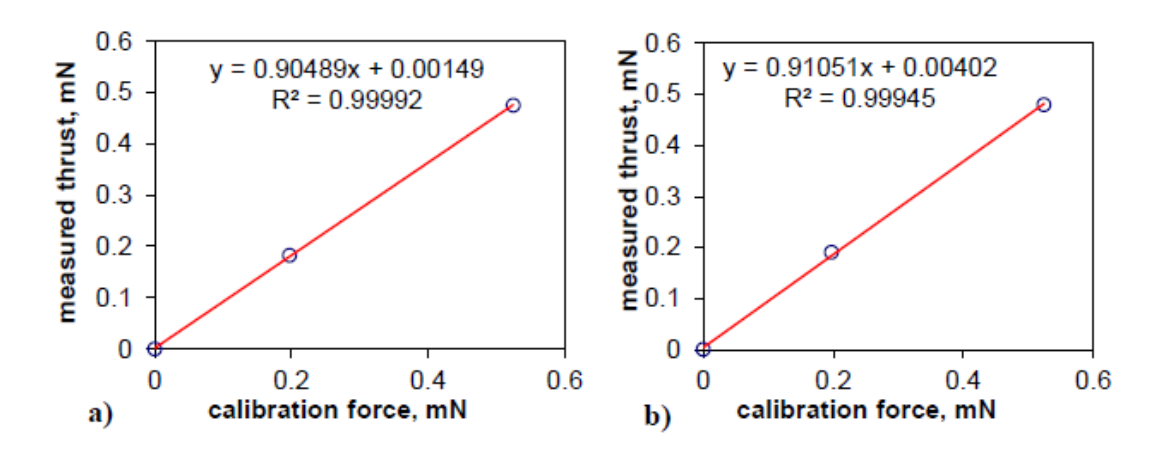


Figure 71 – Calibration graphs for discharge with magnetic field on the T6 HCT a) $10A\ 4\ scm$ and b) 15A 8 sccm

The full list of the values of the calibration gains is reported in Table 17 for the T5K and in Table 18 for the T6 HCT.

Table 17 – Calibration gain for the T5K HCT tests at AER

Current, A	Mass Flow Rate, sccm	Calibration Gain
1.5	2	0.893
1.5	4	0.895
2	2	0.888
2	4	0.894
2	6	0.895
2.5	2	0.890

Table 18 - Calibration gain for the T6 HCT tests at AER

Current, A	Mass Flow Rate, sccm	B, gauss	Calibration Gain
10	4	0	0.90373
10	4	86	0.90158
10	6	0	0.9087
10	O	86	0.90489
10	8	0	0.90782
10	o	86	0.90533
10	10	0	0.89897
10	10	86	0.91346
15	4	0	0.90433
13	4	86	0.90452
15	6	0	0.91468
13	6	86	0.87249
1.5	8	0	0.90246
15		86	0.91051
1.5	10	0	0.94312
15		86	0.92718

IV.3.6.3. Error Budget

For better clarity, it is worth to point out that the evaluation of the thrust balance error budget was completely carried out by the author. The total uncertainty of the mean value of the thrust obtained at AER is a combination of three different types of uncertainties:

- Uncertainty on the calibration gain
- Uncertainty on the raw thrust reading
- Uncertainty on the thrust fitting

IV.3.6.4. Uncertainty of the calibration gain

As explain in par. IV.3.6.1, the uncertainty of the overall thrust balance calibration gain C_G replaces the uncertainty on the voice coil characteristic constant gain C_V . The list of the calibration gains for the T5K and T6 HCTs test is reported in Table 17 and Table 18. Each calibration gain was used to correct the raw thrust of the relative set-point. The uncertainty used for all the calibration gains is the standard deviation of all of the C_G values listed as reported in [99]:

$$\delta C_G = \sqrt{\frac{1}{n} \sum \left(C_{Gi} - \overline{C_G} \right)^2}$$
 (4.3)

where $\overline{C_G}$ is defined as [99]:

$$\overline{C_G} = \frac{1}{n} \Sigma C_{Gi} \tag{4.4}$$

This value was used rather than the uncertainty of each fitting since it gives more confidence and a unique value.

The uncertainty of the calibration gain for the tests with the T6 HCT is then δC_G =0.015 and represents an error in the range 1.81% to 1.95%, whereas that for the T5K is δC_G =0.0029 representing an error of about 0.33%.

IV.3.6.5. Uncertainty of the raw thrust reading

Small oscillations of the thrust balance can cause uncertainties in the reading of the raw thrust as shown in Figure 72, where the red line shows the filtered signal. This can be quantified in $\delta T_R = \pm 15 \, \mu \text{N}$ taking an average peak to peak value.

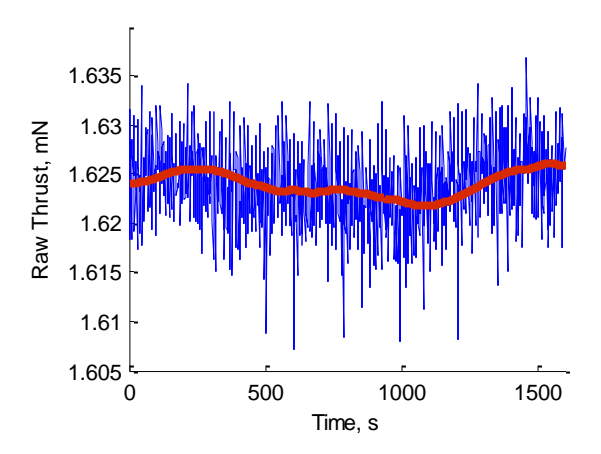


Figure 72 – Oscillations in the raw thrust

IV.3.6.6. Uncertainty of the measuring system

The raw thrust data at AER is fitted linearly before and after the switch-off, then the fit is extrapolated backwards at the exact time of the switch off (green square). The difference between the two interpolating lines at the switch-off is the raw thrust. The uncertainty δT_F is relative to the precision of the linear fit hence depends on the measurements; however it is in the range 4% to 7%. This procedure is used since the

main cause of the change in the drift may be due to the cables connected to the thrust balance. When the thrust is on the cables are overheated and their elastic properties change, and when the current is switched off the drift changes because the elastic properties of the cables are going back to the 'cold' values.

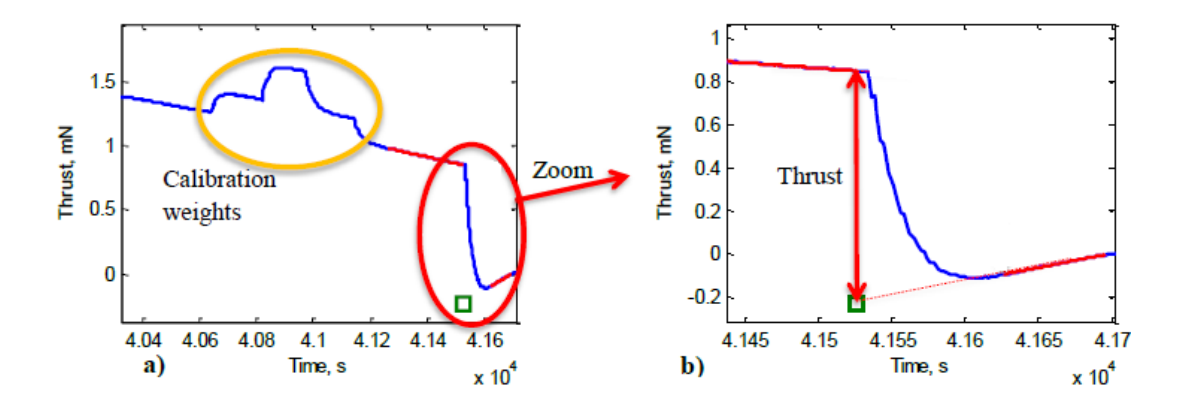


Figure 73 – Sensor trace at AER on the T6 for 8sccm and a) 10A, B=0 and b) zoom

IV.3.6.7. Summary of the uncertainties

Following what discussed in paragraphs 0 to IV.3.6.6, the error budget for the T5K and T6 HCTs thrust at AER is:

Table 19 – Calibration gain for the T5K HCT tests at AER

Quantity	Error Budget		
Quantity	Т5К НСТ	Т6 НСТ	
δC_G	0.33%	±1.81% to ±1.95	
δT_R	$\pm 2.4\%$ to ± 4	<<1%	
δT_F	$\pm 4\%$ to $\pm 7\%$	$\pm 4\%$ to $\pm 7\%$	
$\delta Thrust$	Max 8.1%	Max 7.3%	

IV.4. Test Equipment and Set-Up at UoS

IV.4.1. Vacuum Rig and diagnostic

The vacuum chamber at the UoS was previously used to characterize the hollow cathode of the UK-25 ion engine [16] and HCTs based on the T5 and T6 HCs [6, 12]: it consists of a stainless steel chamber 500 mm in diameter and 500 mm long, with an ISO 500 chamber door with five integrated DN40CF feedthroughs allowing for electrical and fluidic connections. At the bottom side an ISO 160 port allows for

the connection of the pumping system, while another ISO 160 port allows for optical access on the right hand side. A KF25 and a KF 40 port on the top of the chamber are used for the pressure gauges and a DN40CF port at the rear is used for inlet and outlet water connections to a cylindrical cooled copper shroud used as heat sink inside the chamber.

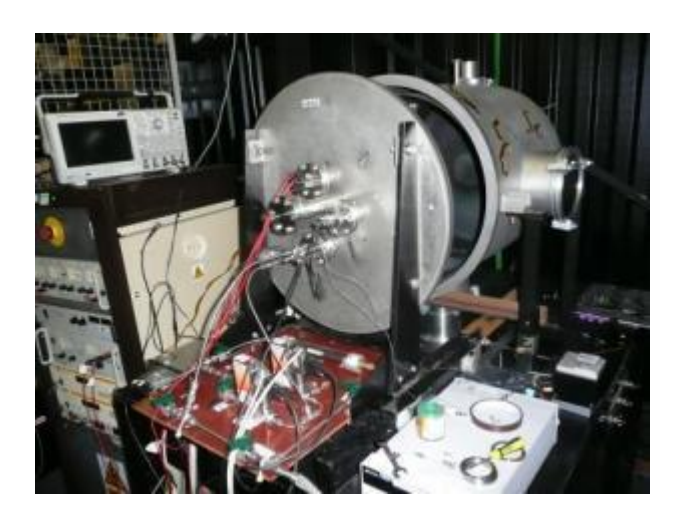


Figure 74 - The vacuum chamber at UoS

The pumping system is composed of a water cooled molecular pump (Pfeiffer Balzers TPH 520KTG, 500 l/s) with a control unit made of a Balzers TCP 380 drive unit and a Balzers TCS 303 controller and backed by a rotary vane pump (Pfeiffer Balzers DUO 016B). Vacuum pressure is monitored via a Balzers TGP 300 pressure gauge package consisting of a pirani gauge $(1000 - 5.4 \times 10^{-4} \text{ mbar})$ and a cold cathode gauge $(5 \times 10^{-3} - 1 \times 10^{-9} \text{ mbar})$. The facility ultimate pressure is $2.1 \times 10^{-5} \text{ mbar}$.

IV.4.2. Fluidic Line

The fluidic line is shown in Figure 75: xenon gas grade 4.8 is supplied from a cylinder which has a plug valve and a pressure reducer. To supply the cathode the gas is driven towards the oxygen trap (*Cole Palmer* 40 ml) and then towards one of the two *Bronkhorst* mass flow controllers (MFCs) and then into the vacuum chamber. All the fluidic lines upstream of the MFCs and the venting pipe are 1/8" in diameter. Immediately downstream the MFCs the pipe is still 1/8" but before entering the vacuum chamber via feedthrough a reducer to 1/16" is placed so that, inside the chamber, the pipe is always 1/16". A 1/16" pipe has been used inside the

chamber to minimize the amount of gas left in the pipe once a zero mass flow rate is commanded to the MFC. A series of On/Off valves are in place to ensure that each part of the fluidic line can be evacuated independently hence minimizing the chances of oxygen contamination and preventing the poisoning of the insert.



Figure 75 – Fluidic lines at UoS

IV.4.3. Test equipment

IV.4.3.1. With the T6 HCT

Two power supplies are needed to operate the optimised T6 HCT: one for the cathode heater (PowerBox Lab605, 32V-5A), which provides the 3.3A (and up to 22V) required to heat the insert to the emissive temperature, and one for the discharge (Glassman LV80-37, 80V-37A). Two more power supplies are included in the set-up: a PowerBox Lab622 (32V-2A) allowing for the use of the magnetic coil and a Bertan 205B-01R (1kV-30mA) allowing for a high voltage strike to ignite the discharge in the event of repeated unsuccessful attempts with the low voltage power supply. The minus connection of the high and low voltage discharge power supplies and that of the cathode heater power supply are grounded and only the magnet coil power supply was left floating. The overall test setup for the tests at the University of Southampton is reported in Figure 76, where it can be seen how the cathode body and one connection of the heater were grounded via the thrust balance and the vacuum chamber.

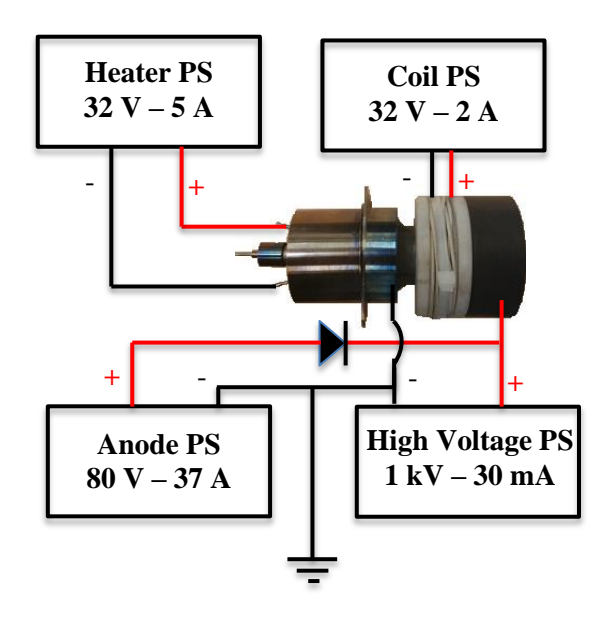


Figure 76 – Electric set-up at UoS for the T6 HCT

Discharge voltage including plasma noise and instabilities are monitored via a Tektronix digital oscilloscope connected with one terminal at the common ground and one terminal at the anode power supply feedthrough terminal.

IV.4.3.2. With the T5A HCT

A similar set-up is used for the experiments on the T5 HCT at the UoS. The only difference is that a power supply for the magnetic coil is no longer needed and that the cathode heater is left floating hence the heater power supply connection terminals are left floating as shown in Figure 77:

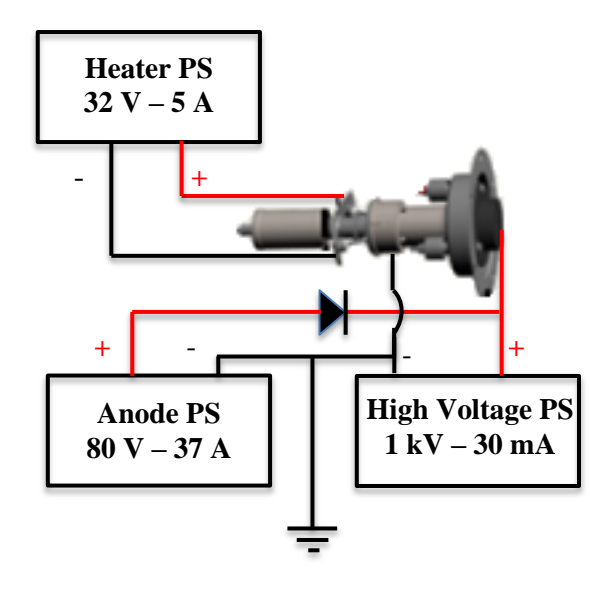


Figure 77 – Electric set-up at UoS for the T5 HCT

IV.5. The thrust balance at the UoS

The thrust balance is a hanging pendulum shown in Figure 78 and Figure 79: it consists of a stainless steel swinging arm fixed to an aluminium support structure via a flexural pivot (*Riverhawk* 6012-800 [100]).

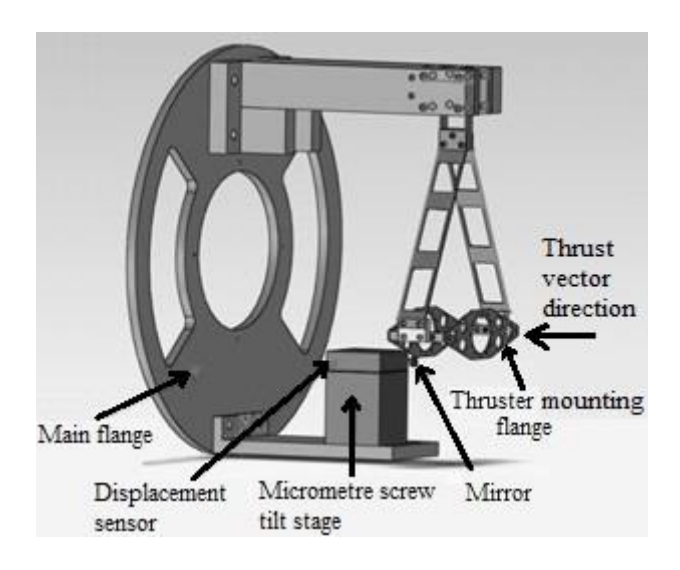


Figure 78 - Complete thrust balance assembly schematic

The thruster is mounted on the swinging arm on the mounting flange. When the device is operated giving a certain thrust, the swinging part of the balance reaches a new equilibrium position which is determined by the balance of the torques generated by the thrust, the action of the gravity and the reaction of the torsional spring constant of the flexural pivot. The displacement of the arm is measured as the distance of the mirror, which is connected to the swinging part of the balance, to an optical sensor [101] which is placed on a tower as shown in Figure 78. The position of the optical sensor can be adjusted by using two micrometre screws and a tilt stage for its alignment with the mirror.

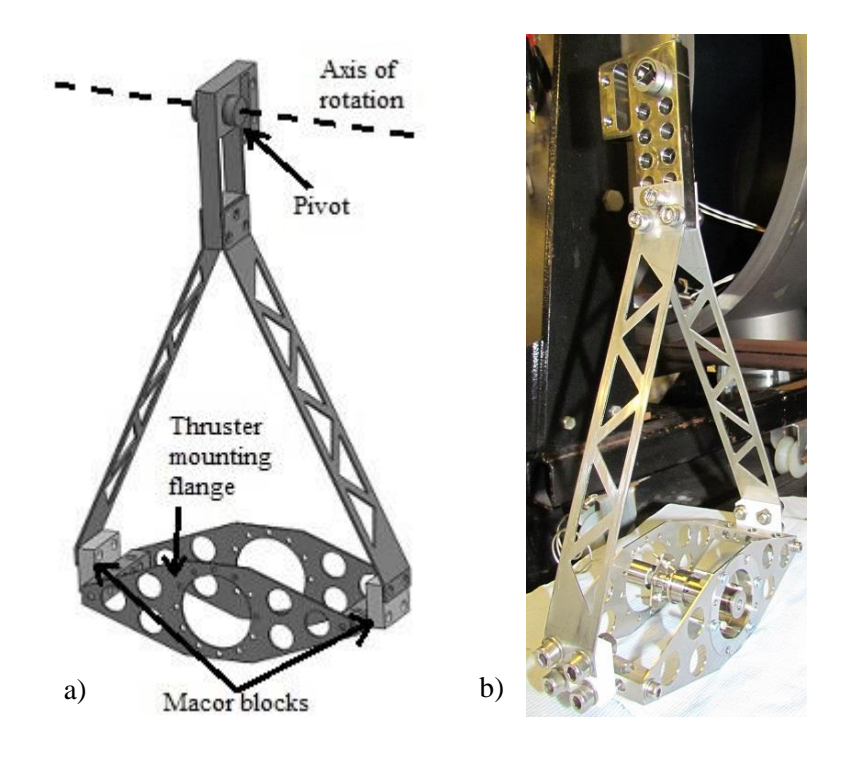


Figure 79 - Swinging arm of the thrust balance a) CAD model b) manufactured

The fluidic and electrical connections needed to operate the thruster are shown in Figure 80: they are mechanically constrained via a clamp to the swinging part of the balance. This ensures that these connections will have minimal effects on the dynamic response of the thrust balance.

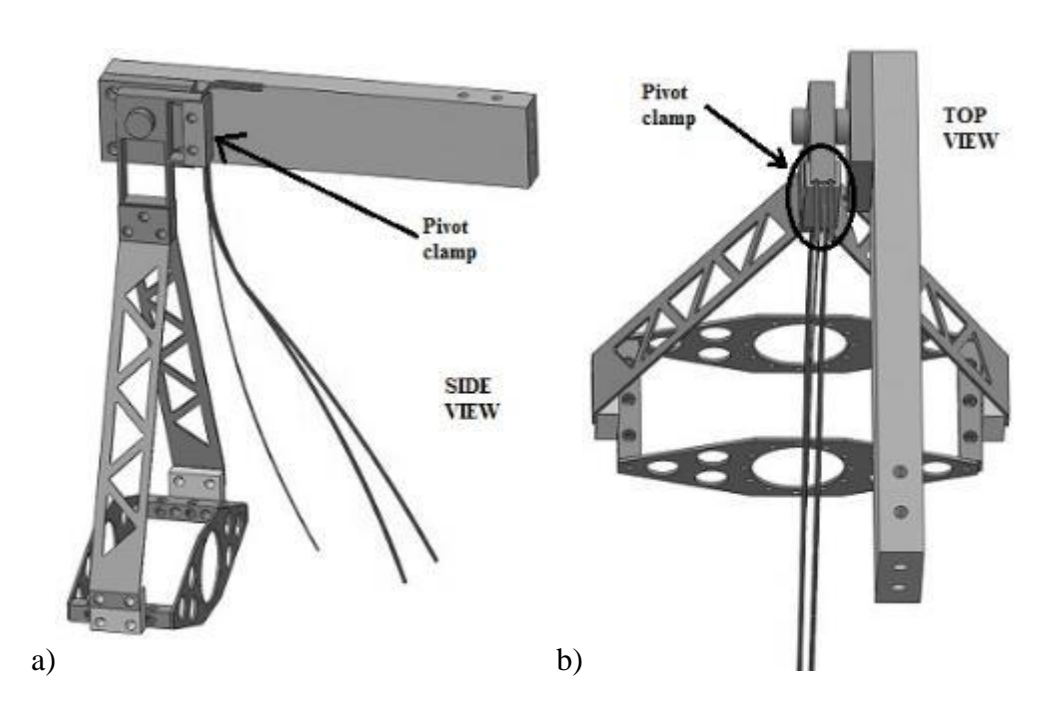


Figure 80 - Electrical connections constrained to the thrust balance

The displacement sensor used is a 3R class laser interferometer (EUCLID) with an operating wavelength of 667 nm and an optical power $<50\mu W$ [101]. In order to obtain reliable measurements, the interferometer needs to be aligned to the mirror placed on the mounting flange of the thruster on the movable part of the balance. The interferometer has an optimized distance, called 'sweet-spot' W_D , of 6 mm from the mirror at which the tolerance to misalignment of the target mirror is maximised, and a working range W_R of ± 3 mm from the sweet-spot [101].

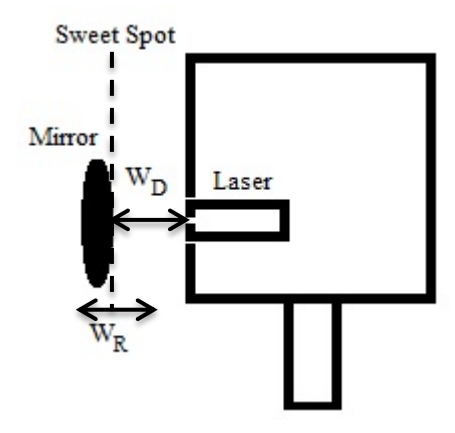


Figure 81 - Working distance and sweet-spot of EUCLID

The mirror used in the present thrust balance configuration is a *Thorlabs* PF05-03-F01 [102], which reflectivity and flatness are respectively >0.9 and λ /10 and meet the interferometer specifications which require a mirror reflectivity >0.9 and a flatness of at least λ /4 [101]. The EUCLID interferometer comes with an electric box for the main PC and power connections and a *Labview* software which provides the state of the alignment and the real-time tracking of the mirror with the possibility of data logging.

IV.5.1. Thrust Balance Characterization

IV.5.1.1. The working principle

The thrust balance is schematically shown in Figure 82 in the two equilibrium positions, i.e. when no thrust is applied and when the thrust is on.

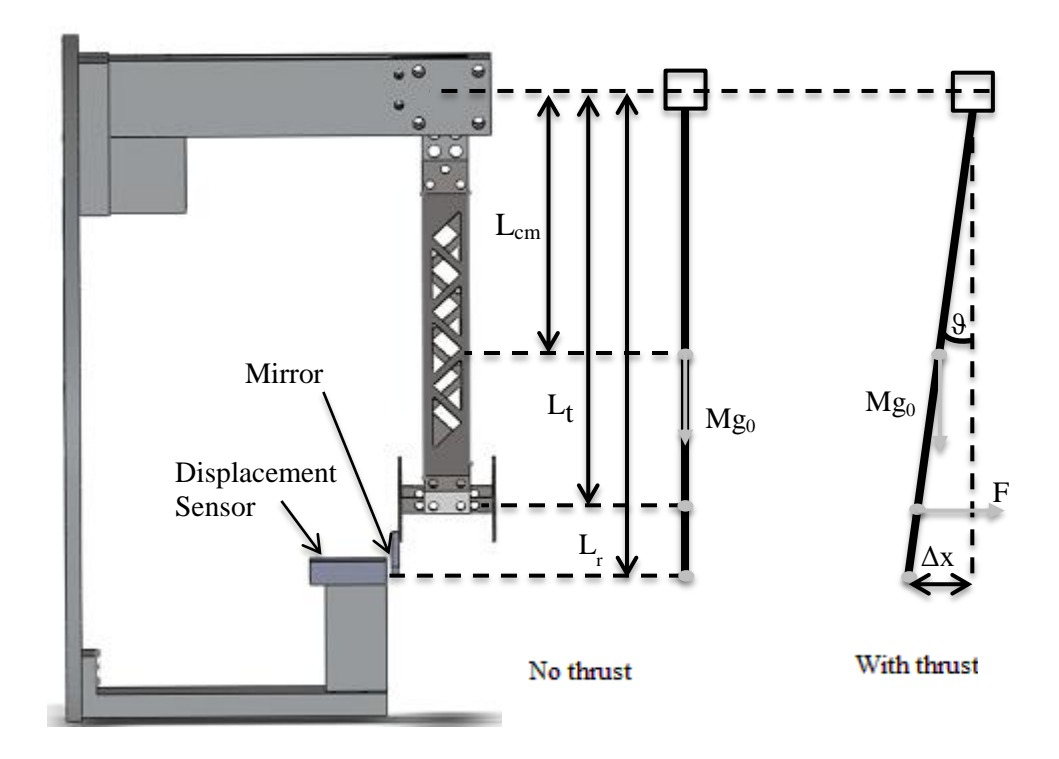


Figure 82 - Thrust balance, schematics (not in scale)

In Figure 82, M and L_{cm} are the balance mass and the distance from the axis of rotation to the balance centre of mass, L_r is the distance from the axis of rotation at which the mirror (i.e. the reading of the linear displacement) is placed, θ and Δx are respectively the angular and linear displacement, g is the standard gravity, F is the thrust and L_t the distance from the axis of rotation to the position where the thruster is mounted. Assuming $sin(\theta) = \theta$, i.e. the balance angular displacement is small, the sum of the torques acting on the thrust balance can be expressed as:

$$J_{bal}\ddot{\mathcal{G}} + \Gamma \dot{\mathcal{G}} + k\mathcal{G} + ML_{cm}g_{0}\mathcal{G} = F L_{t}$$
(4.5)

where $\Gamma \dot{\mathcal{G}}$ is the viscous friction term and J_{bal} and k are respectively the moment of inertia (with respect to the axis of rotation) and the torsional spring constant of the assembly formed by the pivot, the cables and propellant pipe. Dividing both the RHS and the LHS by J_{bal} , equation (4.5) takes the shape of the classical pendulum equation:

$$\ddot{\mathcal{G}} + 2 \varsigma \omega_n \dot{\mathcal{G}} + \omega_n^2 \mathcal{G} = \frac{F L_t}{J_{bal}}$$
(4.6)

where ζ is the damping coefficient, expressed as:

$$\varsigma = \frac{\Gamma}{2J_{hal}\omega_n} \tag{4.7}$$

and ω_n is the natural angular frequency of the balance expressed as:

$$\omega_n = \sqrt{\frac{k + ML_{cm}g}{J_{bal}}} = \sqrt{\frac{K}{J_{bal}}}$$
(4.8)

In equation (4.8) K indicates the total torsional spring constant of the whole balance assembly, including the gravity effect. For small angular displacement $(sin(\theta) = \theta)$ it is possible to write:

$$\mathcal{G} = \frac{\Delta x}{L_{\cdot \cdot}} \tag{4.9}$$

Combining equations (4.6), (4.8) and (4.9) one can obtain an equation for the thrust in stationary conditions as:

$$F = \frac{\omega_n^2 J_{bal} \Delta x}{L_t L_r} \tag{4.10}$$

Equation (4.10) shows that in order to calculate the thrust five parameters are needed. The two geometric dimensions L_t and L_r , defined in Figure 82, were measured with a calliper and are respectively 27.1 cm and 34.5 cm with an uncertainty of 0.5 cm, hence $\pm 1.85\%$ and $\pm 1.45\%$ respectively. The other parameters needed are moment of inertia of the balance assembly J_{bal} , the natural angular frequency ω_n and the linear displacement Δx .

IV.5.1.2. Linear displacement evaluation

As discussed already in paragraph IV.5, the distance between the interferometer and the mirror, fixed to the balance swinging arm, is monitored and measured in real-time. Figure 83 shows an example of an unfiltered sensor trace acquired in real-time using the EUCLID interferometer with the T6 HCT running in discharge mode with xenon at 10 sccm and 10 A.

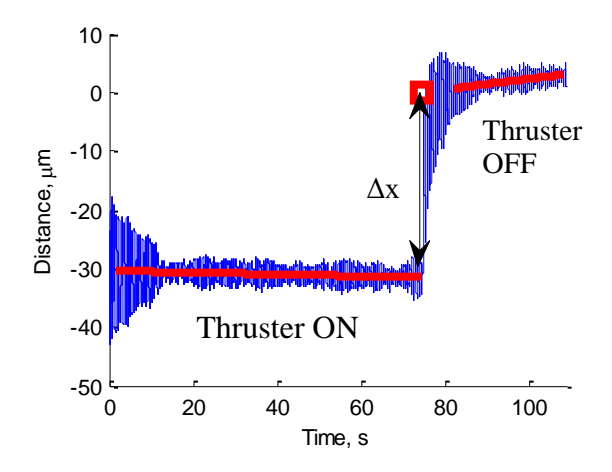


Figure 83 - Displacement sensor trace for a T6 in discharge mode at 10 A and 10 sccm

It is possible to obtain an instantaneous measurement of the linear displacement Δx due to the application of the thrust with the following procedure:

- 1. Turn on the thruster and set the desired set-point
- 2. wait until the thruster and the balance have reached steady state thermal condition

This will result in a constant value of the mirror to sensor distance signal

- 3. take a displacement reading
- 4. <u>turn off the discharge (by switching off the anode power supply) and the propellant feed (by commanding zero flow to the mass flow controller) at the same time</u>

By doing so the thrust will reduce to zero and the balance will go to its equilibrium position at no thrust.

- 5. take a second displacement reading
- 6. make the difference between the two displacement readings to obtain the linear displacement Δx due to the thrust produced by the HCT

When the propellant feed is turned off by setting to zero the mass flow controller, the remaining gas in the pipe downstream of the MFC (hence between the MFC and the HCT) will flow through the thruster. The time needed for the gas to flow out is directly proportional to the pipe length and determines the time needed for the thrust to decrease to zero.

It needs to be noted that the equilibrium position at which the balance will move after the thruster has been switched off is, in general, different from the original balance equilibrium position (i.e. prior the thruster being switched ON).

This is mainly due to the thermal expansion and thermal gradients of the balance and of the feed pipes and power lines attached to it caused by the thruster power dissipation.

Considering this it can be understood that, if the thrust goes to zero instantaneously, the balance equilibrium position (recorded in step 5) will be relative to the same thermal state at which the thrust displacement was measured (step 3 above). Hence making the difference between these two readings to obtain Δx (step 6) will automatically eliminate the influence of any potential thermal drift causing a shift in the balance position.

On the contrary, if the thrust goes to zero slowly after the HCT switch off, the balance thermal state will be different in the measurement taken at step 3 and 5 above hence producing a value of Δx that is affected by thermal drifts

To reduce as much as possible the time needed for the thrust to decrease to zero, the fluidic line and the thrust balance at the UoS have been designed in such a way that the part of the pipe between the MFC and the HCT is as short as possible (about 60 cm). In this way the remaining gas will flow quickly out the HCT and the thrust will decrease rapidly resulting in a sharp gradient of the interferometer signal as shown in Figure 83. Moreover the anode power supply is switched off at the same time as the flow rate to avoid large discharge voltage increases which would damage the HCT.

To reduce to a minimum the uncertainties introduced by this finite time of decay of the thrust, the raw sensor data before and after the thruster switch off are fitted with two straight lines to evaluate the linear displacement Δx at the exact time of the turn off as shown in Figure 83. It must be noted that the displacement values in the sensor traces are negative since the swinging arm of the balance moves towards the sensor (hence reducing the mirror-to-arm distance) when the thruster is on.

The oscillations of the balance around its equilibrium position are the main cause of error on the displacement, and their amplitude depends on the environment around the vacuum chamber and on the thrust level at which the device is run. For instance, the analysis of the sensor trace in Figure 83 leads to an average linear displacement of 32.6 μ m and to uncertainty of about 1.6 μ m, hence an error of 4.9%, due to the balance oscillations around its equilibrium position.

The same procedure can be followed to evaluate the linear displacement in cold gas and resistojet mode: in these cases only the propellant feed has to be tuned off to let the balance go back to its original equilibrium position, since there is no arc discharge ignited.

IV.5.1.3. Natural angular frequency evaluation

The balance assembly natural angular frequency ($\omega_n=2\pi f_n$) depends on the total torsional spring constant and the moment of inertia of the whole balance assembly, as shown in equation (4.8). Hence, once the geometry of the balance is fixed, it depends on the thruster geometry and position and on the electrical cables and the fluidic pipe downstream the connection to pivot shown in Figure 80 (in particular their moment of inertia). The natural angular frequency was hence evaluated before every test campaign. From the acquired raw sensor trace, shown in Figure 83, it is possible to obtain the balance spectrum signal via a Fourier Transform (FT). The natural frequency f_n is the value at which the FT spectrum signal shows a peak. An example of FT spectrum signal for the evaluation of the natural frequency is shown in Figure 84.

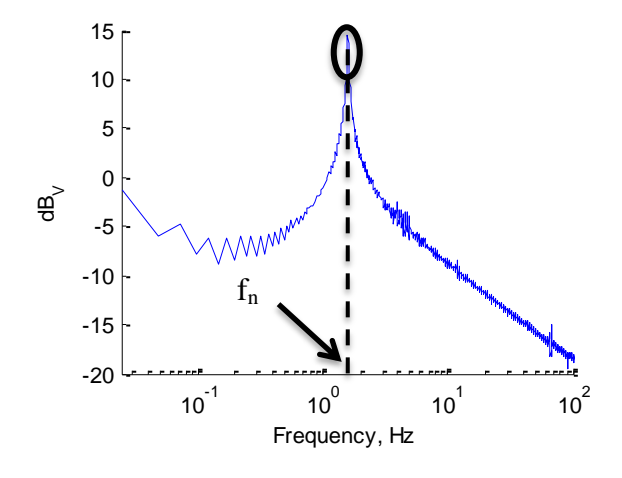


Figure 84 - Example of Fourier Transform to evaluate the natural frequency

The uncertainty in the natural angular frequency is given by [103]:

$$\delta\omega_n = 2\pi f_s \frac{1}{2(P/2+1)} \tag{4.11}$$

where *fs* is the signal sampling frequency and *P* is the power of 2 closest to the number of acquired samples. The uncertainty in the natural angular frequency has an order of magnitude of 1 mHz since the signal was acquired using an oscilloscope with a sampling frequency of 25 kHz for at least 5 minutes every time. This uncertainty is of the order of 0.1% since the natural angular frequency has an order of magnitude of 1 Hz, hence it can be neglected.

IV.5.1.4. Moment of inertia evaluation

A dynamic calibration of the thrust balance assembly can be carried out to obtain the moment of inertia of the thrust balance assembly J_{bal} , which is needed to calculate the thrust as per equation (4.10). The dynamic calibration consists in applying different known weights to the balance and obtaining the new natural angular frequency of the balance and weights system using the procedure shown in paragraph IV.5.1.3. In fact, when an extra weight is attached to each side of the balance at a distance L_m from the centre of rotation, the new natural angular frequency of the balance and weights system can be written following the procedure carried out in equation (4.8) as:

$$\omega = \sqrt{\frac{K + 2mL_m g}{J_{bal} + 2J_m}}$$
(4.12)

where J_m is the moment of inertia of the weight relative to the balance rotational axis. Equation (4.12) can be written in a different way as:

$$2\omega^2 J_m - 2mL_m g = -J_{bal}\omega_n^2 + K {4.13}$$

The LHS of equation (4.13) is easily obtained when the extra weights have a known mass m and distance L_m =28.2 from the balance axis of rotation, have a simple shape such to calculate J_m and the new natural angular frequency of the balance and weights system ω is measured. Repeating this procedure several times with different weights it is possible to obtain different values for the LHS of equation (4.13) and then fit the data linearly in order to obtain a value for the balance total moment of

inertia J_{bal} and total torsional spring constant K. In particular the absolute value of the slope of the linear fit will be J_{bal} , whereas the intercept is K.

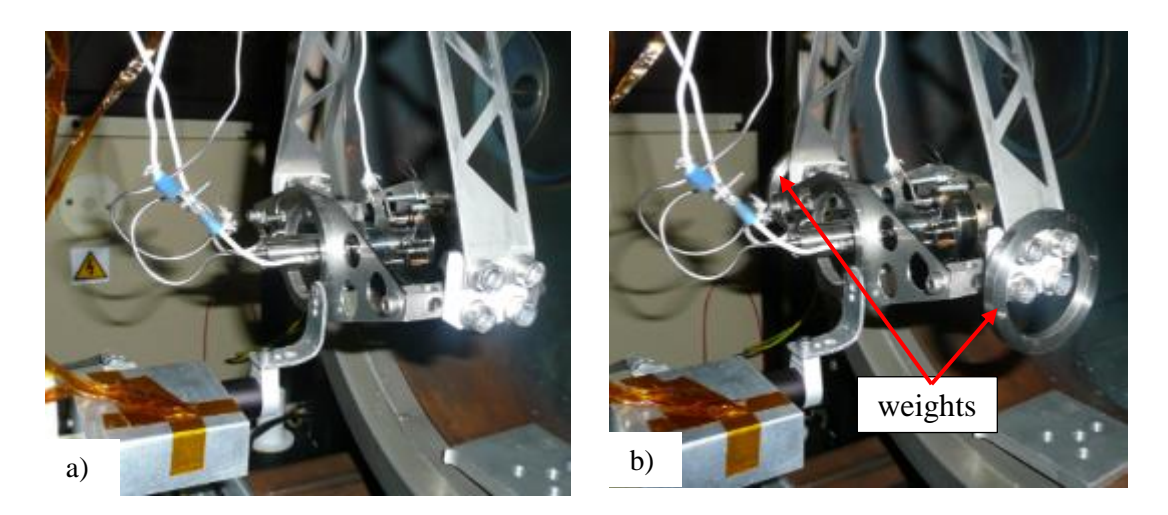


Figure 85 - Thrust balance a) without and b) with weights

Two pairs of different annular weights have been manufactured, with their geometrical features shown in Figure 86 and Table 20:

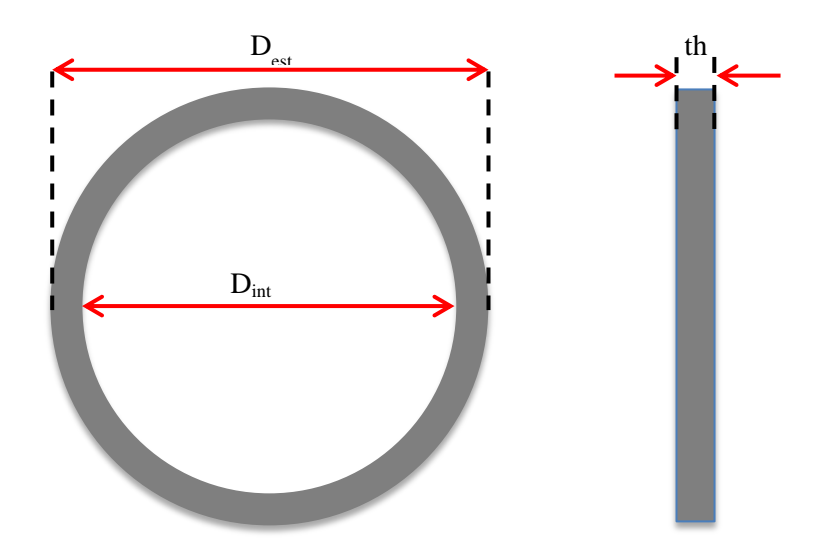


Figure 86 - Geometrical parameters of the weights

Table 20 - Geometrical values of the weights

Weight	'Small'	'Big'
D_{ext} , mm	54	54
D_{int} , mm	42	42
th, mm	5	15
mass, g	14.2	35.6

In Table 21 the different configurations of weights used for the dynamic calibration of the T5 and T6 HCTs are reported:

Table 21 - Configuration of weights used

Config no	Weights used		
Config. no.	Left hand side	Right hand side	
1	-	-	
2	Small	Small	
3 (shown in Figure 85)	Big	Big	
4	Big+Small	Big+Small	

Figure 87 shows the results of the dynamic calibrations with the T5A and T6 HCTs, with the four balance-weights configurations were fitted with a straight line as per equation (4.13). The new natural frequency of the balance-weights system was obtained more than fifteen times for each configuration, but only the mean values are reported in Figure 87 for clarity. The standard deviation of the mean values are not shown in Figure 87 since they are always <<1% hence negligible.

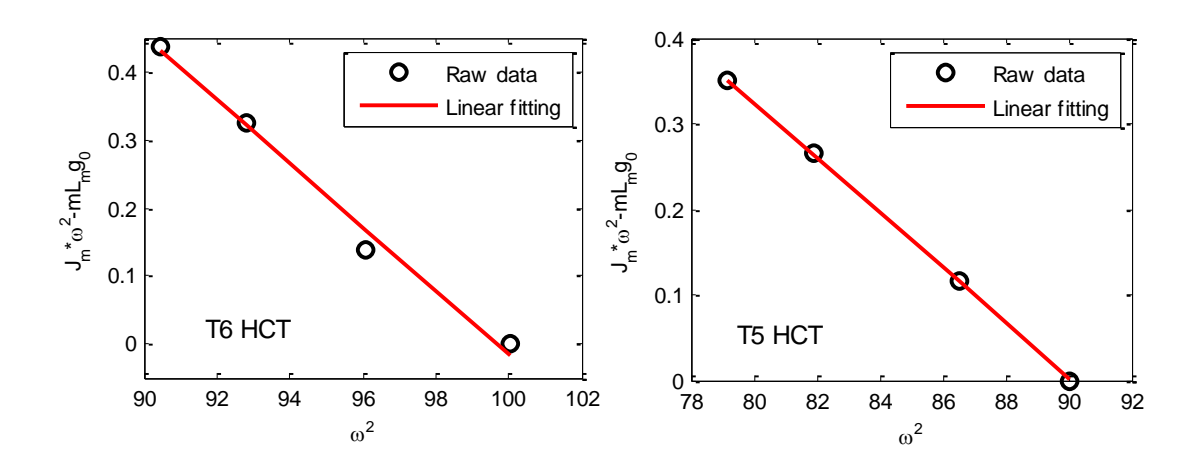


Figure 87 - Dynamic Calibration for the calculation of the moment of inertia for the T6 and T5A balance assembly

The moment of inertia for the two balance assemblies are reported in Table 22. The uncertainty of the moments of inertia were calculated as those of the fitting, in agreement with what is reported in [99], and were found to be respectively 2.6% and 8% of the nominal J_{bal} value of the T5A and T6 HCT balance assemblies.

Table 22 – Moment of inertia and uncertainty

Balance Assembly	Т5А НСТ	Т6 НСТ
J_{bal} , kg m ²	0.0321	0.0466
δJ_{bal} , kg m ²	± 0.0008	± 0.0037

IV.5.2. Evaluation of thermal effects on the measurements

The heat produced by inefficiencies of the device may cause thermal drifts which in turn can affect the calculation of the thrust: the distance shown in Figure 83, for instance, increases after the device switch-off because of thermal effects. In the calculation of thrust, referring to equation (4.10), the parameters which may be affected by thermal effects are the balance moment of inertia, the geometrical parameters L_t and L_r and natural angular frequency. If an increase of 500 °C, which is a very pessimistic hypothesis, is considered, the additional error due to thermal expansion on L_t and L_r will be about 0.7% since the balance is made of stainless steel, which has a thermal expansion coefficient of $17x10^{-6}$ K⁻¹ [104]). The error on the moment of inertia J_{bal} is then twice that on L_t and L_r hence about 1.4% since J_{bal} scales as the square of the balance dimension $(J_{bal} \sim mL^2 \mapsto \delta J_{bal}/J_{bal} \sim 2\delta L/L)$ [99]. The increase in temperature will affect also the properties of the pivot, in particular on its spring constant k hence on the natural angular frequency of the balance assembly as per equation (4.8). Parts in Macor, which has a thermal conductivity as low as 1.46 W m⁻¹ K⁻¹ [105], are employed in order to reduce the heat conduction towards the pivot: they are placed between the thruster mounting balance and the swinging balance arms as shown in Figure 79. The linear displacement Δx is not evaluated with respect to a "zero" equilibrium position obtained before turning on the thruster but it is obtained instantaneously at the turn off time from the displacement sensor trace as described in paragraph IV.5.1.2. The obtained values of Δx and ω_n used in equation (4.10) hence take automatically into account the thermal effects which may possible arise hence no errors relative to Δx and ω_n should be included in the error budget because of the thermal effects. The knowledge of the value of k and/or of its trend with temperature is also not needed thanks to the particular thrust measurement procedure. Following the measurement technique discussed in paragraph IV.5.1.2 hence results in negligible thermal drifts

since the thruster has reached thermal equilibrium and at the switch off, by the time the thrust goes to zero, the thermal loads do not change rapidly. A different measurement technique would result in having to separate the thermal drift from the thrust signal. If the thrust would have been measured at the switch on, for example, the thermal loads coming from the heater would have caused a considerable thermal drift.

IV.5.3. The error budget

The uncertainty of the experimental mean value of the thrust, which is obtained using equation (4.10), is calculated within this paragraph. In equation (4.10) Δx and ω_n are obtained from the displacement sensor trace, J_{bal} is obtained with the dynamic calibration and L_t and L_r have been measured with a calliper, and. The error on the thrust can be expressed as reported in [99]:

$$\delta F = F \sqrt{\left(\frac{\delta L_t}{L_t}\right)^2 + \left(\frac{\delta L_r}{L_r}\right)^2 + \left(\frac{\delta J_{bal}}{J_{bal}}\right)^2 + \left(2\frac{\delta \omega_n}{\omega_n}\right)^2 + \left(\frac{\delta \Delta x}{\Delta x}\right)^2}$$
(4.14)

The first three terms in the square root in equation (4.14) include the error term due to the thermal effects, as shown in equation (4.15) in an example for L_t :

$$\left(\frac{\delta L_t}{L_t}\right)^2 = \left(\frac{\delta L_t}{L_t}\right)_{no \ thermal}^2 + \left(\frac{\delta L_t}{L_t}\right)_{thermal}^2$$
(4.15)

The uncertainty on the linear displacement Δx depends on the thrust level and it is usually close to 5%. The error budget for the T6 HCT balance assembly is reported in Table 23:

Table 23 - Error budget for the T6 HCT in discharge mode

Quantity	Error	Thermal effects at 500 °C	Total error at 500 °C
L_t	±1.85%	±0.7%	±1.98%
L_r	$\pm 1.45\%$	±0.7%	$\pm 1.61\%$
$oldsymbol{J}_{bal}$	$\pm 8.0\%$	$\pm 1.4\%$	$\pm 8.1\%$
ω_n	<<1%	0%	<<1%
Δx	Measurement dependent ~ 5%	0%	Measurement dependent ~ 5%
Thrust	~ ±9.7%	±1.7%	~ ±9.9%

The error budget for the T5A HCT balance assembly is reported in Table 23:

Table 24 - Error budget for the T5A HCT in discharge mode

Quantity	Error	Thermal effects at 500 °C	Total error at 500 °C
L_t	±1.85%	±0.7%	±1.98%
L_r	$\pm 1.45\%$	±0.7%	±1.61%
$oldsymbol{J}_{bal}$	±2.6%	$\pm 1.4\%$	$\pm 2.95\%$
ω_n	<<1%	0%	<<1%
Δx	Measurement dependent ~ 5%	0%	Measurement dependent ~ 5%
Thrust	~ ±6.1%	±1.7%	~ ±6.3%

IV.5.4. Thrust Balance Assessment

In order to assess the thrust balance developed at the UoS, the optimized T6 HCT described in IV.2.2 has been tested at both AER, with the set-up and thrust balance described in IV.3, and at the UoS. The tests were carried out in the cold gas mode, with the mass flow rate ranging 2 to 10 sccm at AER and 2.5 to 20 sccm at UoS, and in the discharge mode with a discharge current of 10 and 15 A and with and without the application of an external axial magnetic field of 86 G. In Figure 88 the cold gas thrust obtained at AER and UoS is shown:

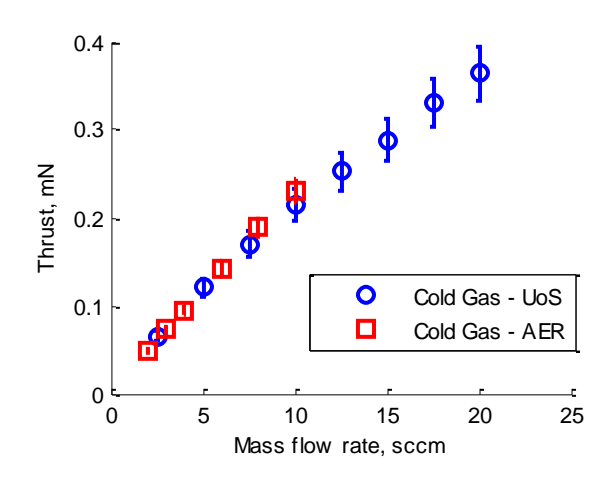


Figure 88 - T6 HCT in cold gas mode at UoS and AER

The comparison of the cold gas in Figure 88 shows a good agreement between the two sets of measurements, being always within the error bars and the maximum

error being 6.7% at 10 sccm. The thrust obtained in the discharge mode at AER and UoS with and without the magnetic field is shown in Figure 89:

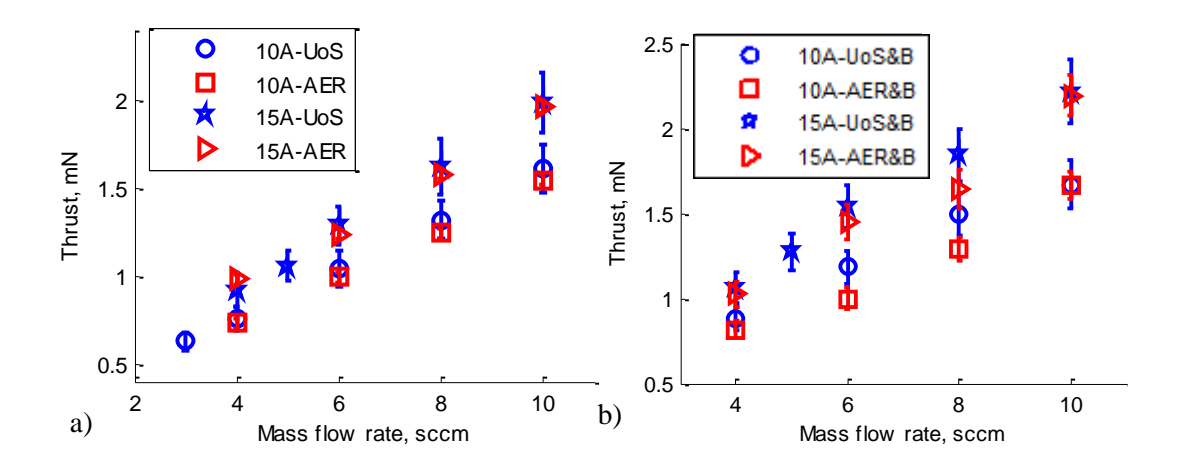


Figure 89 - Thrust at AER and UoS at 10A and 15 A a) without B and b) with the applied B $\,$

In the discharge mode the comparison between the sets of data obtained at the different facilities are in good quantitative agreement: the maximum error for the case of no magnetic field is 6.7% at 15 A and 4 sccm whereas it is 15.6% at 10 A and 6 sccm for the case of the applied magnetic field.

Since there is reasonable agreement between the data obtained with two different direct thrust balances at two different test facilities, in the next chapters only the data obtained at the UoS will be shown and discussed as no more distinctions will be made between the two sets of experiments.

Chapter V

Results and Comparison

This chapter describes the experimental results obtained during the test campaigns on the T5 and the optimised T6 HCTs held at Aerospazio and on both the T5 and the optimised T6 at the University of Southampton. The presented thrust measurements are obtained for the first time with a direct thrust balance on a HCT. Up to now, in fact, indirect thrust balances only have been used to collect the performance of HCTs [6, 12, 78], but the use of this type of balances may result in an overestimation of the real thrust value as discussed already in chapter II.

V.1. Direct Measurements on the HCTs

Before discussing the thrust measurements obtained, it is useful to remember that the experimental set-ups and the thrust measurements techniques at Aerospazio and University of Southampton are described in chapter IV. In this chapter the obtained direct thrust measurements will also be compared to the theoretical predictions. For what concerns the predictions of the performance when no magnetic field is applied the theoretical model described in chapter III has been used. In order to identify the increase in thrust due to the application of the magnetic field, the model described in [69] has been adopted. It should be noted that the section at which the arc current attaches at the anode section, needed to calculate the electromagnetic component of the thrust, was chosen to be R_a =4mm for the T6 HCT after a visual inspection at the end of the test campaigns.

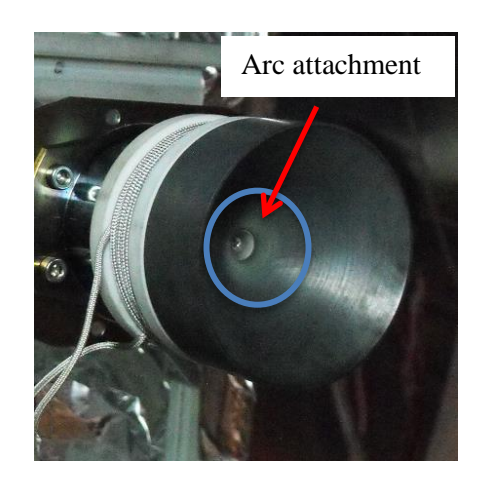


Figure 90 - Arc attachment section on the T6 HCT

The complete test overview is shown in Table 25. The T6 HCT was tested in cold gas, resistojet and discharge mode; the T5K (in the keeper configuration) was only tested in the discharge mode; the T5A (with the anode) was tested in the cold gas and resistojet mode. The idea was to compare the V-I characteristics and the thrust measurements in discharge mode of the T5A with the results obtained with the T5K. Unfortunately only the discharge characteristics at different current and thrust measurements in cold gas and resistojet mode (at 2A and 3A) were obtained from the T5K before a major failure of the vacuum system at the UoS.

Table 25 - Thrust measurements set-points

Operating mode	T5A HCT	T5K HCT	T6 HCT
Cold Gas	UoS		AER and UoS
Resistojet	UoS (2, 3 A)		UoS (1, 2, 3.3A)
Discharge	UoS (V-I only)	AER (1.5, 2, 2.5A)	UoS (10, 15, 20, 24A)
			AER (10, 15A)
Discharge with			UoS (10, 15, 20A)
applied B			AER (10, 15A)

V.2. Cold gas and Resistojet Thrust Measurements

As described in chapter II, HCTs can be operated in cold gas and resistojet mode in addition to the discharge mode, depending on the specific impulse and thrust required by the mission, and by the power and time availability. Tests in cold gas

and resistojet mode were conducted with xenon grade 4.8. In resistojet mode, the heater of the T5A HCT reached a steady value of 7.7V and 15.1V for respectively 2A and 3A, leading to an operational power of 15.4W and 45.3W. The T6 HCT was operated in resistojet mode using only one of the two available heaters, which reached a steady value of 3.1V, 11V and 22V for a power of 3.1W (at 1A), 22W (at 2A) and 72.6W (at 3.3A) respectively.

As shown in Figure 91 to Figure 93, the thrust increases linearly with the mass flow but not linearly with the applied power. The cold gas thrust for the case of the T5A HCT is in the range $50\mu\text{N}$ - $390\mu\text{N}$, whereas it is in the range $65\mu\text{N}$ - $360\mu\text{N}$ for the T6 HCT. Looking at the cases of the cold gas and the resistojet mode at 2A, the values of the thrust are essentially the same for the two HCTs; this means that the T5 HCT used in resistojet mode can heat the flowing gas more efficiently than the T6 HCT since, at 2A, it needs only 15.4W compared to the 22W needed by the T6 HCT. The reason lies within the fact that the T5 has a smaller internal insert diameter and smaller orifice hence a throat area almost 3 times smaller with respect to that of the T6. The T5 will have in turn an internal pressure about 3 times higher since the *Isp* (hence the choked velocity) is essentially the same, resulting in an increase of the thermal conductivity of the gas.

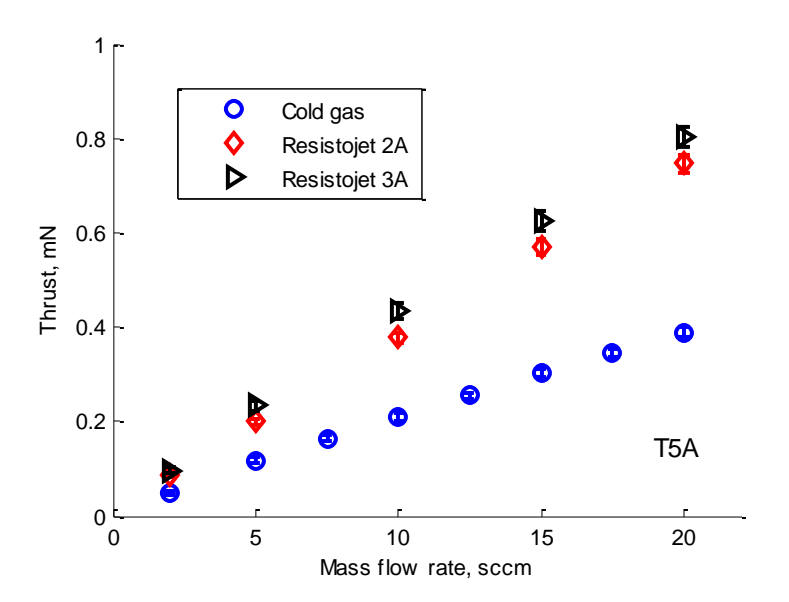


Figure 91 – Thrust in cold gas and resistojet mode for the T5A

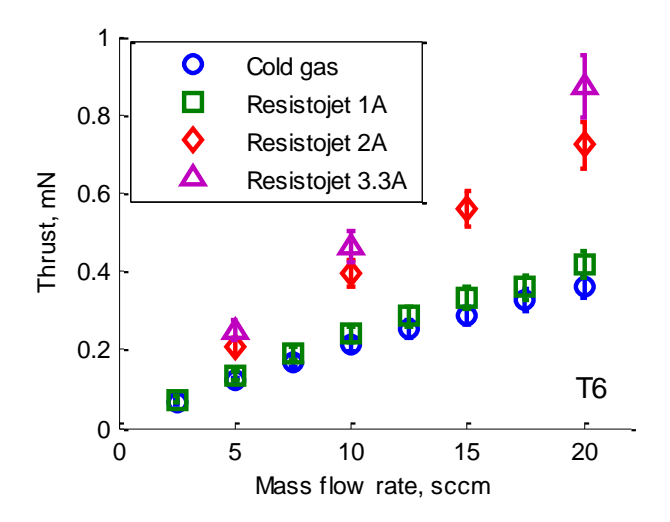


Figure 92 – Thrust in cold gas and resistojet mode for the T6

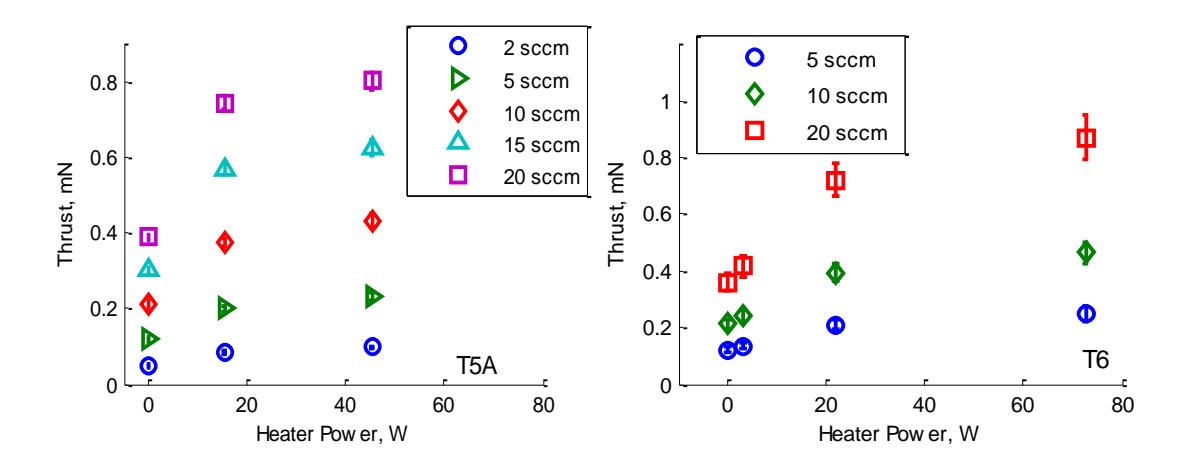


Figure 93 - Thrust vs applied power

The specific impulse is shown in Figure 94 and is in the range 39s-45s and 42s-51s for what concerns the T5A in resistojet mode at respectively 2A and 3A, whereas that of T6 HCT is in the range 21s-30s, 38s-44s and 45s-52s at respectively 1A, 2A and 3.3A. The specific impulse in cold gas mode is in the range 21s-25s for the T5A and 19s-27s for the T6 HCT.

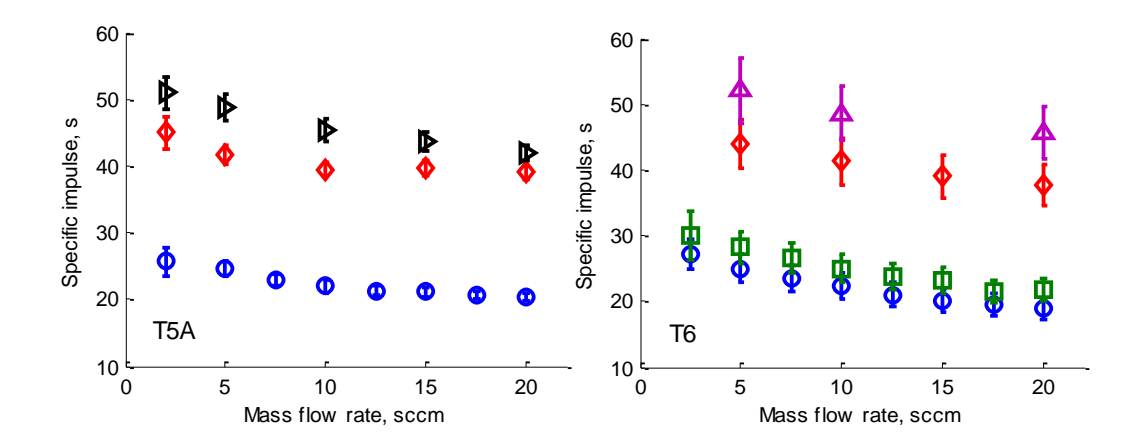


Figure 94 –Isp in cold gas and resistojet mode for the T5A and T6 HCTs

If it is assumed that the flow experiences an adiabatic expansion in the nozzle, the exhaust velocity u_{ex} can be found with a one-dimensional model as reported in [23]:

$$u_{ex} = \sqrt{2c_p(T - T_{in})} \tag{5.1}$$

where T_{in} is the inlet gas temperature and c_p is the specific heat at constant pressure. Since the Isp is known and with the assumption that the gas is at ambient temperature when entering the HCT, it is possible to calculate the mean temperature of the gas at the throat T in equation (5.1). For the T6 HCT it ranges from 162°C, when the Isp is 21.8s and the heater current 1A, to 840°C, at 52s and 3.3A. These values seem reasonable if considered that when the arc current is ignited the insert of the T6 HCT is at about 1000°C with the heater at 2.5A (47 W) [7]. With the same procedure it can be found that the gas temperature in the throat of the T5A HCT is in the range 480°C (39s, 2A) to 808°C (51s, 3A).

The thrust efficiency in resistojet mode is shown in Figure 95 and increases with the mass flow rate while decreases with the applied power. It should be noted that the thrust efficiency of the tested HCTs is always lower than 1.5% hence one order of magnitude lower than what found with xenon resistojets by other authors [27-29] and discussed in chapter I. The heater of the tested HCTs in fact were designed to raise the temperature of the insert to the desired ignition temperature (about 1100 degC) and not to efficiently heat the gas to use the device in resistojet mode. The flowing gas in the HCT used in resistojet mode is mainly heated by the surrounding

walls hence the flow is likely to have a radial temperature gradient with a considerably colder core.

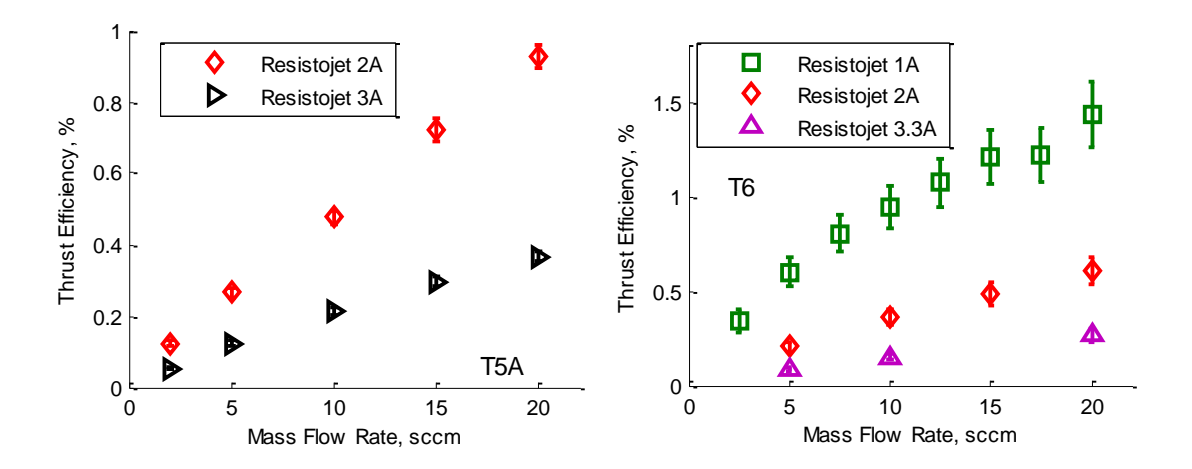


Figure 95 – Thrust efficiency in resistojet mode

V.3. **Discharge Characteristics**

V.3.1. **The T5 HCT**

The characteristic V-I curves were obtained for the T5 HCT in the two different configurations tested (T5K and T5A described in chapter IV) and are shown in Figure 96. The discharge voltage decreases when the mass flow rate is increased and reaches a plateau after a particular value of mass flow rate which increases with the current, as found already by other authors [7, 10]. The discharge voltage is in the range 13 to 15 V for the T5K and 18.2 to 25.5 V for the T5A, with the latter configuration showing higher voltages for the same set-point.

Looking for example at the cases of 2A and 2.5A and 2 to 6 sccm, the discharge voltage on the T5A is about 1.6 times higher than that of the T5K. This is probably due to the distance between the orifice tip and the anode/keeper: in the T5K this gap is 2.3mm, increased to 4mm in the T5A configuration.

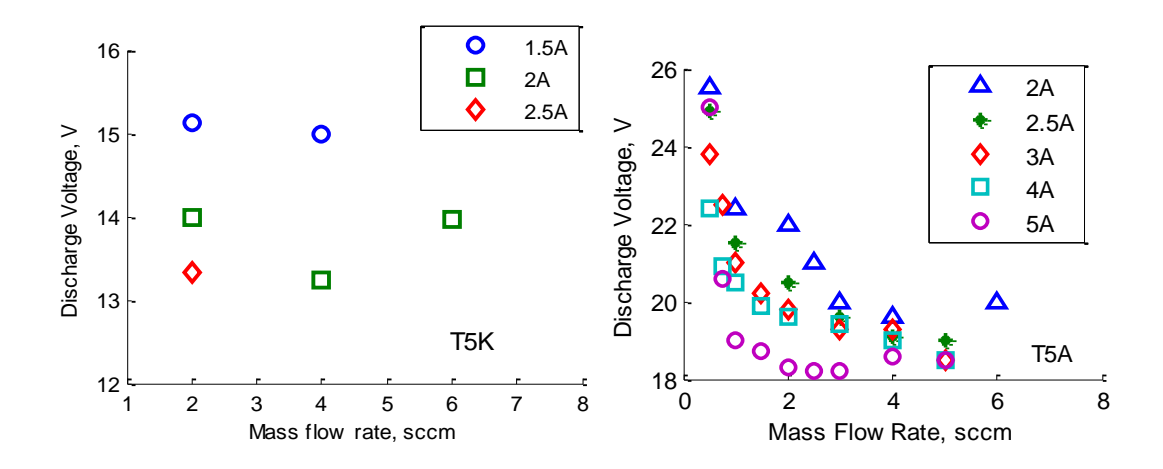


Figure 96 - Discharge characteristics on the T5K and T5 HCT

V.3.2. **The T6 HCT**

The characteristic V-I curves were obtained for the T6 HCT with and without the use of a 86 G external axial magnetic field in the orifice region and are shown in Figure 97. In both the cases the V-I curves show the same typical behaviour already discussed for the case of the T5 HCT in paragraph V.3.1. The discharge voltage decreases when the mass flow rate is increased and reaches a plateau after a particular value of mass flow rate which increases with the current, as found already by other authors [7, 10] and shown in Figure 97 to Figure 99. The discharge voltage is in the range 7 to 29 V. In the legend of the figures in this chapter the label '& B' means that the external magnetic field of 86 G was applied.

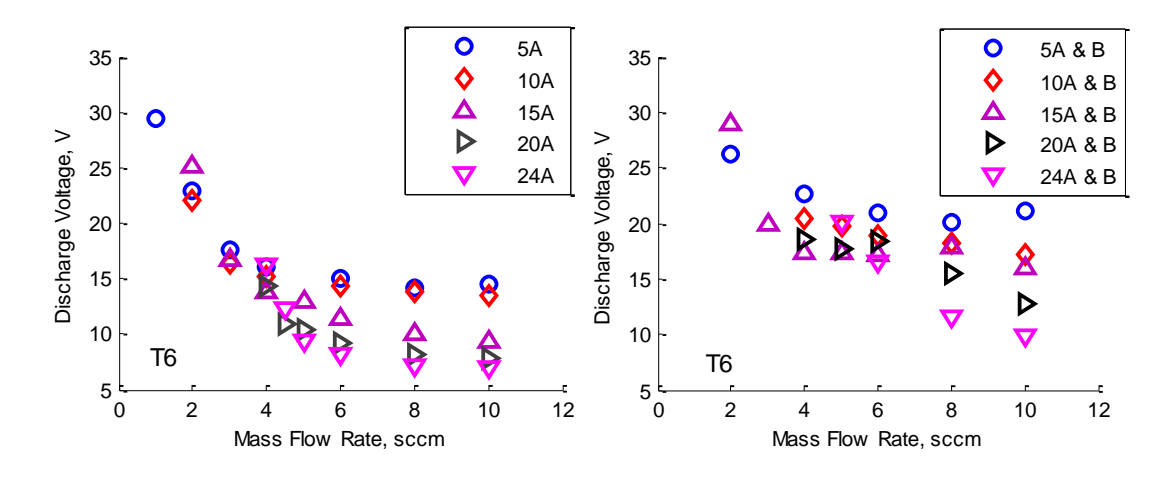


Figure 97 – Discharge characteristics on the T6 HCT

133

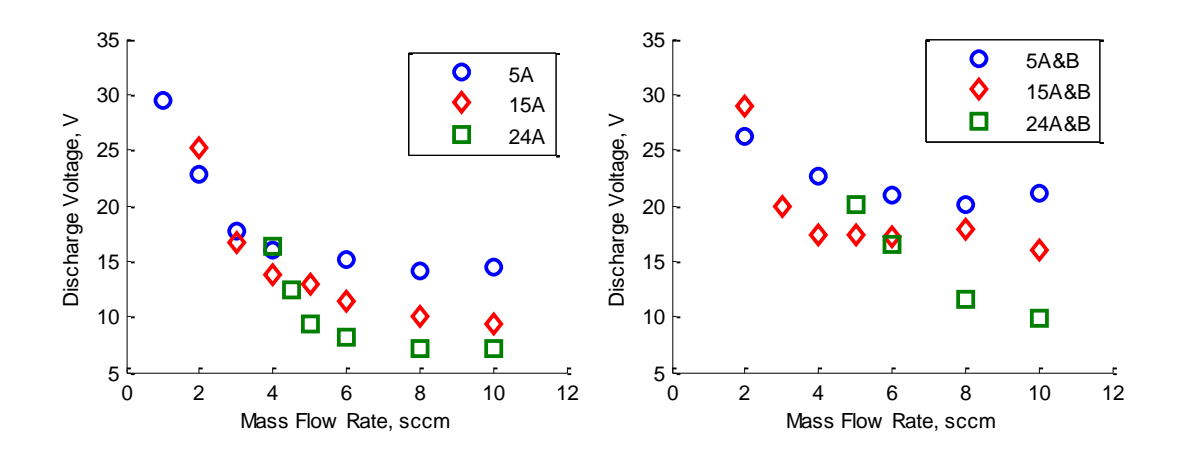


Figure 98 – Discharge characteristics on the T6 HCT – 5, 15 and 24 A only

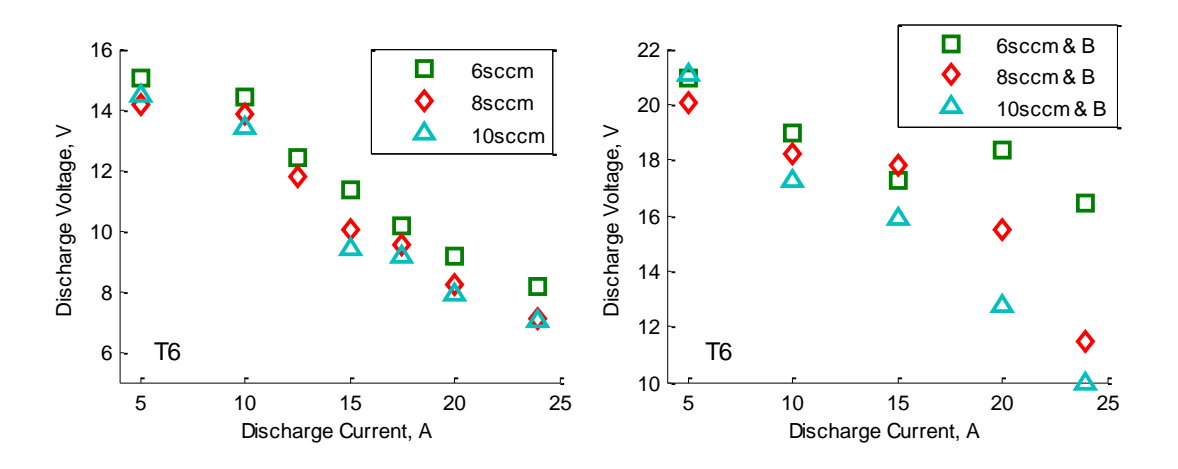


Figure 99 – Discharge characteristics vs mdot on the T6 HCT

The application of the magnetic field results in an increase of the discharge voltage, but this increase does not follow a unique trend for different discharge currents. This increase is in fact higher for higher mass flow rate for the case of 15A and for lower mass flow rates for the case of 24A as shown in Figure 100.

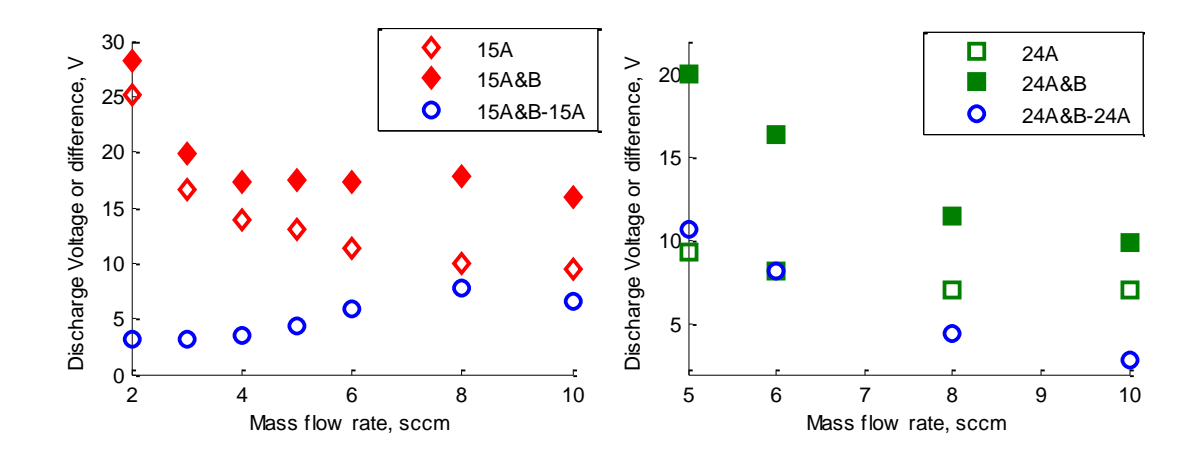


Figure 100 - Discharge characteristics at 15A and 24A on the T6 HCT at UoS

In Figure 101 and Figure 102 the discharge voltage is plotted against the specific energy E, defined as:

$$E = \frac{\left(VI_D + P_m\right)}{m} \tag{5.2}$$

where P_m is the power needed by the coil and I_D and V are respectively the discharge current and voltage, and \dot{m} is the mass flow rate. It should be noted how the discharge voltage decreases or increases almost linearly when the mass flow or the discharge current are respectively fixed. It should also be noted how the range of the specific energy is larger for the case of applied magnetic field: this is a consequence of the increase in discharge voltage and the additional power needed by the coil for the field generation.

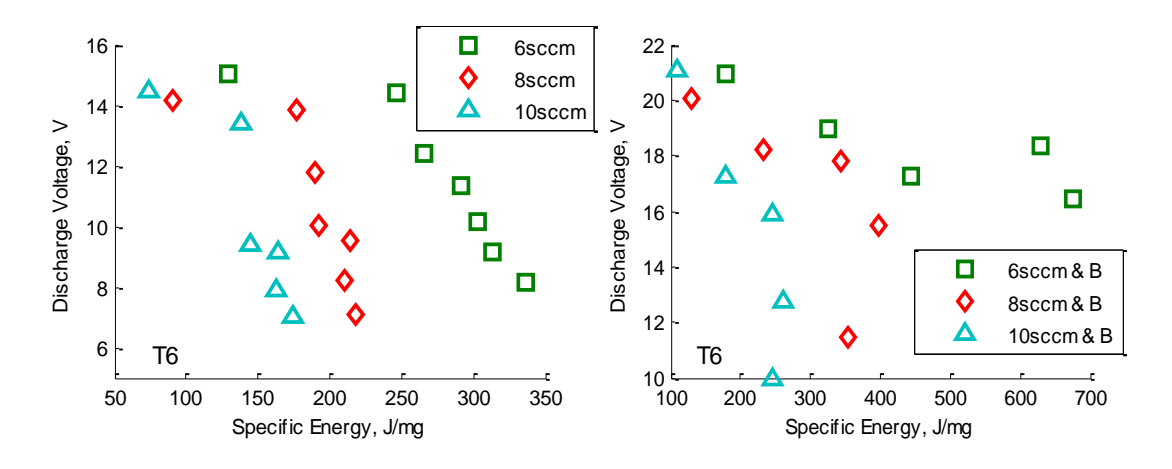


Figure 101 – Discharge characteristics vs E on the T6 HCT

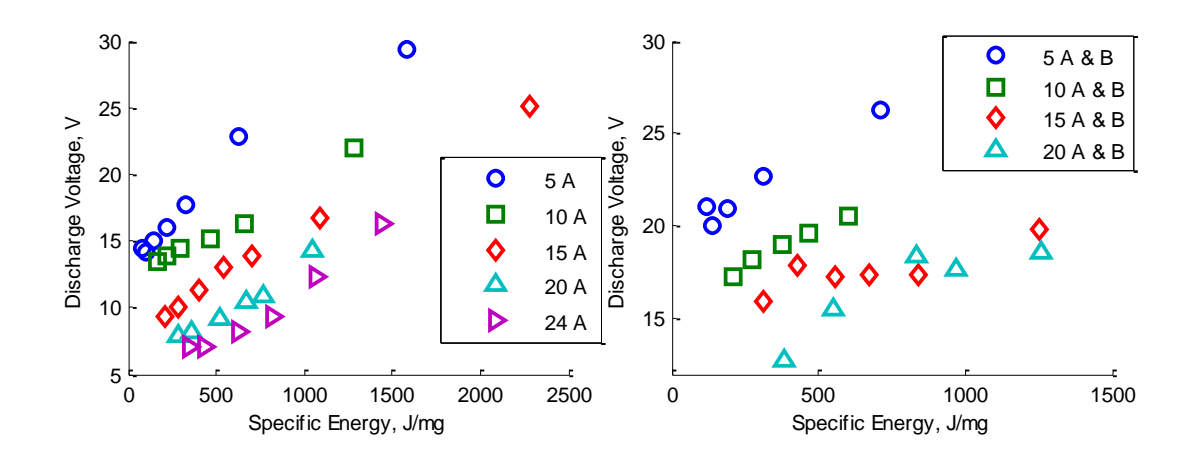


Figure 102 – Discharge characteristics vs E on the T6 HCT

An important consequence of the application of the magnetic field is the decrease in the noise level of the discharge voltage as it can be seen in Figure 103.

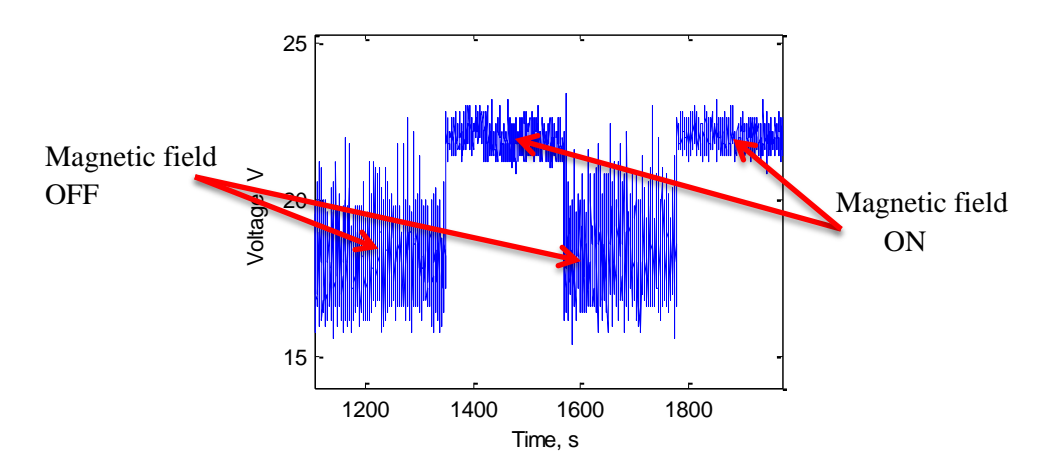


Figure 103 – Effect of the application and removal of the magnetic field on the discharge voltage at 15 A and 4 sccm on the T6

This effect was expected since the same behaviour was demonstrated in MPD thrusters in [106]. The reason for this lies within the fact that at relatively high discharge currents and low mass flow rates, the lack of charge carriers causes the anode sheath voltage to increase in order to collect more carriers. This is an unstable phenomenon leading to the discharge voltage noise seen in Figure 103. When the magnetic field is applied, the increase in voltage is probably due to the increase in the anode sheath voltage [106]. The increase in the anode sheath voltage allows in turn for the collection of more carriers hence the source of noise is decreased.

Figure 104 shows pictures of the T6 HCT at UoS for different set points: the anode/nozzle gets brighter when the current is increased and this may be an indication of an increase in temperature.

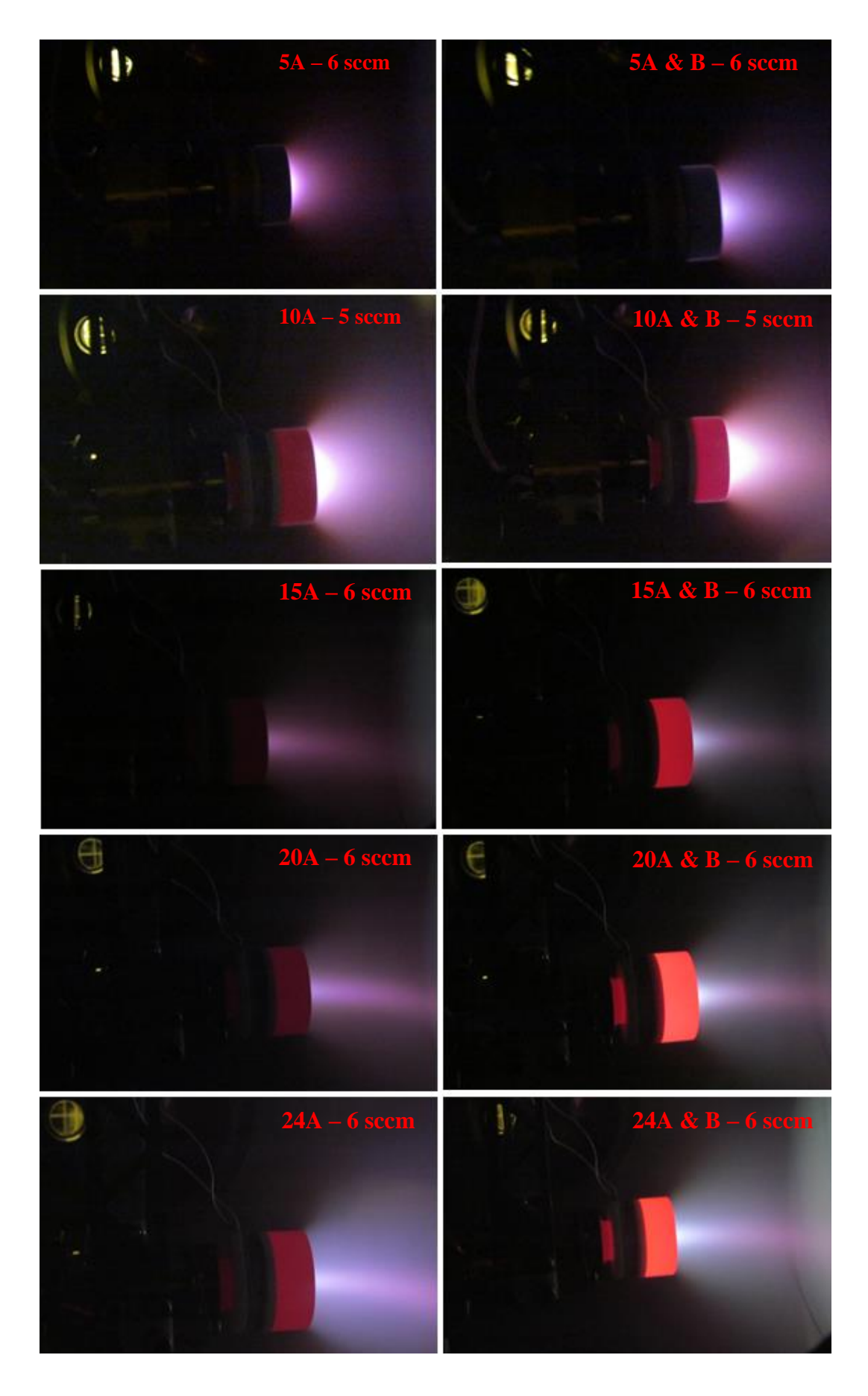


Figure 104 – Pictures of T6 HCT in discharge mode

V.4. **Discharge Thrust Measurements**

V.4.1. **T5K HCT**

Thrust measurements with the T5 in the keeper configuration (T5K) were obtained at Aerospazio Tecnologie with their direct thrust balance, discussed in chapter IV. These have been the first direct thrust measurements on a HCT available in the open literature. The gas used was xenon and the tested set-points are summarised in Table 26:

Table 26 - Thrust measurements set-points for the T5K

Т5К НСТ	Set-Points
1.5 A Discharge	2, 4 sccm
2 A Discharge	2, 4, 6 sccm
2.5 A Discharge	2 sccm

The obtained thrust is shown in Figure 105 with a comparison with the theoretical model. The thrust is in the range 0.2 to 0.7 mN and increases with the discharge current and the mass flow rate, with the specific impulse ranging 100 to 140s shown in Figure 106.

The predicted values are in a reasonable agreement with the experimental data, with the maximum difference being 14.5%. The model is then capable of catching the basic plasma process in the HCT. Using the predicted results it was possible to perform an assessment of the relative importance of the various thrust production mechanisms, shown in Figure 106, discussed in chapter II. The impulsive contribution to the thrust is always above 98% of the total. The heavy particles pressure contribution is always about 0.3% of the total, and the electromagnetic contribution decreasing with the mass flow rate from 1% to about 0.1%.

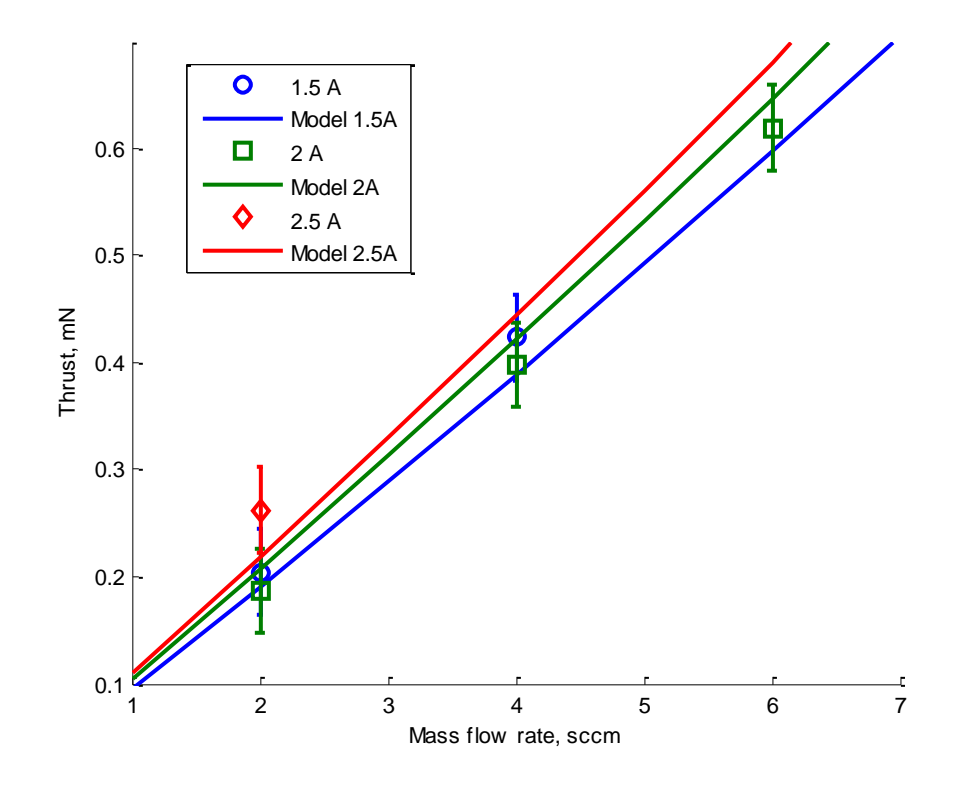


Figure 105 – Thrust vs mass flow rate on the T5K HCT

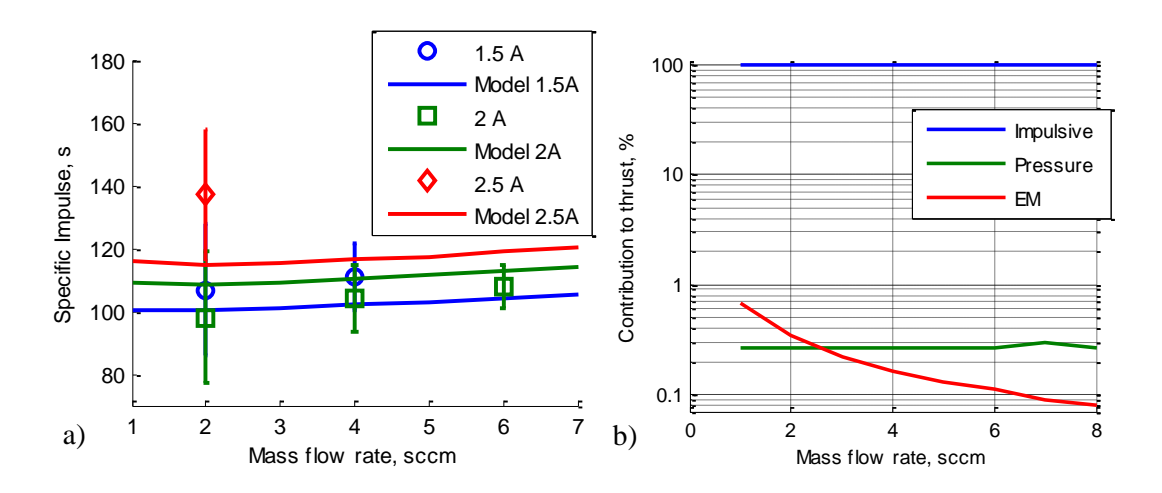


Figure 106 – a) Isp vs. mass flow rate and b) contribution to the thrust on the T5K

The thrust efficiency is shown in Figure 107 and is in the range 0.3 to 1.2%. It can be seen that the thrust efficiency increases with the mass flow rate.

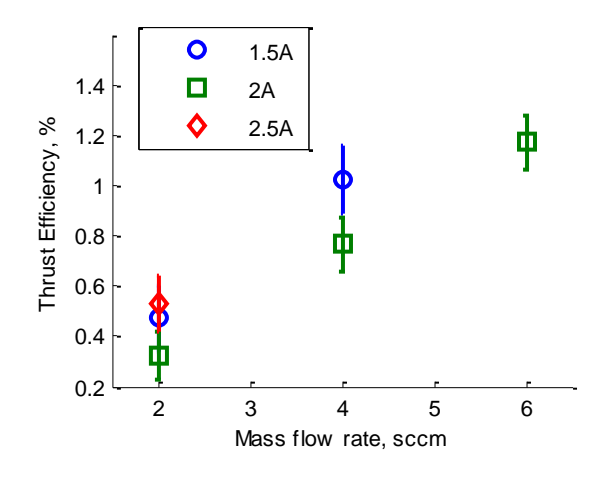


Figure 107 – Thrust efficiency of the T5 HCT

V.4.2. **T6 HCT**

Thrust measurements with the optimized T6 HCT were obtained at the University of Southampton with the direct thrust balanced described in chapter IV and partially replicated at Aerospazio Tecnologie with their direct thrust balance. The comparison between the results from the two different thrust balance were discussed in chapter IV, and in this paragraph only the test at the UoS will be shown. The gas used was xenon and the tested set-points are summarised in Table 27:

Table 27 - Thrust measurements set-points for the T6 HCT

Т6 НСТ	Set-Points at B=0	Set-Points at B=86G
10 A Discharge	3, 4, 6, 8, 10 sccm	4, 6, 8, 10 sccm
15 A Discharge	4, 5, 6, 8, 10 sccm	4, 5, 6, 8, 10 sccm
20 A Discharge	5, 6, 8, 10 sccm	6, 8, 10 sccm
24 A Discharge	4.5, 5, 6, 8, 10 sccm	

Thrust data with discharge currents of 10, 15 and 20 A were obtained also applying a magnetic field of 86 G in the orifice region.

V.4.2.1. Thrust and Specific Impulse

It is important to stress once again that the T6 HCT here presented is the first HCT with a geometry optimized to reach high performance with a theoretical tool. The

measured thrust in discharge mode is in the range 0.63mN to 2.61mN for the case of no magnetic field, shown in Figure 108, and 0.88mN-2.65mN with the applied magnetic field, shown in Figure 109. The thrust increases linearly with the mass flow rate in both the cases. The linear dependency between the thrust and the mass flow rate with no magnetic field applied had been already identified in [3, 4, 7, 10] with the use of indirect thrust balances.

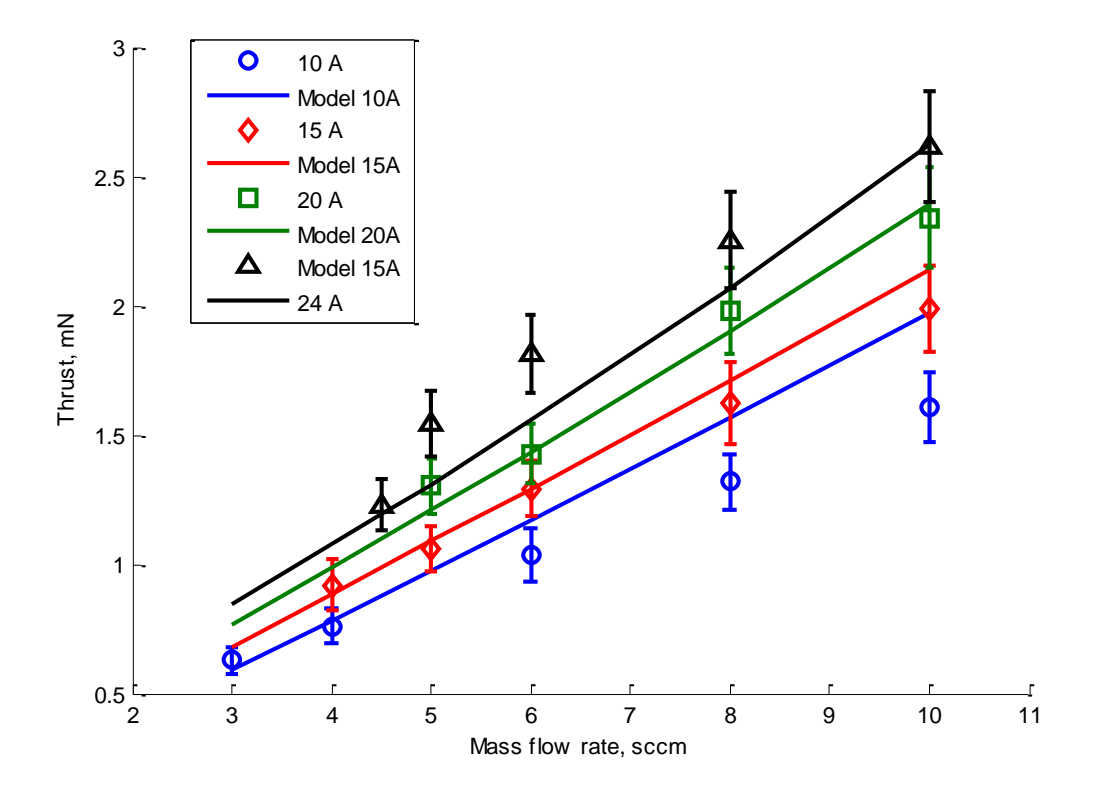


Figure 108 – Overall view of the thrust obtained with no applied magnetic field

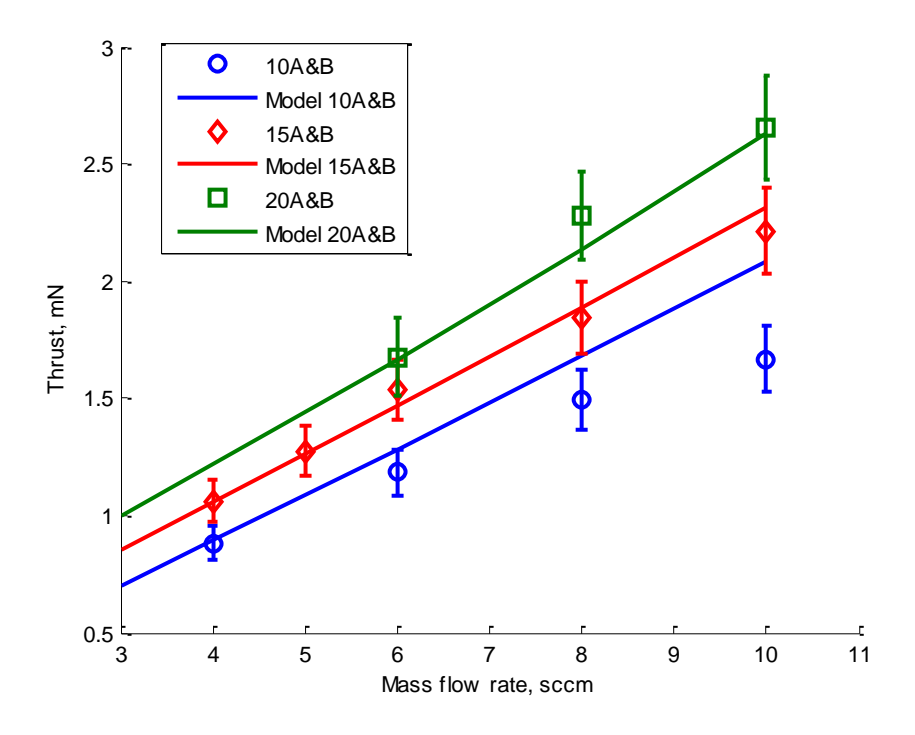


Figure 109 - Overall view of the thrust obtained with applied magnetic field

The predictions of the theoretical model are in reasonable agreement for values of the discharge current of 15, 20 and 24 A showing a maximum error of 11.5%. At 10 A the predicted values overestimate the thrust giving a maximum error of 15.6%, as shown in Figure 108. Same results for the predictions of the theoretical model with the applied magnetic field: the computed thrust is in very good agreement with the measured thrust for discharge currents of 15 and 20 A, whereas at 10 A the predicted thrust overestimates the computed one, as shown in Figure 109. Once again the model seems well capable of catching the physical processes in the HCT. The impulsive part of the heavy particles gasdynamic thrust is the highest contribution, being always higher than 85%. The pressure part is instead always about 0.01%, meaning that the nozzle is capable of fully expanding the hot gas. The electromagnetic contribution increases with the discharge current, and this was expected since it is the result of the *jxB* effect. It is useful to remember that the electromagnetic thrust is a constant value, hence its percentage contribution to the total thrust decreases with the mass flow rate.

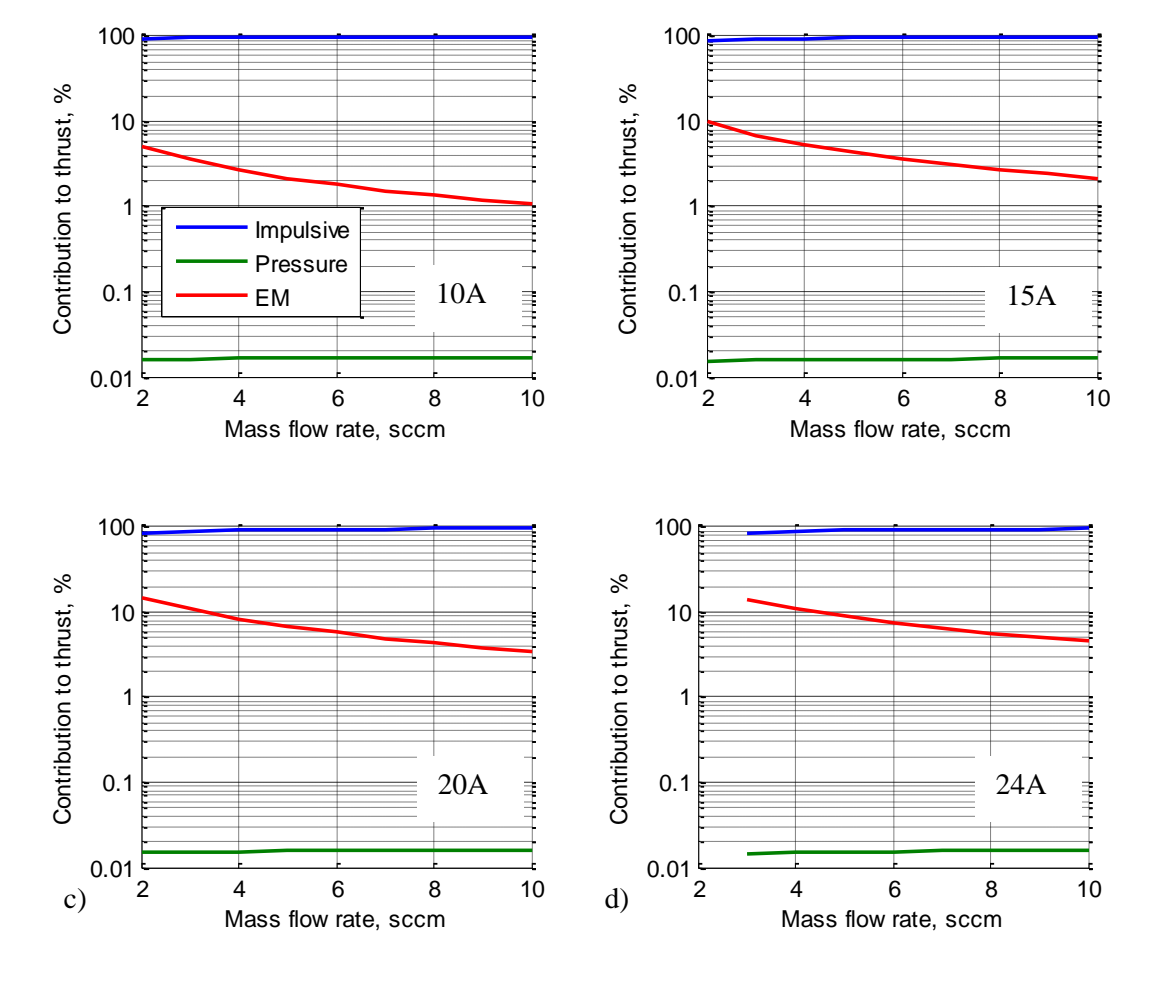


Figure 110 -Contribution to the thrust for the T6 HCT with no applied B

The specific impulse is shown in Figure 111: it is in the range 168s-323s and 175s-298s for the case of no magnetic field and applied magnetic field respectively and increases when the mass flow rate decreases. Compared to the *Isp* obtained by Gessini [1, 3, 4] with the T6 with an orifice diameter of respectively 1mm and 0.5mm and by Grubisic [7], with a T6 with an orifice diameter of 1 mm, the *Isp* obtained for the same set-point with this optimized T6, which has a narrower and longer orifice, is about 180%, 30% and 300% higher respectively. It should also be noted that in [1, 3, 4, 7] thrust measurement were obtained with indirect thrust balance, which may overestimate the thrust as discussed in chapter II, were used hence the difference may be even higher.

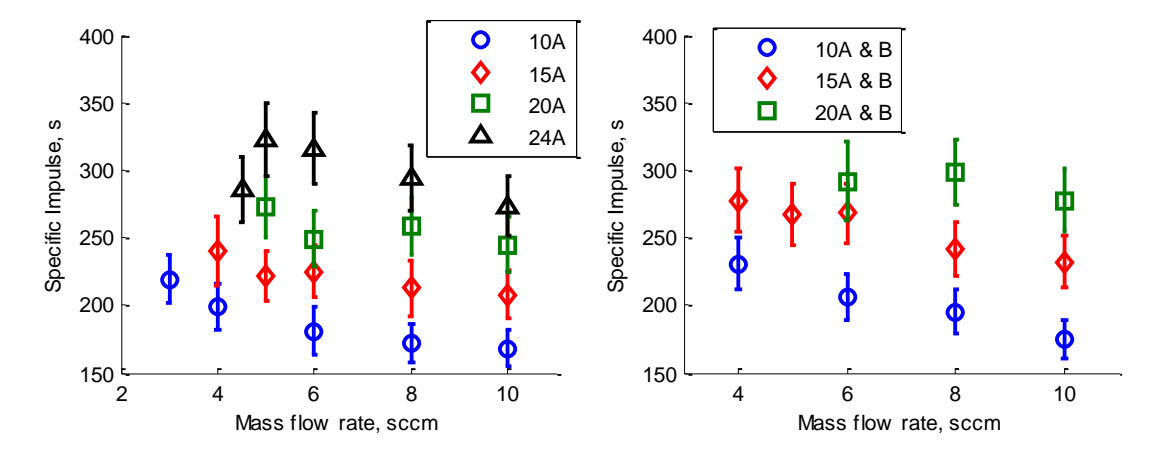
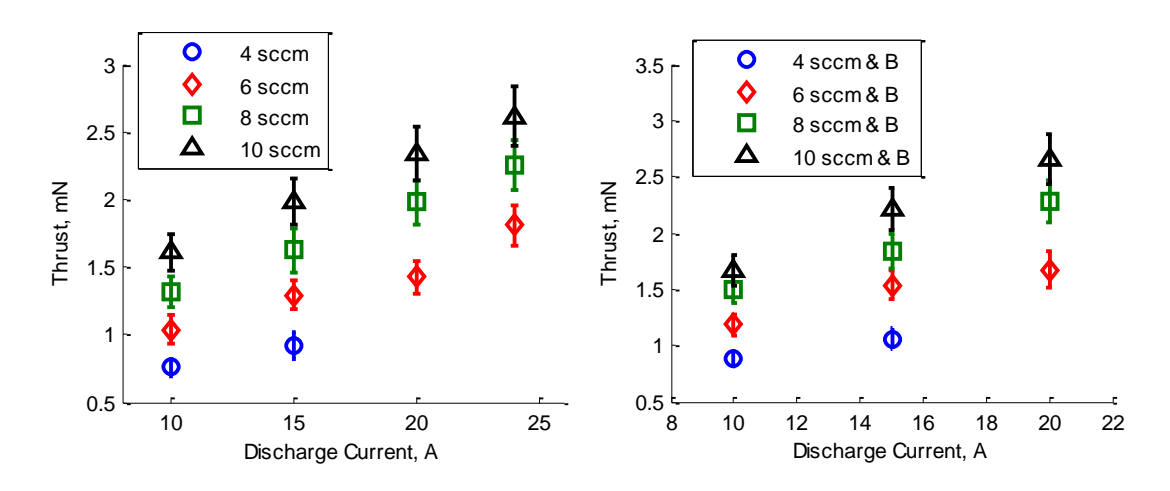


Figure 111 – Overall view of the Isp obtained

As shown in Figure 112 and Figure 113 the thrust and *Isp* increase linearly with the discharge current in both the cases of applied and unapplied magnetic field. In chapter II the thrust production mechanisms have been discussed. The main mechanism that contributes to the production of the thrust has been shown by the theoretical model to be the impulsive part of the heavy particles gasdynamic contribution, hence the expansion of the hot propellant in the anode/nozzle. In the HCTs heavy particles collisions with energetic electrons [61, 88] and charge exchange collisions raise the temperature of the propellant in the insert and especially in the orifice region where the particle density is the highest. The other contribution was shown to be the electromagnetic force, which gave a maximum contribution to the thrust of 80 μ N at 24A (11% of the thrust at 24A and 5sccm). The HCTs main thrust production mechanism seems to be the arcjet-like operation mode, and this is supported by the linear dependency between the thrust and the discharge current, shown in Figure 112.



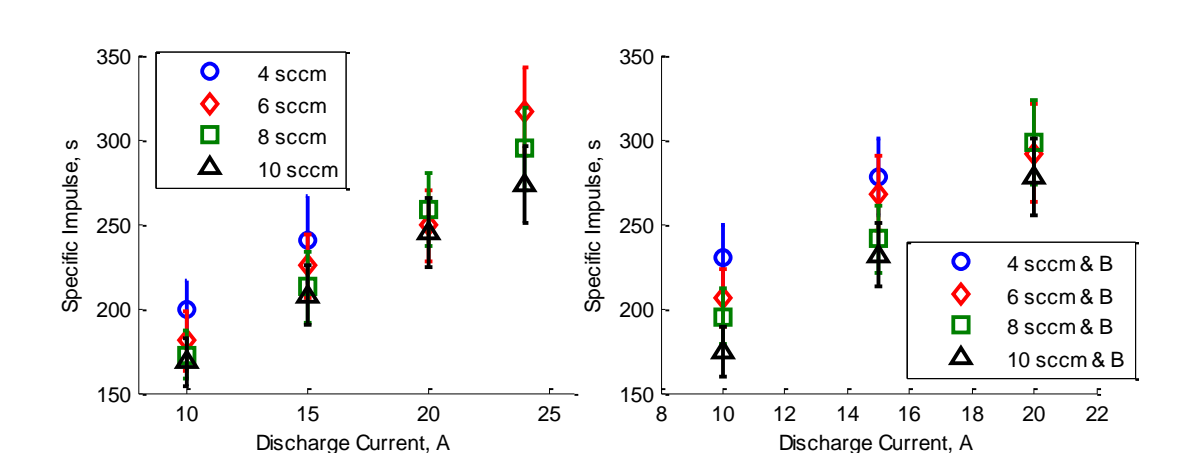


Figure 112 – Thrust plotted against the discharge current

Figure 113 – Isp plotted against the discharge current

In Figure 114 the thrust is plotted against the specific energy, defined in equation (5.2). The thrust decreases, for a fixed current, and increases, for a fixed mass flow rate, almost linearly when the specific energy increases for both the cases of applied and no applied magnetic field. These behaviours were expected: in fact, for a fixed current, a decrease in mass flow rate leads to a higher V and lower thrust while E increases as discussed in equation (5.2). This behaviour was seen already in [7, 10, 12] with no magnetic field applied. Following the same way of thinking, the thrust was expected to increase with E for a fixed mass flow rate.

The *Isp* instead increases linearly with the specific energy for lower discharge currents and has instead a maximum at 24 A for the case of no applied magnetic field as shown in Figure 115 for a fixed current. In the case of a fixed mass flow rate, the *Isp* increases almost linearly with the specific energy. As discussed for the case of the thrust, it can be proved how the behaviour of the specific impulse versus the specific energy followed what expected.

It should be noted that the range of the specific energy in the case of applied magnetic field is much larger since the energy spent in generating the magnetic field is included in equation (5.2).

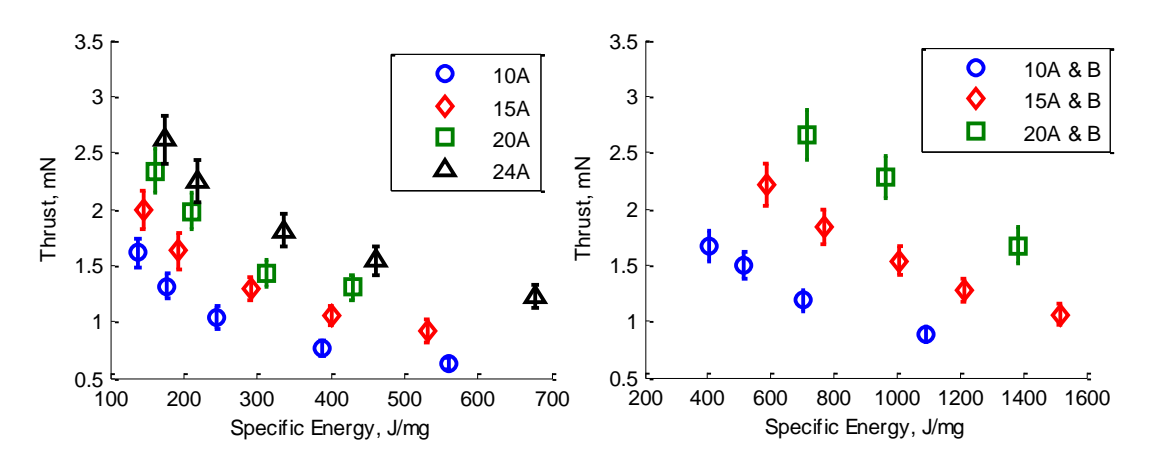


Figure 114 – Overall view of the thrust vs. specific energy obtained

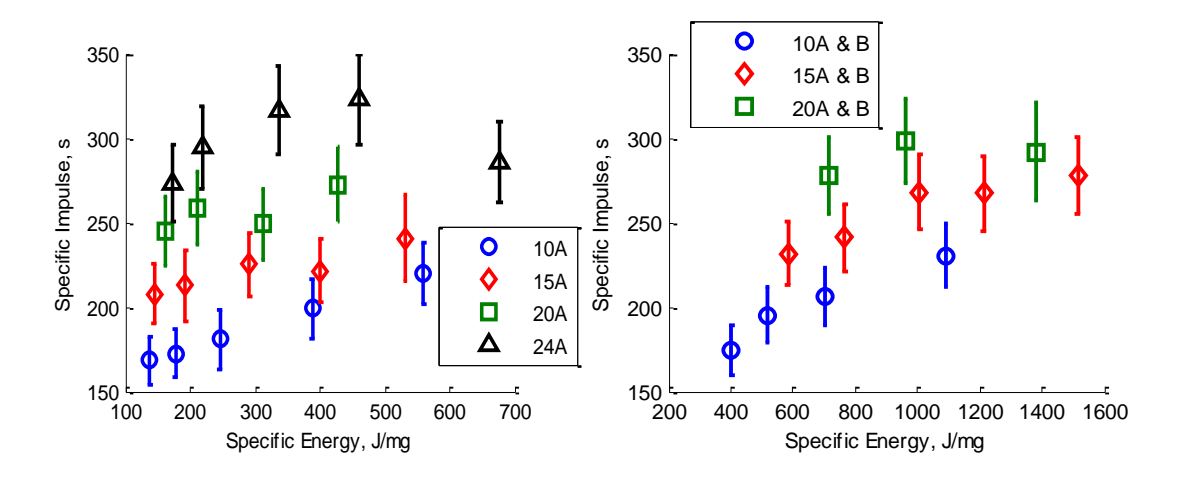


Figure 115 – Overall view of the Isp vs. specific energy obtained

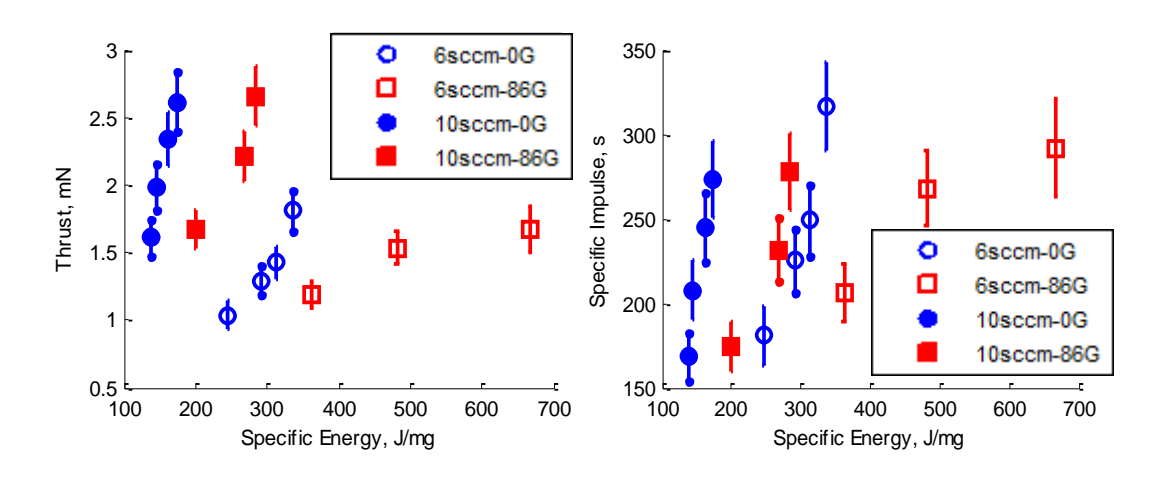


Figure 116 – Example of thrust and specific impulse vs. E for a fixed mass flow rate

When the magnetic field is applied, the increase in thrust is about 15% and this does not depend dramatically on the mass flow rate, as show in Figure 117. The *Isp* shows instead a linear increase with the discharge current when the magnetic field is

applied. In Figure 117 the increase in thrust are compared with the theoretical predictions obtained with the theoretical model developed for MPD thrusters [69]. The model described in [69] predicts only the increase in the electromagnetic thrust and does not simulate the changes in the thrusters behaviour which the magnetic field may take. The agreement of the predicted values with the experimental ones is satisfactory: the HCT behaves like a low power MPD thruster when the external magnetic field is applied.

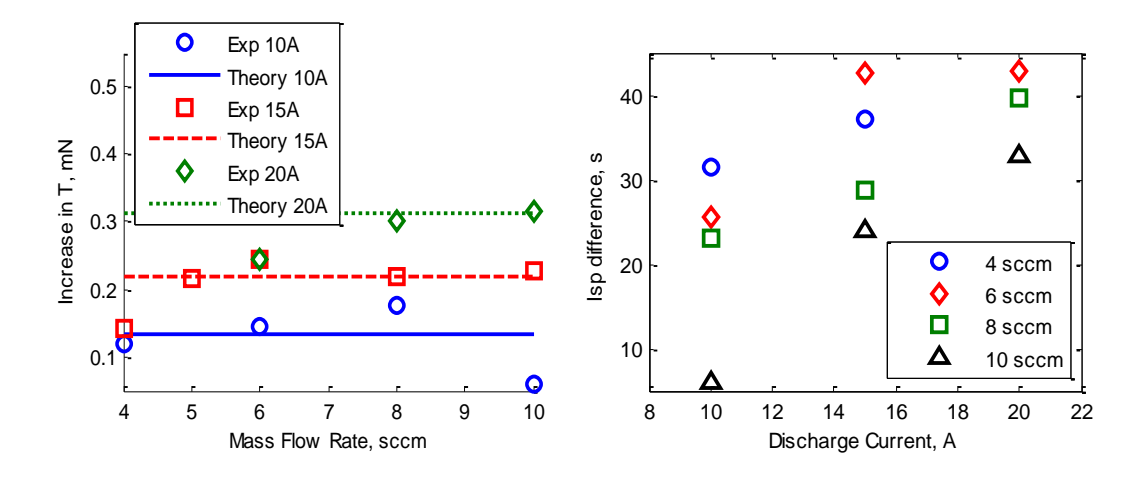


Figure 117 – Increase in thrust and Isp with the applied magnetic field

V.4.2.2. Thrust Efficiency

The efficiency of the thruster was derived from the thrust and the total power as shown in equation (5.3):

$$\eta = \frac{F^2}{2m(VI_D + P_m)}$$
(5.3)

where V and I_D are respectively the discharge voltage and current and P_m is the power needed by the coil.

The thrust efficiency is in the range 0.5% to 2% and 0.43% to 1.30% for the case of no magnetic field and applied magnetic field respectively. As shown in Figure 118 and Figure 119 it increases linearly with the mass flow rates and the discharge current in both cases. It should be noted that the thrust efficiency is lower in the case of applied magnetic field because of the additional amount of power required by the coil as shown in equation (5.3). As discussed already in chapter I, it can be shown

that the thrust efficiency obtained in the previous measurements, using the data in [2, 7, 10], was in the range 0.06% to 0.27% at 25A hence about 10 times lower than what obtained with this optimized T6 HCT. The main reason for the enhanced performance lies in the longer and narrower orifice, likely to produce hotter plasma with higher particle number densities.

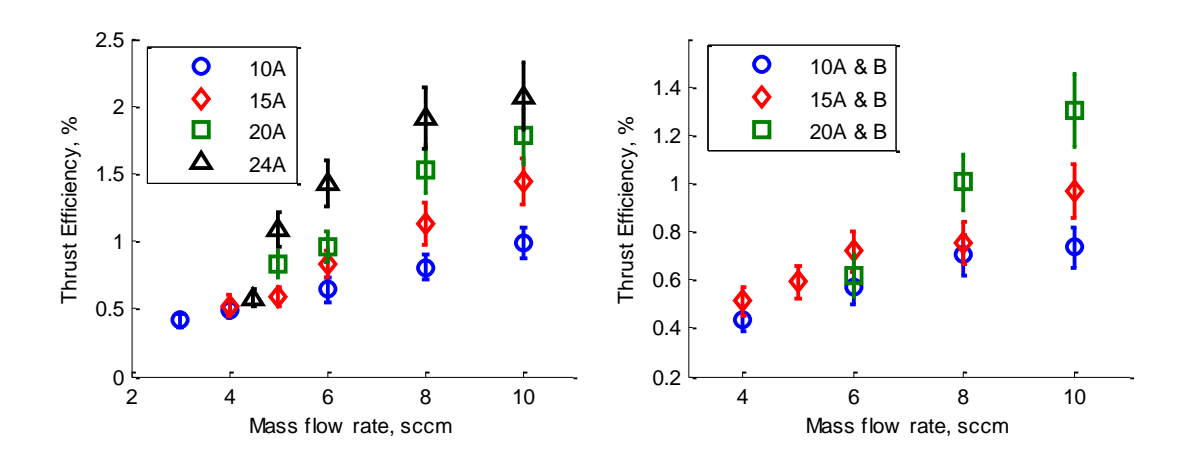


Figure 118 – Thrust efficiency vs mass flow rate on the T6 HCT

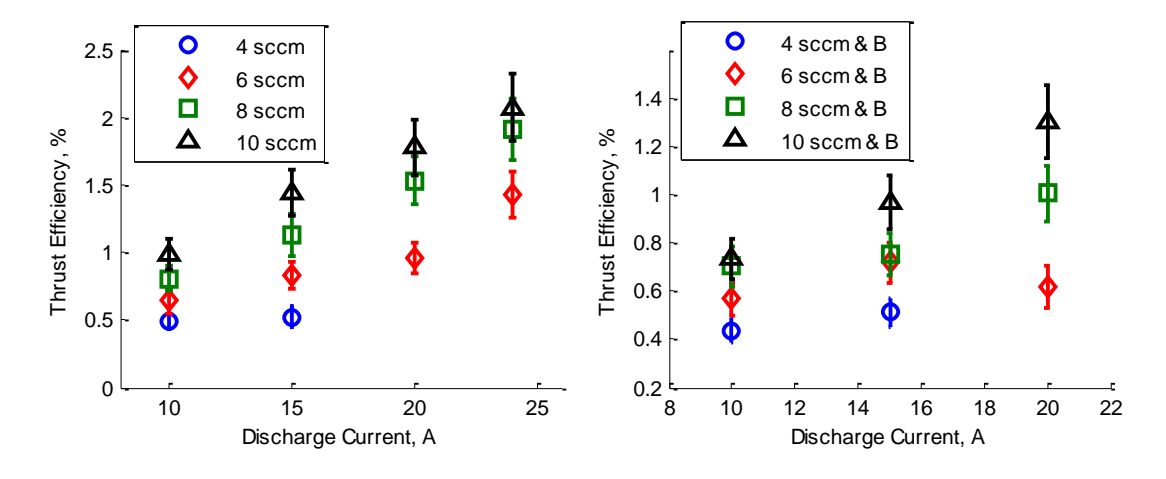


Figure 119 – Thrust efficiency vs discharge current on the T6 HCT

The thrust efficiency decreases when the specific energy increases as shown in Figure 120. The reason for this lies within the fact that when the mass flow rate is decreased there is an increase in the discharge voltage, leading to a higher power available per mass flow unit (specific energy) as per equation (5.2); in the meantime the decrease in thrust leads to an overall decrease in the thrust efficiency as per equation (5.3).

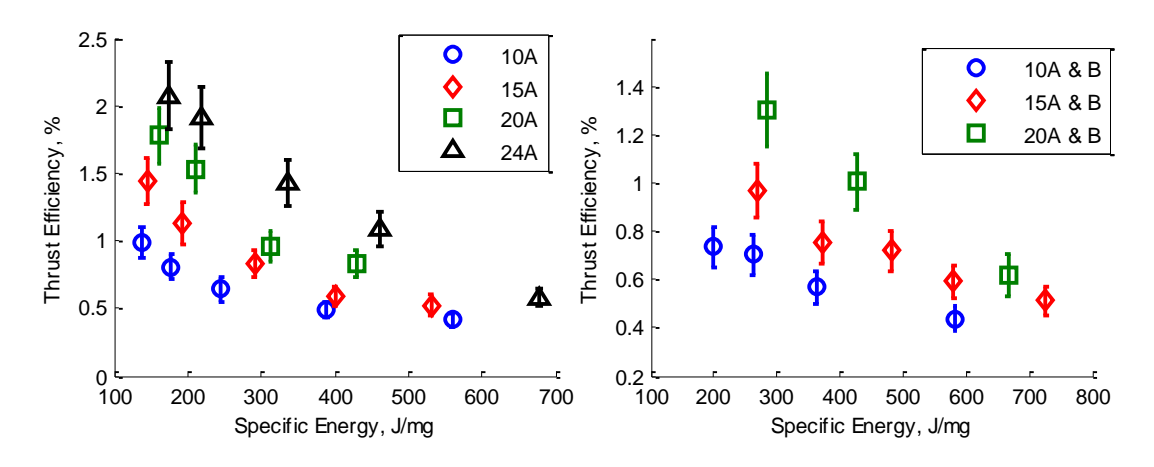


Figure 120 – Thrust efficiency vs specific energy on the T6 HCT at UoS

V.5. Comparison with the requirements

In chapter I a series of requirements derived from [32] to replace chemical thrusters with electric propulsion systems onboard communication satellites were shown. Starting from the requirements for the cold gas mode (25mN of thrust at 30s of *Isp*), with the T6 HCT thrust up to 0.369 mN was measured. The data obtained were linearly fitted to extrapolate the mass flow rate needed to have 25 mN of thrust. A xenon rate of 1105 sccm would be needed to get 25 mN, with a calculated *Isp* of 23.7 s. The requirement for the *Isp* in the cold gas mode would not be achieved. In discharge mode a thrust up to 1.3 mN with an *Isp* of 273s was obtained at 20 A and 5 sccm without the magnetic field, exceeding the requirements. The effect of the magnetic field is that of reducing the level of noise on the discharge voltage, even though the discharge voltage itself increases, and that of increasing the thrust by 10% to 20%.

The HCT also showed a quick start (<10 minutes) with low voltage (~30 V) when heated with one heater at 3.3 A. The single HCT is <350g with the magnetic coil; 12 HCTs would be <4.2kg hence about 7.8kg would remain to complete the system (FCUs, etc.) hence to be compliant in the system mass requirement.

A compliancy matrix shows the requirements and the measured performance:

Table 28. Comparison of experimental data with requirements

		Measured at		
Parameter	Requirement	20A, 5sccm, B=0G	15A, 6sccm, B=86G	Compli ant
System mass (12 thrusters)	< 11 kg	1 HCT < 350 g		
Power per thruster	< 500 W	210 W	281 W	Yes
Isp	> 250 s	273 s	268 s	Yes
Thrust	> 0.6 mN	1.3 mN	1.54 mN	Yes
Isp in cold gas mode	> 30 s	23.7 s (derived)		No
Thrust in cold gas mode	> 25 mN	At 1105 sccm (derived)		Yes

V.6. **Erosion**

At the end of the tests the T5 and T6 HCTs were inspected to check for signs of erosions. The orifice measurements were taken along the orifice axis on two perpendicular planes using a Vision Engineering's Hawk Duo CNC [107] measuring optical microscope hosted at QinetiQ. This microscope uses image focusing to calculate the distance on three axes. Two sets of measurements were made for each cathode, and they are in good agreement with each other, being the largest difference of the order of 5%.

For what concern the T5 HCT, it was run in the discharge mode for about 60 hours in two different configurations (T5K and T5A) in a wide range of discharge currents (1 to 5 A) and with discharge voltages sometimes exceeding 35 V. The orifice, which was 1 mm long fully straight with a diameter of 0.22mm, presents now a chamfered part 0.6mm long with a semi-angle of 30 degrees as shown in Figure 121.

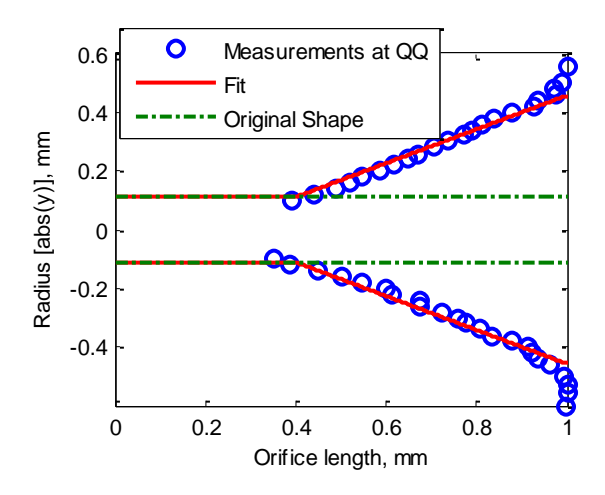


Figure 121 - Orifice new shape measured with the microscope

The chamfered orifice can also be seen at naked eye, as shown in Figure 122.

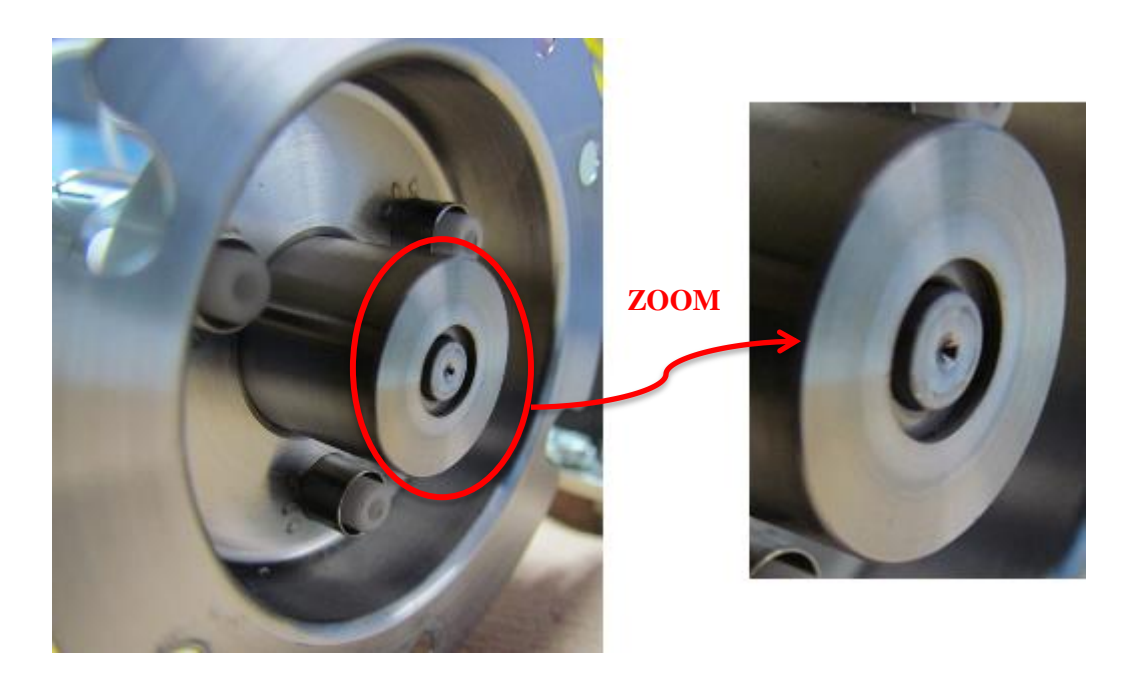


Figure 122 - Orifice visual inspection

From Figure 123 is then possible to notice the erosion of the orifice. The cathode orifice at the cathode beginning of life is shown in Figure 123-a), whereas the orifice at the end of the test is shown in Figure 123-b).

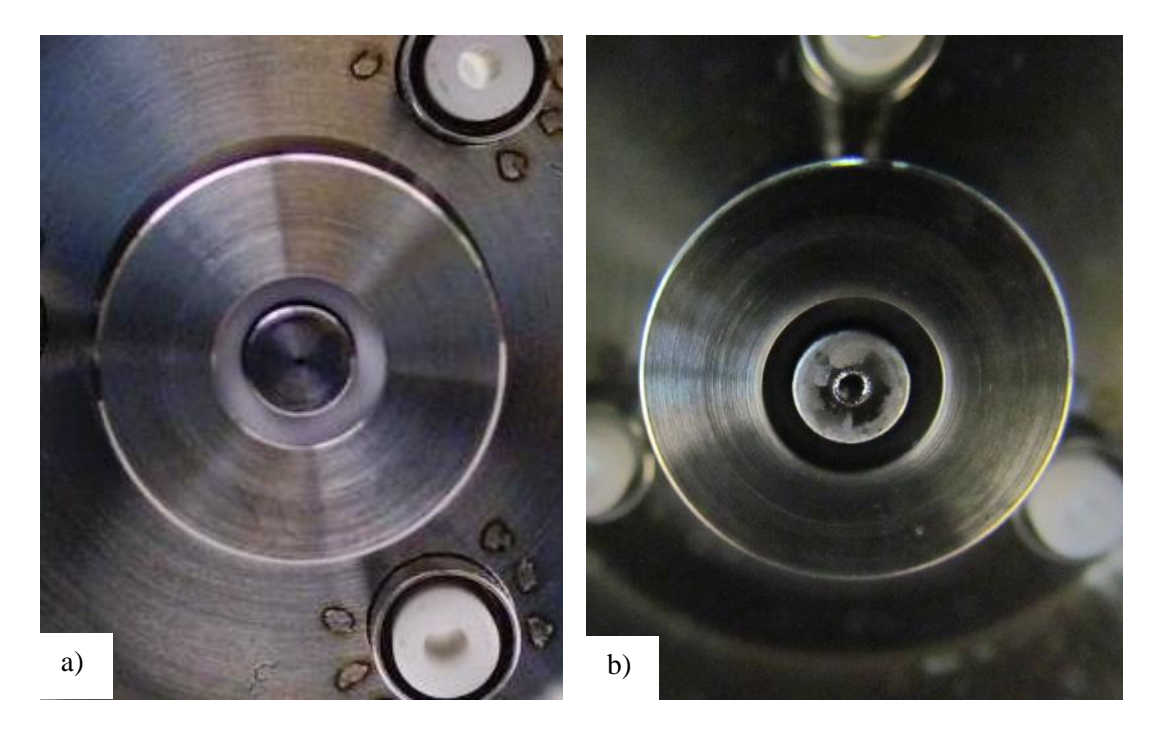


Figure 123 - The orifice a) as given by QQ and b) after the test at Aerospazio

Regarding the optimized T6 HCT, after the test campaign at AER and UoS it had accumulated more than 300h working in the discharge mode, with a wide range of discharge currents (5 to 24A) and discharge voltages sometimes exceeding 40V. From the microscope measurements, shown in Figure 124, it is possible to see that the new orifice geometry presents a straight part only 0.1mm long at the nominal diameter.

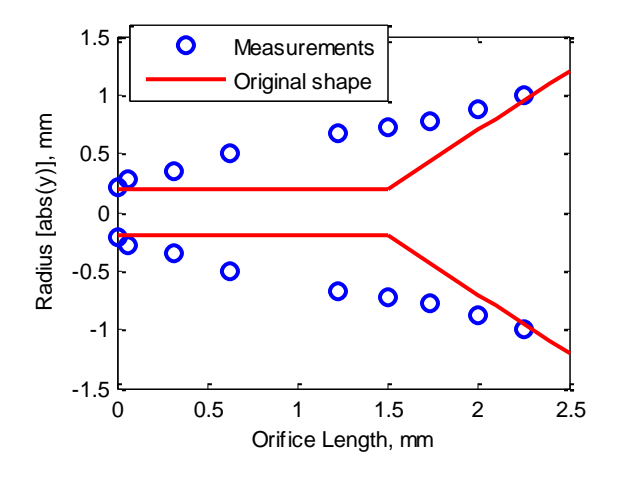


Figure 124 – New orifice geometry

The orifice tip is shown in Figure 125, whereas in Figure 126 the images from the microscope are shown from the orifice tip base (100% deep) to the external surface (0% deep)



Figure 125 – The orifice tip

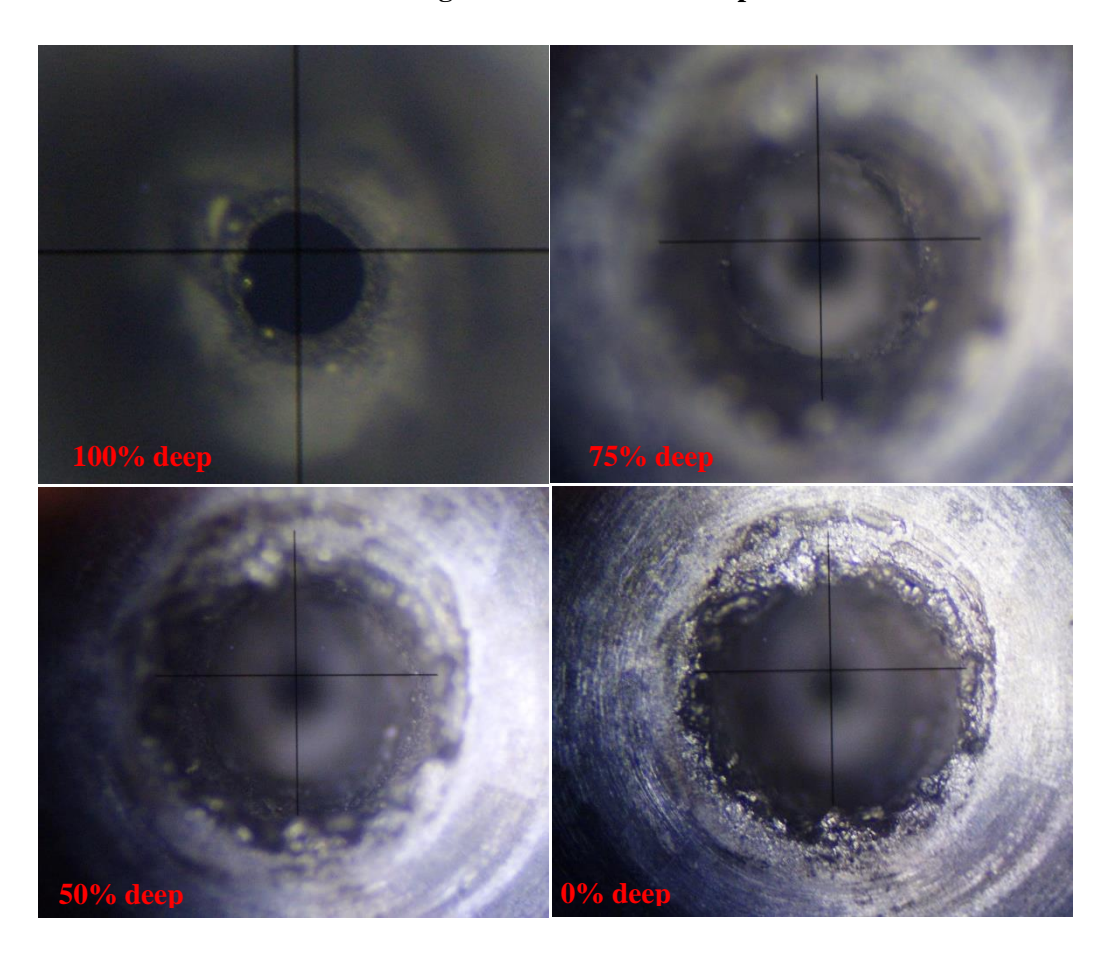


Figure 126 – T6 HCT orifice visual inspection with the microscope

The erosion of the T6 HCT orifice was probably caused by the wide range of setpoints often leading to high voltage in excess of 40V, and to the shape of the orifice, narrower and longer than the standard T6 HC hence likely to produce higher plasma density and ion fluxes to the wall.

The T6 HCT was also disassembled and all the components were visually inspected. Figure 127 show the enclosed keeper: there is no sign of erosion on the internal wall of the divergent part of the nozzle or on the internal upstream part of the nozzle, where a small deposition of white material, probably Boron Nitride coming from the spacer.



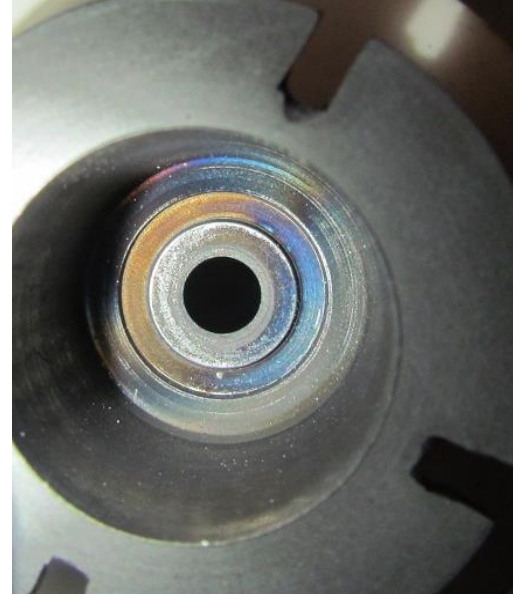


Figure 127 – The anode/nozzle

The spacer, shown in Figure 128, looks in very good conditions: no signs of erosion are visible at naked eye. Only the upstream part, directly connected with the orifice tip, and the internal wall of the divergent part, present a black surface, probably due to the high temperature in that region.





Figure 128 – The spacer

Chapter VI

Conclusions

This research has produced the first theoretical tool specifically developed for the prediction of the performance of hollow cathode thrusters (HCTs), and collected the experimental data needed for its validation hence demonstrating the validity of the model as a designing tool. The development of such a model is essential to reduce the long and expensive experimental tests needed to experimentally optimize HCTs performance. The thrust measurements shown within this research are the first obtained with a direct thrust balance and were carried out to make a comparison with the predictions of the model. Consequently, a better understanding of the physical processes contributing to the generation of the thrust and of the performance that HCTs are able to reach have been gained after this work. This chapter summarises the main conclusions drawn from this research.

VI.1. Theoretical Model and Mechanisms of Thrust Production

The theoretical model presented within this work is the first one specifically developed to predict performance of hollow cathode thrusters in terms of thrust, *Isp* and power consumption with reasonable accuracy, simplicity and low computational cost. The model consists of three sub-models to simulate the plasma inside the three main HCTs regions: a 0D model for the insert developed at JPL [35], a 1D model for the orifice region developed within this research and a classical model for the 1D adiabatic gasdynamic expansion of the gas in the nozzle.

The model for the orifice, specifically developed within this research, is a 2-fluid model where the electrons and the heavy particles (ions and neutrals) are treated separately. The main assumptions consist in the quasi-neutrality of the plasma, in the thermal equilibrium of the heavy particles that also have the same group velocity,

sonic conditions for the heavy particles at the orifice throat and a constant electron Mach number. Algebraic and fluid differential equations are implemented together in the model, with the latter including in the source terms all the main physical processes characterizing the plasma behaviour. The source terms include ionization, particles losses to the walls, elastic collisions, heat conduction and the presence of an electric field.

The results from the model in terms of plasma parameters (electron and neutral densities and electron temperature) and voltage drop in the orifice are in reasonable agreement with the experimental results obtained for the NSTAR cathode at two different set-points. The predictions in terms of thrust and *Isp* have the expected trends when the geometry or the set point is changed while the discharge voltage does not follow the expected trend. The reason for is most likely due to the fact that the model does not calculate the orifice sheath voltage, which may be significant, or any voltage drop in the anode region.

The predicted values in terms of thrust and *Isp* are in good quantitative agreement with the direct thrust measurements carried out within this research. For the T5K (with its original keeper electrode in front of the orifice tip), the maximum difference between the measured and predicted values was 14.5%. For the optimised T6 HCT, for values of the discharge current of 15, 20 and 24 A the maximum error is 11.5%, whereas at 10 A the predicted values overestimate the thrust giving a maximum error of 15.6%. Hence, the model is capable of predicting the thrust and specific impulse of HCTs with reasonable accuracy, showing that the basic plasma processes are well described by the equations implemented in the model and that the processes contributing to the generation of the thrust are understood.

Prior to starting the plasma modelling inside HCTs, a significant effort was made to identify which physical processes might contribute to the generation of the thrust. Following the work started by Gessini and Grubisic [6, 12, 13], four main mechanisms were identified as potential contribution to the thrust:

- heavy particles gasdynamic acceleration
- electrons gasdynamic acceleration
- electromagnetic acceleration

high energy ions production.

The heavy particles gasdynamic acceleration is relative to the ions and neutrals exit velocity and pressure and has been identified as the highest contribution. The other main process contributing to the thrust is the electromagnetic (jxB) acceleration. The electrons gasdynamic process and the contribution from high energy ions might take part in the generation of the thrust, but their contribution is negligible being orders of magnitude lower than the others.

With the model predictions, it was possible to perform an assessment of the relative importance of the various thrust production mechanisms. For what concerns the T5K, the impulsive contribution to the thrust of the heavy particles gasdynamic acceleration is always above 98% of the total, while the pressure contribution of the heavy particles gasdynamic acceleration is about 0.3% of the total, with the electromagnetic contribution decreasing with the mass flow rate from 1% to about 0.1%. In the T6 HCT the impulsive part of the heavy particles gasdynamic acceleration is also the highest contribution, being always higher than 85%. The pressure part is instead always about 0.01%, with the electromagnetic contribution reaching values as high as 15%. Hence, the T5K behaves as an arcjet-like whereas the T6, which also shows an arcjet-like behaviour, also shows a magnetoplasmadynamic acceleration.

VI.2. The Design Optimisation of the T6 HCT and the Direct Thrust Measurements

In the work presented in this thesis and for the first time in the open literature, the design of a hollow cathode was optimized to meet or exceed given requirements in terms of thrust, *Isp* and power consumption. The optimization process was carried out with the theoretical model described in chapter III. The optimized geometry has an insert diameter of 2 mm and a part straight and part diverging orifice. The straight part has a 0.2 mm radius and is 1.5 mm long, whereas the divergent part has a semicone aperture of 45 degrees and is 1 mm long.

The optimised T6 HCT was tested in the three different operational modes (cold gas mode, resistojet mode and discharge mode) also with the application, during the discharge mode only, of an external magnetic field in the orifice zone.

It is worth to note these are the first thrust measurements available in the open literature performed on a hollow cathode thruster in discharge mode, without and with the application of an external magnetic field, using a direct thrust balance.

Direct thrust measurements were also obtained on the T5A (with an anode/nozzle in front of the orifice) in cold gas and resistojet mode and on the T5K in discharge mode only.

The direct thrust measurement were obtained during a test campaign at Aerospazio Tecnologie Srl (reported in paragraph IV.3) and using a direct thrust balance developed as part of this study which is described in paragraph IV.4. Thanks to the availability of an in-house direct thrust balance it was possible to carry out reliable thrust measurement at a very low cost and in a timely way. This allowed each measurement to be repeated at least three times resulting in lower error bars and higher confidence in the measured values.

The cold gas thrust was in the range $50\mu N$ - $390\mu N$ for the T5A and in the range $65\mu N$ - $360\mu N$ for the T6 HCT, with the *Isp* in the range 21s-25s and 19s-27s respectively.

In resistojet mode, the T5A was tested from 2sccm to 20sccm at 15.4W and 45.3W leading to a thrust in the range 86μ N-746 μ N and 97μ N-804 μ N respectively, and an *Isp* in the range 39s-45s and 42s-51s respectively. The T6 HCT was tested in resistojet mode at 3.1W, 22W and 72.6W: the measured thrust is in the range 72 μ N-417 μ N, 210 μ N-722 μ N and 249 μ N-872 μ N respectively with the *Isp* ranging 30s-22s, 44s-38s and 52s-46 respectively. The efficiency in resistojet mode increases with the mass flow rate while decreases with the applied power and it is always <1.5%. The reason for this lies within the fact that the heater of these HCTs is not designed to efficiently heat the flowing gas but to raise the insert temperature for the thermionic emission.

The T5K was tested in the discharge mode for currents ranging 1.5A-2.5A: the thrust is in the range 0.2 to 0.7 mN and increases with the discharge current and the mass flow rate, with the specific impulse ranging 100s-140s and the efficiency 0.3%-1.2%. The T6 HCT was tested in the discharge mode for currents ranging 10A-24A. A thrust up to 2.61 mN with an *Isp* of 273s was obtained at 24 A and 10 sccm, and

Isp up to 323 s with a thrust of 1.53 mN was obtained at 24 A and 5 sccm. The thrust increases linearly with the mass flow rate and discharge current. The *Isp* increases linearly with the discharge current and also increases if the mass flow rate is decreased. The optimisation of the T6 geometry resulted in a significant improvement in the *Isp* achieving values that are about 3 times higher than those found in previous testing by Grubisic [12]. It must be noted that this improvement might even be higher since the use of an indirect thrust balance in [12] might have resulted in an overestimation of the measured thrust.

The trends of the measurements in the discharge mode are not affected by the application of the external magnetic field. Its effect is that of reducing the level of noise on the discharge voltage, even though the discharge voltage itself increases, and that of increasing the thrust by 10% to 20%.

The direct thrust measurements obtained within this research were obtained thanks to the development of a direct thrust balance. With the availability of the direct thrust balance it was possible to carry out reliable thrust measurement in-house at a very low cost. Those key points allowed each measurement to be carried out at least three times in a timely way.

VI.3. Novelty and Applicability of the Work

The conducted research is a wide-ranging study intended to better assess the potential use of hollow cathode thrusters by understanding the performance they can achieve and gaining deeper knowledge into the previously poorly understood thrust production mechanisms. The wide range of application of these devices, from spacecraft space charge control to primary electron source in a variety of thruster configurations, results in a wide range of applicability for the outcomes of this research.

The manufacturing and testing of hollow cathodes and hollow cathodes thrusters is extremely expensive due to the rare metals which form the high temperature parts of the item and laboratory costs, including rare gas propellants. On the other hand, the testing part during the development of an optimised HCT design can be dramatically reduced by using the theoretical model. The novel features of this research can be summarised as follows.

Theoretical Model

- For the first time in the open literature a theoretical model was developed
 with the main scope of predicting the performance of hollow cathode
 thrusters in terms of thrust, specific impulse and power consumption with
 reasonable accuracy.
- The model was found to predict the performance of HCTs with reasonable accuracy.
- A considerable achievement of this work is a better understanding of the physical processes contributing to the generation of the thrust, strengthened by the good agreement between model predictions and experimental data.

Optimised HCT Design

- The optimised T6 hollow cathode thruster is the first HCT which design was specifically optimised with the support of a theoretical model to meet a given set of requirements in terms of thrust, specific impulse and power consumption.
- The optimised T6 HCT exceeded the requirements in terms of thrust, *Isp* and power consumption. When compared to the performance measured in the past [12], it showed improvements in terms of *Isp* of about 3 times.
- The results obtained from the thrust measurements make the optimised T6
 HCT the electrothermal device operating on xenon with the highest *Isp*measured.

Direct Thrust Measurements

- The thrust data measured within this research are the first thrust measurements available in the open literature obtained on hollow cathode thrusters operating in discharge mode carried out with the use of a direct thrust balance.
- The measured thrust with the application of the external magnetic field in discharge mode is also the first ones obtained on HCTs available in the open literature.

VI.4. Recommendations for Future Work

The present study has dealt with a number of issues pertaining to hollow cathode thrusters. Although some of the questions have been successfully investigated, some others still remain and new ones have been posed. In this paragraph a few recommendations are presented for research studies that can help to increase our knowledge on these devices.

Improvements and full validation of the theoretical model.

Modifications in the theoretical model to include the computation of the sheath voltages would be a beneficial improvement towards the correct prediction of the discharge voltage. Other improvements can also be done, for example including non-classical behaviour of the plasma resistivity in the orifice. The development of a 2D or 3D code for the insert and orifice region, including the simulation of the sheath regions, would be beneficial in elucidating the physical processes ongoing during the discharge and the modifications in the plasma occurring when an external magnetic field is applied. The development of a model for the HCT breakdown which takes into account the electrodes temperature, the distance between the electrodes and the pressure in that region would also be beneficial to better understand the process of the formation and growth of the plasma.

The model's predictions should be verified with more experimental data on HCTs with different geometries to fully validate the model. Measurements on HCTs operating with lighter gases would also be beneficial for a deeper validation of the model. The acquisition of the measurements of plasma temperature and density would be of profound importance to validate the model from the plasma physics point of view.

Losses mechanisms in hollow cathode thrusters.

The maximum value for the thrust efficiency of 2.1% obtained within this research, even if improved with respect to past works [6, 12], might not be very appealing for space users. A significant effort should be made to identify which mechanisms contribute to the loss in efficiency.

The use of magnetic field.

Direct thrust measurements should be obtained from HCTs in discharge mode with different values of the external applied magnetic field to evaluate the improvements in performance and the trend with the magnetic field. The use of permanent magnets should be also investigated. Their use would probably bring improvements in performance, in particular to the thrust efficiency, since permanent magnets do not require additional power.

How to design the inter-electrodes spacer.

When an insulating spacer is used between the orifice tip and the nozzle, some careful engineering of the hollow cathode thruster assembly is required not to incur in the likely problem of the HCT not reaching the needed temperature to initiate the discharge. In this context, the author tested the T5 in a configuration similar to the T5A but with a different shapalM spacer, which upstream and downstream surfaces were in direct contact with the orifice plate and the nozzle respectively, as shown in Figure 129.

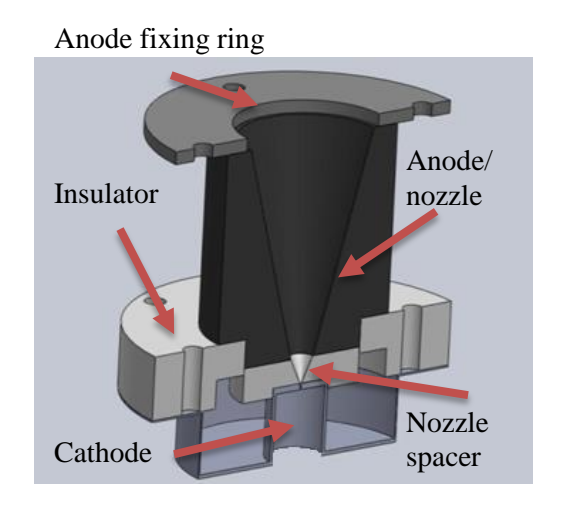


Figure 129 – T5 with a different nozzle spacer

Many attempts to initiate the cathode discharge were carried out without success, so the cathode was dismounted and visually inspected. From a visual inspection it was possible to notice two shadowed arcs on the shapalM spacer indicated by red arrows in Figure 130-a). The spacer, which was in contact with the orifice plate, subtracted heat from the cathode by conduction preventing the insert to reach the temperature

needed to initiate the discharge. This is strengthened by the fact that the heater voltage (which reflects the insert heating), shown in Figure 130-b), reaches a lower value when the spacer was in contact with the orifice resulting in the cathode not becoming hot enough to initiate the discharge.

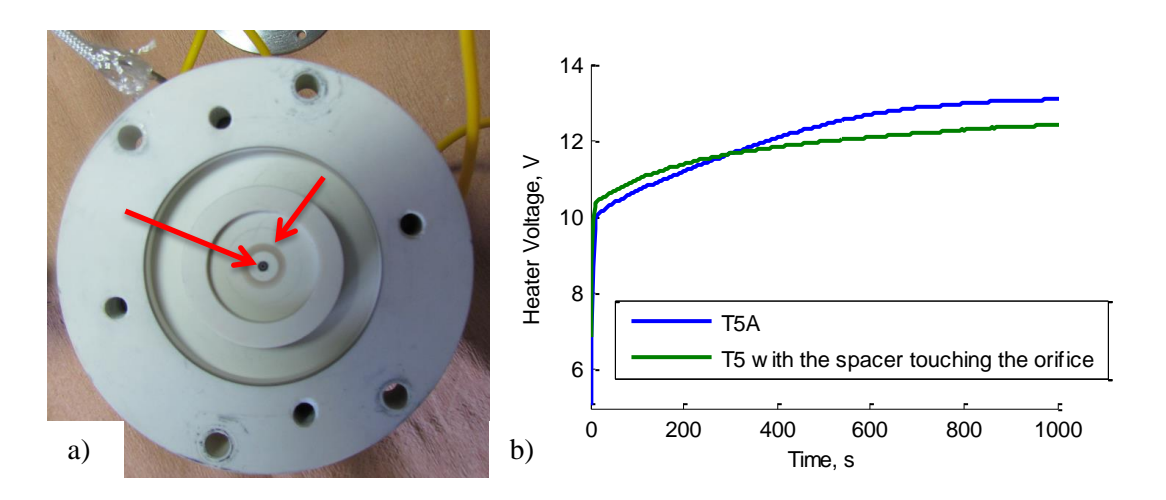


Figure 130 - a) Visual inspection of the spacer b) Heater voltage during the cathode warm up

To prevent this from happening, the use of an electrically and thermally insulating material is recommended. As an alternative, the spacer can be incorporated in the cathode-anode insulator disc to prevent any contact with the orifice tip or at least to minimise it, in order to minimise the heat subtracted by conduction from the orifice plate.

REFERENCE

- 1. Gessini, P., S.B. Gabriel, and D.G. Fearn, *The Hollow Cathode as a Micro-Ion Thruster*, in 27th International Electric Propulsion Conference. 2001. p. IEPC-01-233.
- 2. Gessini, P., S.B. Gabriel, and D.G. Fearn, *Hollow Cathode Thrust Measurement Using a Target: System Calibration and Development*, in 38th AIAA/ASME/SAE/ASEE Joint Propulsion Conference & Exhibition. 2002. p. AIAA 2002-4104.
- 3. Gessini, P., S.B. Gabriel, and D.G. Fearn, *The T6 Hollow Cathode as a Microthruster*, in *41st AIAA/ASME/SAE/ASEE Joint Propulsion Conference & Exhibit*. 2005. p. AIAA-2005-4078.
- 4. Gessini, P. and S.B. Gabriel, A Study of the Thrust Generated by a T6 Hollow Cathode, in 42nd AIAA/ASME/SAE/ASEE Joint Propulsion Conference & Exhibit. 2006. p. AIAA 2006-5265.
- 5. Gessini, P., et al., A Pendulum Target Balance for Ion Engine Thrust Measurement, in 30th International Electric Propulsion Conference. 2007. p. IEPC-2007-149.
- 6. Gessini, P., *Cathode Thrust Measurements Using a Target*. 2007, University of Southampton.
- 7. Grubisic, A.N., S.B. Gabriel, and D.G. Fearn, *Characterization of a T6 Based Hollow Cathode Thruster*, in *58th International Astronautical Federation Congress*. 2007.
- 8. Grubisic, A.N. and S.B. Gabriel, *Hollow Cathode Thruster for All-Electric Spacecraft*, in *58th International Astronautical Federation Congress*. 2007.
- 9. Grubisic, A.N. and S.B. Gabriel, *Preliminary thrust characterization of a T5 hollow cathode*, in 43rd AIAA/ASME/SAE/ASEE Joint Propulsion Conference & Exhibit. 2007.
- 10. Grubisic, A.N., S.B. Gabriel, and D.G. Fearn, *Preliminary Thrust Characterization of the T-Series Hollow Cathodes for All-Electric Spacecraft*, in 30th International Electric Propulsion Conference. 2007. p. IEPC-2007-81.
- 11. Grubisic, A.N. and S.B. Gabriel. *Hollow Cathode Thrust Mechanisms*. in 45th AIAA/ASME/SAE/ASEE Joint Propulsion Conference & Exhibition. 2009.
- 12. Grubisic, A.N., *Microthrusters Based on the T5 and T6 Hollow Cathodes*. 2009, University of Southampton.
- 13. Grubisic, A.N. and S.B. Gabriel, *Understanding Hollow Cathode Thrust Production Mechanisms*, in 31st International Electric Propulsion Conference. 2009.
- 14. Grubisic, A.N. and S.B. Gabriel, Development of an indirect counterbalanced pendulum optical-lever thrust balance for micro- to millinewton thrust measurement. Measurement Science & Technology, 2010. **21**(10).
- 15. Grubisic, A.N. and S.B. Gabriel, *Thrust production mechanism in hollow cathode microthrusters*, in *IEEE Aerospace Conference*. 2010.
- 16. Edwards, C.H., Discharge Characteristics and Instabilities in the UK-25 Ion Thruster Operating on Inert Gas Propellants. 1997, University of Southampton.

- 17. Gray, H.L., *Development of ion propulsion systems*. Gec Review, 1997. **12**(3): p. 154-+.
- 18. Wallace, N.C. and D.G. Fearn, *The design and performance of the T6 ion thruster*, in *Joint Propulsion Conference*. 1998. p. AIAA Paper 98-3342.
- 19. Fearn, D.G., et al., *The operation of ion thruster hollow cathodes using rare gas propellants*, in 21st International Electric Propulsion Conference. 1990. p. AIAA Paper No. 90-2584.
- 20. Latham, P.M., A.R. Martin, and A. Bond, *Design, manufacture and performance of the UK-25 engineering model thruster*. 1990. p. AIAA Paper 90-2541.
- 21. Harris, P.T. and S. Gair, A review of the cathode construction for the RAE 10/25 mN thruster, in International Electric Propulsion Conference. 1988. p. Paper No.88-078.
- 22. Philip, C.M. and D.G. Fearn, *RECENT HOLLOW-CATHODE INVESTIGATIONS AT ROYAL AIRCRAFT ESTABLISHMENT*. Aiaa Journal, 1974. **12**(10): p. 1319-1325.
- 23. Jahn, R.G., *Physics of Electric Propulsion*. 1968: McGraw-Hill.
- 24. Hill, P.G. and C.R. Peterson, *Mechanics and Thermodynamics of Propulsion*. 1965: Addison-Wesley Publishing Company.
- 25. Coletti, M., et al., European Student Moon Orbiter Solar Electric Propulsion Subsystem Architecture An All-Electric Spacecraft, in International Electric Propulsion Conference. 2007. p. IEPC-2007-111.
- 26. Gibbon, D., et al., The design, development and in-flight performance of alow power resistojet thruster, in 39th AIAA/ASME/SAE/ASEE Joint Propulsion Conference. 2003. p. AIAA-2003-4548.
- 27. Barley, S.Z., et al., Characterization of a Monopropellant Microthruster Catalytic bed, in 41st AIAA/ASME/SAE/ASEE Joint Propulsion Conference. 2005. p. AIAA-2005-4544.
- 28. Passaro, A. and A. Bulit, Development and Test of XR-150, a New High-Thrust 100 W Resistojet, in 33rd International Electric Propulsion Conference. 2013. p. IEPC-2013-219.
- 29. Nicolini, D., et al., Xenon Resistojets as Secondary Propulsion on EP Spacecrafts and Performance Results of Resistojets Using Xenon, in 28th International Electric Propulsion Conference. 2003. p. IEPC-03-305.
- 30. Welle, R.P., J.E. Pollard, and S.W. Janson, *One Kilowatt Hydrogen and Helium Arcjet Performance*. The Aerospace Corporation, 1993. **ATR-91** (8443)-2.
- 31. Hai-Bin, T., et al., Numerical and Experimental Study of a 1-kW Hydrazine Engineering Design Model Arcjet Thruster. Journal of Aerospace Engineering, 2014. **27**(1): p. 16-25.
- 32. Jameson, P., Hollow Cathode Thruster Requirements and Architectural design Esa ITT Development of a Hollow Cathode Thruster. 2011.
- 33. Frollani, D., M. Coletti, and S.B. Gabriel, *Thrust Measurements on the T6 Hollow Cathode Thruster Using Direct Thrust Balances*, in 33st International Electric Propulsion Conference. 2013.
- 34. Cronin, J.L., *Modern Dispenser Cathodes*. 1981. p. 19–32.
- 35. Goebel, D.M. and I. Katz, *Fundamentals of Electric Propulsion: Ion and Hall Thrusters*. JPL Space Science and Technology Series. 2008.
- 36. Simmons, J.G., *Richardson-Schottky Effect in Solids*. Physical Review Letters, 1965. **15**(25): p. 967-968.

- 37. Siegfried, D.E. and P.J. Wilbur, *A MODEL FOR MERCURY ORIFICED HOLLOW CATHODES THEORY AND EXPERIMENT*. Aiaa Journal, 1984. **22**(10): p. 1405-1412.
- 38. Csiky, G.A., Investigation of a Hollow Cathode Discharge Plasma, in 7th AIAA Electric Propulsion Conference. 1969. p. AIAA- 69-258.
- 39. Philip, C.M., *STUDY OF HOLLOW CATHODE DISCHARGE CHARACTERISTICS*. Aiaa Journal, 1971. **9**(11): p. 2191-&.
- 40. Fearn, D.G. and C.M. Philip, *INVESTIGATION OF PHYSICAL PROCESSES IN A HOLLOW CATHODE DISCHARGE*. Aiaa Journal, 1973. **11**(2): p. 131-132.
- 41. Krishnan, M., et al., *PHYSICAL PROCESSES IN HOLLOW CATHODES*. Aiaa Journal, 1977. **15**(9): p. 1217-1223.
- 42. Siegfried, D.E. and P.J. Wilbur, Studies on an Experimental Quartz Tube Hollow Cathode, in 14th International Electric Propulsion Conference. 1979. p. AIAA-79-2056.
- 43. Siegfried, D.E. and P.J. Wilbur, *INVESTIGATION OF MERCURY HOLLOW-CATHODE PHENOMENA*. Astronautics & Aeronautics, 1978. **16**(12): p. B22-B22.
- 44. Rehn, L. and H.R. Kaufman, Correlation of Inert Gas Hollow Cathode Performance, in 13th AIAA/DGLR International Electric Propulsion Conference. 1978. p. AIAA-78-707.
- 45. Csiky, G.A.g., Measurements of Some Properties of a Discharge from a Hollow Cathode. 1969. p. NASA TN D-4966.
- 46. Csiky, G.A., *LANGMUIR PROBE MEASUREMENTS IN A DISCHARGE FROM A HOLLOW CATHODE*. Journal of Spacecraft and Rockets, 1970. **7**(4): p. 474-&.
- 47. Rudwan, I.M.A., *Physics of Hollow Cathode Breakdown and Steady-State Operation with Several Inert Gas Propellants*. 2003, University of Southampton.
- 48. Jack, T.M., S.W. Patterson, and D.G. Fearn, *The Effect of the Keeper Electrode on Hollow Cathode Characteristics*, in *36th AIAA/ASME/SAE/ASEE Joint Propulsion Conference and Exhibit*. 2000. p. AIAA-2000-3533.
- 49. Patterson, S.W. and D.G. Fearn, *The Generation of High Energy Ions in Hollow Cathode Discharges*, in *26th International Electric Propulsion Conference*. 1999. p. IEPC-99-125.
- 50. Fearn, D.G. and S.W. Patterson, *The Compatibility of Hollow Cathode Characteristics with a Variety of Ion Thruster Designs*, in *26th International Electric Propulsion Conference*. 1999. p. IEPC-99-133.
- 51. Fearn, D.G. and S.W. Patterson, *Characterization of the High Current Hollow Cathode for the T6 Ion Thruster*, in *AIAA/ASME/SAE/ASEE 34th Joint Propulsion Conference and Exhibit*. 1998. p. AIAA-98-3346.
- 52. Patterson, S.W., A.K. Malik, and D.G. Fearn, *Noise and Oscillatory Disturbances in the T6 Ion Thruster Hollow Cathode*, in 35th AIAA/ASME/SAE/ASEE Joint Propulsion Conference and Exhibit. 1999. p. AIAA-99-2577.
- 53. Patterson, S.W., *Discharge Physics and Associated Phenomena in an Ion Thruster Type Hollow Cathode*. 2003, **Imperial College**.

- 54. Fearn, D.G. and S.W. Patterson, *The Hollow Cathode a Versatile Component of Electric Thrusters*, in *ESA/CNES International Conference on Spacecraft Propulsion*. 2000. p. **ESA SP-465**.
- 55. Fearn, D.G. The operation of hollow cathodes under conditions suitable for ion beam neutralisation. in Electric Propulsion of Space Vehicles. 1973.
- 56. Kaufman, H.R., *Technology of electron Bombardment Ion Thruster*. Advances in Electronics and Electron Physics, 1974. **36**.
- 57. Salhi, A. and P.J. Turchi, *A first-principles model for orificed hollow cathode operation*, in *Joint Propulsion Conference*. 1992. p. **AIAA PAPER 92-3742**.
- 58. Salhi, A., Theoretical and experimental studies of orificed, hollow cathode operation. 1993, **The Ohio State University**.
- 59. Katz, I., et al., *Model of plasma contactor performance*. Journal of Spacecraft and Rockets, 1997. **34**(6): p. 824-828.
- 60. Katz, I., et al., *One-dimensional hollow cathode model*. Journal of Propulsion and Power, 2003. **19**(4): p. 595-600.
- 61. Mikellides, I.G., et al., *Hollow cathode theory and experiment. II. A two-dimensional theoretical model of the emitter region.* Journal of Applied Physics, 2005. **98**(11).
- 62. Mikellides, I.G. and I. Katz, *Wear mechanisms in electron sources for ion propulsion, 1: neutralizer hollow cathode.* Journal of Propulsion and Power, 2008. **24**(4): p. 855-65.
- 63. Goebel, D.M., et al., *Potential fluctuations and energetic ion production in hollow cathode discharges.* Physics of Plasmas, 2007. **14**(10).
- 64. Mikellides, I.G., et al., Wear mechanisms in electron sources for ion propulsion, 2: Discharge hollow cathode. Journal of Propulsion and Power, 2008. **24**(4): p. 866-879.
- 65. Mikellides, I., et al., Numerical Simulations of the Partially-ionized Gas in a 100-A LaB6 Hollow Cathode, in 33rd International Electric Propulsion Conference. 2013. p. IEPC-2013-142.
- 66. Fradkin, D.B., Analysis of Acceleration Mechanisms and Performance of an Applied Field MPD Arcjet. 1973, Princeton University.
- 67. Sasoh, A. and Y. Arakawa, *ELECTROMAGNETIC EFFECTS IN AN APPLIED-FIELD MAGNETOPLASMADYNAMIC THRUSTER*. Journal of Propulsion and Power, 1992. **8**(1): p. 98-102.
- 68. Mikellides, P.G. and P.J. Turchi, A Theoretical Model for the Thrust and Voltage of Applied-Field MPD Thruster, in 34th Joint Propulsion Conference and Exhibit. 1998.
- 69. Coletti, M., A thrust formula for an MPD thruster with applied-magnetic field. Acta Astronautica, 2012. **81**(2): p. 667-674.
- 70. Glocker, B., H.O. Schrade, and M. Auweter-Kurtz, *Performance Calculation of Arc Jet Thrusters The Three Channel Model*, in 23rd Electric Propulsion Conference. 1993.
- 71. Wallner, E. and J. Czika, *Arc-Jet Trustor for Space Propulsion*, in *Lewis research Center*, *Cleveland*, *Ohio*. NASA TN D-2868.
- 72. Glocker, B. and H.O. Schrade, *Numerical Prediction of Arcjet Performance*, in *21st International Electric Propulsion Conference*. 1990.
- 73. Packan, D., J. Bonnet, and S. Rocca, Thrust measurement with the ONERA micronewton balance, in 30th International Electric Propulsion Conference. 2007.

- 74. Diamant, K.D., et al., *Thrust Stand Characterization of the NASA Evolutionary Xenon Thruster*. Journal of Propulsion and Power, 2011. **27**(4): p. 777-785.
- 75. Koizumi, H., K. Komurasaki, and Y. Arakawa, *Development of thrust stand* for low impulse measurement from microthrusters. Review of Scientific Instruments, 2004. **75**(10): p. 3185-3190.
- 76. Ziemer, J.K., *Performance Measurements Using a Sub-Micronewton Resolution Thrust Stand*, in *International Electric Propulsion Conference*. 2001. p. **IEPC-01-238**.
- 77. Chen, X., The impact force acting on a flat plate exposed normally to a rarefied plasma plume issuing from an annular or circular nozzle. Journal of Physics D-Applied Physics, 2010. **43**(31).
- 78. Snyder, A. and B.A. banks, *Thrust Measurements of a hollow cathode discharge*. 1972.
- 79. Kameyama, A. and P.J. Wilbur, *Zenith-Angle Distributions of Erosion Rates near High-Current Hollow Cathodes*, in 32nd Joint Propulsion Conference. 1996. p. AIAA 96-3208.
- 80. Latham, P.M., A.J. Pearce, and R.A. Bond, *Erosion Processes in the UK-25 Ion Thruster*, in *22nd International Electric Propulsion Conference*. 1991. p. IEPC 91-096.
- 81. Friedly, V.J. and P.J. Wilbur, *HIGH-CURRENT HOLLOW-CATHODE PHENOMENA*. Journal of Propulsion and Power, 1992. **8**(3): p. 635-643.
- 82. Kameyama, I. and P.J. Wilbur, *Measurements of ions from high-current hollow cathodes using electrostatic energy analyzer*. Journal of Propulsion and Power, 2000. **16**(3): p. 529-535.
- 83. William, G., et al., Laser Induced Fluorescence Characterization of Ions Emitted from a Hollow Cathode, in 35th Joint Propulsion Conference. 1999. p. AIAA Paper No. 99-2862.
- 84. Rawlin, V.K., Internal Erosion Rates of a 10-kW Xenon Ion Thruster, in 24th Joint Propulsion Conference and Exhibit. 1988. p. AIAA-88-2912.
- 85. Kameyama, I., Effects of Neutral Density on Energetic Ions Produced Near High-Current Hollow Cathodes. 1997.
- 86. Mikellides, I.G., et al., Evidence of nonclassical plasma transport in hollow cathodes for electric propulsion. Journal of Applied Physics, 2007. **101**(6).
- 87. Jorns, B.A., I.G. Mikellides, and D.M. Goebel, *Temporal Fluctuations in a 100-A LaB6 Hollow Cathode*, in *33rd International Electric Propulsion Conference*. 2013. p. **IEPC Paper No. 13-385**.
- 88. Mikellides, I.G., Effects of viscosity in a partially ionized channel flow with thermionic emission. Physics of Plasmas, 2009. **16**(1).
- 89. Miller, J.S., et al., *Xenon Charge Echange Cross Sections for Electrostatic Thruster models.* Journal of Applied Physics, 2002. **91**.
- 90. Rudwan, I.M., N.C. Wallace, and M. Kelly, *Dispenser Temperature Profile Measurement and Discharge Current Division in the T5 & T6 Kaufman-type Ion Thrusters*, in *30th International Electric Propulsion Conference*. 2007. p. IEPC-2007-170.
- 91. Pottinger, S., *Investigation of Steady State Characteristics of Hollow Cathode Internal Plasmas using Optical Emission Spectroscopy*. 2005, University of Southampton.
- 92. Braginskii, S.I., *Transport Processes in Plasmas*. Reviews of Plasma Physics, 1965. **1**.

- 93. Reid, R.C., *The Properties of Gases and Liquids*. 1977: McGraw-Hill.
- 94. Kierzenka, J. and L.F. Shampine, *A BVP Solver Based on Residual Control and the Matlab PSE*. ACM Transactions on Mathematical Software, 2001. **27**.
- 95. Liebermann, D.M. and A. Liechtenberg, *Principles of Plasma Discharges and Materials Processing*. 1994: Wiley.
- 96. Mukherjee, J., L.M. Gantayet, and S.A. Ahmad, *Free Jet Expansion of Atomic Beam: Simulation Studies of Some Parameters*. <div data-canvas-width="13.86401344537815" style="left: 206.333px; top: 78.6943px; font-size: 13.864px; font-family: serif; transform: scaleX(0.990287);">J. Phys. D: Appl. Phys. 33 (2000) 1386–1392, 2000.
- 97. Jameson, K., D.M. Goebel, and R.M. Watkins, *Hollow Cathode and Thruster Discharge Chamber Plasma Measurements Using High-Speed Scanning Probes*, in 29th IEPC. 2005: Princeton University.
- 98. Rudwan, I.M.A., et al., Emitter Depletion Measurements and Modeling in the T5 and T6 Kaufman-Type Ion Thrusters, in 30th IEPC. 2007.
- 99. Taylor, J.R., An introduction to error analysis. 1996: UniversityScienceBooks.
- 100. Pivots, R.F. *Double-Ended Pivot no. 6012-800*. [cited Available at the time of publication at http://www.flexpivots.com/doubleendedpivotbearings.php.
- 101. Aston, S.M., *Optical Read-Out Techniques for the Control of Test-Masses in Gravitational Wave Observatories*. 2011, University of Birmingham.
- 102. Thorlabs, *Mirror no. PF05-03-F01*. Available at the time of publication at http://www.thorlabs.de/catalogpages/V21/774.PDF.
- 103. Oppenheim, A.V. and R.W. Schafer, *Discrete-time signal processing*. 2009: Prentice Hall.
- 104. Kovach, C.W., High Performance Stainless Steel. Nickel Institute.
- 105. Rutt, H., *Technical Note 02-053: The thermal conductivity of macor at intermediate cryogenic temperatures.* 2002, Thomas Jefferson National Accelerator Facility.
- 106. Lev, D., Investigation of Efficiency in Applied Field MagnetoPlasmaDynamic Thrusters. 2012, Princeton University.
- 107. VisionEngineering, *Hawk Duo CNC*. Available at the time of publication at http://www.visioneng.com/products/non-contact-measurement/hawk-automated-optical-and-video-measurement-microscope#Vtab99.